


Winter 2011

# Investigation of microbubble/droplet formation in cross-flow and co-flow micro devices

Tom J. John

Follow this and additional works at: <https://digitalcommons.latech.edu/dissertations>

 Part of the [Biomedical Engineering and Bioengineering Commons](#), and the [Chemical Engineering Commons](#)

---

**INVESTIGATION OF MICROBUBBLE/DROPLET FORMATION  
IN CROSS-FLOW AND CO-FLOW MICRO DEVICES**

by

Tom J. John, M.CA, B.Sc.

A Dissertation Presented in Partial Fulfillment  
of the Requirements for the Degree  
Doctor of Philosophy

COLLEGE OF ENGINEERING AND SCIENCE  
LOUISIANA TECH UNIVERSITY

February 2011

UMI Number: 3451088

All rights reserved

INFORMATION TO ALL USERS

The quality of this reproduction is dependent upon the quality of the copy submitted.

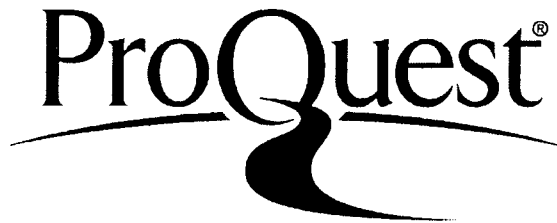
In the unlikely event that the author did not send a complete manuscript and there are missing pages, these will be noted. Also, if material had to be removed, a note will indicate the deletion.



UMI 3451088

Copyright 2011 by ProQuest LLC.

All rights reserved. This edition of the work is protected against unauthorized copying under Title 17, United States Code.



ProQuest LLC  
789 East Eisenhower Parkway  
P.O. Box 1346  
Ann Arbor, MI 48106-1346

LOUISIANA TECH UNIVERSITY

THE GRADUATE SCHOOL

February 2011

Date

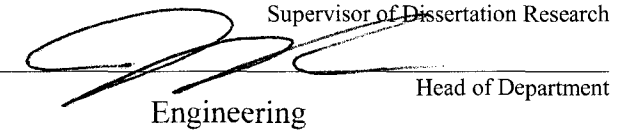
We hereby recommend that the dissertation prepared under our supervision  
by Tom J. John

entitled INVESTIGATION OF MICROBUBBLE/DROPLET FORMATION IN CROSS  
FLOW AND CO-FLOW MICRO DEVICES

be accepted in partial fulfillment of the requirements for the Degree of  
Doctor of Philosophy



Supervisor of Dissertation Research

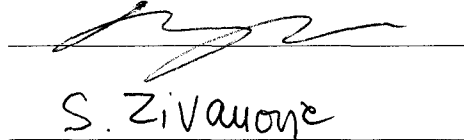
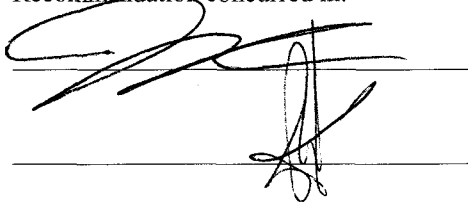


Engineering

Head of Department

Department

Recommendation concurred in:



S. Zivavone

Advisory Committee

Approved:

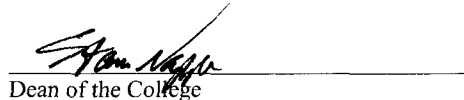


Director of Graduate Studies

Approved:



Dean of the Graduate School



Dean of the College



## ABSTRACT

The primary goal of the work presented in this dissertation is to generate microbubbles of a diameter of less than  $15\mu\text{m}$  inside micro channels. In order to achieve this detailed understanding, the facts and limitations behind the generation of microbubbles inside a micro channel are determined from existing literature. The major limitations of the current bubble/droplet generators are found to be the bubble confinement effect, the merging of bubbles, the difficulty in determining bubble diameter and the need for smaller channels to generate smaller bubbles. A device eliminating these drawbacks is conceptualized, and its feasibility is studied using COMSOL® and found to be successful. Based on the findings of the initial studies, prototypes of a new generation of microbubble/droplet generators are developed in this work. This generator utilizes a fused silica tube as the channel carrying the secondary fluid. The micro channel into which the bubbles/droplets are formed is made on a silicon wafer and is sealed using a glass plate. Both cross-flow and co-flow bubble generation devices are analyzed as part of this work. The new generation devices have the advantage of generating unconfined spherical bubbles inside a micro channel while keeping the pressure drop across the channel as low as possible. The new generation cross-flow bubble generator is able to produce bubbles smaller than that possible with existing devices. The cross-flow devices were found to be more efficient in producing microbubbles of smaller diameter in comparison to a similar co-flow device operating under identical conditions. In order to

produce smaller microbubbles inside micro channels, a flow focusing technique is introduced in both cross-flow and co-flow devices. Using flow focusing techniques has made it possible to produce microbubbles smaller than that possible without flow focusing. The major parameters that affect bubble formation inside micro channels are determined using a parametric study of both the fluid properties and the geometry of micro channels. A mathematical model is developed to predict the bubble diameter at its detachment from the orifice in a cross-flow device and is validated using experimental data. Surface tension and drag force are found to be the major factors in determining the bubble diameter at detachment. Major achievements of this work are summarized below:

- 1) A new generation of a microbubble/droplet generator capable of producing unconfined microbubble/droplet is developed in this study.
- 2) The merging problem of bubbles inside the micro channel immediately after the bubble detaches from orifice is observed for the first time during this study.
- 3) A microbubble of diameter  $11\mu\text{m}$  is generated in the micro channel of hydraulic diameter  $162\mu\text{m}$ .
- 4) The bubbly region of bubble formation inside a micro channel is further divided into three in this work: confined region, active region and saturation region.
- 5) The flow focusing technique inside the cross-flow devices is introduced and studied for the first time during this work.
- 6) Bubbles of diameter  $6\mu\text{m}$  were produced using the flow focusing technique inside the micro channel of hydraulic diameter  $162\mu\text{m}$ .
- 7) Circular micro channels were found to be more efficient than straight channels when used in a cross-flow device.

## APPROVAL FOR SCHOLARLY DISSEMINATION

The author grants to the Prescott Memorial Library of Louisiana Tech University the right to reproduce, by appropriate methods, upon request, any or all portions of this Dissertation. It is understood that "proper request" consists of the agreement, on the part of the requesting party, that said reproduction is for his personal use and that subsequent reproduction will not occur without written approval of the author of this Dissertation. Further, any portions of the Dissertation used in books, papers, and other works must be appropriately referenced to this Dissertation.

Finally, the author of this Dissertation reserves the right to publish freely, in the literature, at any time, any or all portions of this Dissertation.

Author



Date

02/02/2011

## **DEDICATION**

I dedicate this work to the loving memory of my late wife, Bini Baby P. whom I lost during the first year of my PhD. It was her wish and dedication which made me commence my Ph.D. I also dedicate this work to her sorrowing family.

When God permits trails, he also provides comfort

by Bini Baby P.

## TABLE OF CONTENTS

ABSTRACT .....	iii
LIST OF FIGURES.....	xi
LIST OF TABLES .....	xix
ACKNOWLEDGEMENTS .....	xx
CHAPTER 1 INTRODUCTION .....	1
1.1 Bubble/Droplet Generators .....	1
1.1.1 Overview on the current bubble/droplet generation methods.....	3
1.1.2 Limitations of the current bubble/droplet generators .....	5
1.2 Research Objectives .....	11
1.2.1 New generation bubble/droplet generators.....	13
1.2.2 Flow focusing in cross-flow bubble/droplet generators .....	15
CHAPTER 2 LITERATURE REVIEW .....	17
2.1 Macro Level Bubble/Droplet Generators.....	17
2.2 Micro Level Cross-flow Bubble/Droplet Generators.....	20
2.3 Micro Co-Flow and Flow Focusing Bubble/Droplet Generators.....	24
CHAPTER 3 THEORETICAL MODEL .....	27
3.1 Microbubble Growth and Detachment Model .....	28
3.2 Modified Model for Flow Focusing.....	32
3.3 Feasibility Study for Flow Focusing .....	34

CHAPTER 4 FABRICATION.....	38
4.1 Microchannel Fabrication .....	40
4.1.1 Mask design .....	41
4.1.2 Photolithography.....	43
4.1.3 Buffered oxide etching (BOE).....	45
4.1.4 Inductively coupled plasma etching (ICP) .....	45
4.1.5 Anodic bonding .....	46
4.1.6 Machining and tube fixing.....	51
CHAPTER 5 EXPERIMENTAL METHODS AND UNCERTAINTY ANALYSIS.....	52
5.1 Experimental Test Bench .....	52
5.2 Uncertainty Analysis .....	56
5.2.1 Uncertainty in bubble diameter .....	57
5.2.2 Uncertainty in Reynolds number .....	58
5.2.3 Uncertainty in void fraction.....	61
5.2.4 Uncertainty in superficial velocity.....	62
CHAPTER 6 RESULTS AND DISCUSSIONS.....	65
6.1 Cross-flow Bubble Generators .....	67
6.1.1 Case 1: Variable parameter: Reynolds number of base liquid flow .....	73
6.1.2 Case 2: Variable parameter: Gas flow rate in secondary channel .....	76
6.1.3 Case 3: Variable parameter: Hydraulic diameter secondary channel .....	78
6.1.4 Case 4: Variable parameter: Hydraulic diameter base channel .....	84
6.1.5 Case 5: Variable parameter: Different gas through secondary channel .....	87

6.1.6	Case 6: Variable parameter: Different base liquids.....	90
6.2	Cross-flow Bubble Generator with Flow Focusing.....	96
6.2.1	Case 1: Comparison of cross-flow device with and without flow focusing.....	100
6.2.2	Case 2: Comparison of bubble formation in secondary channel with different hydraulic diameters.....	102
6.2.3	Case 3: Comparison of different shapes of flow focusing structures on cross-flow device performance .....	104
6.2.4	Case 4: Comparison of cross-flow device performance with different base length flow focusing structures.....	111
6.3	Co-Flow Bubble Generators.....	117
6.3.1	Case 1: Variable parameter: Reynolds number of base liquid flow and gas flow rate.....	124
6.3.2	Case 2: Variable parameter: Hydraulic diameter of secondary channel.....	126
6.3.3	Case 3: Variable parameter: Different base liquids.....	130
6.4	Co-Flow Bubble Generators with Flow Focusing.....	132
6.4.1	Case 1: Comparison of co-flow device performance with and without flow focusing technique .....	134
6.4.2	Case 2: Comparison of the performance of co-flow devices with different shapes of flow focusing structures.....	135
6.4.3	Case 3: Comparison of void fraction of bubble formation in co-flow device with flow focusing .....	138
6.5	Droplet Generators .....	141
6.5.1	Case 1: Cross-flow droplet generators.....	143
6.5.2	Case 2: Co-flow droplet generators .....	144
6.6	Cross-flow Bubble Generator with Round Base Channel.....	146

CHAPTER 7 FUTURE WORK AND CONCLUSIONS .....	150
APPENDIX A .....	156
APPENDIX B .....	159
APPENDIX C .....	163
REFERENCES.....	167



## LIST OF FIGURES

Figure 1.1	Schematic diagram showing co-flow, focused flow and cross-flow bubble/droplet generators.....	4
Figure 1.2	Microbubble confined inside a micro channel [45] .....	6
Figure 1.3	T-junction bubble/droplet made with same depth micro channels .....	7
Figure 1.4	Consecutive microbubbles merging with each other right after getting detached from the orifice .....	10
Figure 1.5	Schematic representation of the new generation bubble/droplet generator in co-flow and cross-flow device .....	13
Figure 1.6	Schematic representation of flow focusing technique in a cross-flow bubble/droplet generation device .....	16
Figure 3.1	Schematic figure showing direction of different forces acting on the microbubble during its growth [44] .....	28
Figure 3.2	Schematic figure showing microbubble generation in a micro channel with flow focusing .....	33
Figure 3.3	Different numerical models generated using COMSOL for feasibility study (base channel 100 $\mu$ m, secondary channel 20 $\mu$ m, flow focusing structures 50 $\mu$ m and 100 $\mu$ m, flow direction -X) .....	35
Figure 4.1	Process flow for manufacturing microbubble/droplet generator.....	39
Figure 4.2	Mask pattern for cross-flow and co-flow devices .....	42
Figure 4.3	Chrome mask for generation cross-flow devices .....	43
Figure 4.4	Apparatus for the anodic bonding of silicon to glass.....	47
Figure 4.5	Anodic bonding setup with microscope facility.....	48

Figure 4.6	Manufacturing steps involved in making co-flow and cross-flow device .....	50
Figure 4.7	Fully finished cross-flow and co-flow device with connectors.....	51
Figure 5.1	Experimental test bench used for visualizing and measuring the microbubble/droplet generation .....	53
Figure 5.2	Microscope with camera and light sources mounted on it.....	54
Figure 6.1	Plot compares bubble detachment diameter prediction by the mathematical model with the experimental data (base channel 150 $\mu$ m, secondary channel 10 $\mu$ m) .....	68
Figure 6.2	Merging of successive bubbles into the previous bubble, causing an increase in the diameter of the already detached bubble.....	70
Figure 6.3	Plot compares bubble detachment diameter prediction by the mathematical model with the experimental data (base channel 150 $\mu$ m, secondary channel 15 $\mu$ m) .....	71
Figure 6.4	Bubble formation in a cross-flow bubble generator at various time interval taken at 7500fps. (Base channel 270 $\mu$ m, secondary channel 10 $\mu$ m) .....	72
Figure 6.5	Plot gives the void fraction of bubble formation in base channel for different magnitudes of Reynolds number (base channel 150 $\mu$ m, secondary channel 10 $\mu$ m) .....	74
Figure 6.6	Plot gives the variation in superficial velocity of gas with respect to the change in superficial velocity of the base liquid in a cross-flow device (base channel 150 $\mu$ m, secondary channel 10 $\mu$ m).....	76
Figure 6.7	Plot gives the variation in the bubble diameter with change in base liquid Reynolds number for six different gas flow momentum (base channel 160 $\mu$ m, secondary channel 15 $\mu$ m).....	77
Figure 6.8	Plot gives the variation in void fraction of bubble formation in a cross-flow device for different magnitudes of Reynolds number of base fluid flow (base channel 160 $\mu$ m, secondary channel 5 $\mu$ m) .....	79
Figure 6.9	Plot gives the void fraction of bubble flow in micro channel for different magnitudes of Reynolds number (base channel 160 $\mu$ m, secondary channel 10 $\mu$ m) .....	80

Figure 6.10	Plot gives the void fraction of bubble flow in micro channel for different magnitudes of Reynolds number (base channel 160 $\mu\text{m}$ , secondary channel 15 $\mu\text{m}$ ) .....	81
Figure 6.11	Plot gives the void fraction of bubble flow in micro channel for different magnitudes of Reynolds number (base channel 160 $\mu\text{m}$ , secondary channel 25 $\mu\text{m}$ ) .....	83
Figure 6.12	Plot gives the void fraction of bubble flow in micro channel for different magnitudes of Reynolds number (base channel 160 $\mu\text{m}$ , secondary channel 50 $\mu\text{m}$ ) .....	84
Figure 6.13	Plot gives the comparison of bubble diameter for three different hydraulic diameters of base channel (secondary channel = 10 $\mu\text{m}$ ) .....	85
Figure 6.14	Bubble formed in base channel of width to depth ratio greater than one (Base channel = 193 $\mu\text{m}$ , secondary channel = 10 $\mu\text{m}$ ) .....	86
Figure 6.15	Plot gives the void fraction of bubble formation in base channel with high aspect ratio for different magnitudes of Reynolds number of base liquid (base channel 193 $\mu\text{m}$ , secondary channel 10 $\mu\text{m}$ ).....	87
Figure 6.16	Plot gives the comparison of void fraction of bubble formation for two different gases at same pressure drop across the secondary channel (base channel 150 $\mu\text{m}$ , secondary channel 10 $\mu\text{m}$ ).....	89
Figure 6.17	Plot gives the void fraction of oxygen bubble formation in base channel for different magnitudes of Reynolds number (base channel 150 $\mu\text{m}$ , secondary channel 10 $\mu\text{m}$ ) .....	90
Figure 6.18	Plot gives the void fraction of bubble formation in base channel for base liquids with different kinematic viscosities (base channel 162 $\mu\text{m}$ , secondary channel 10 $\mu\text{m}$ , Gas flow rate 0.187ml/hr).....	92
Figure 6.19	Plot gives the void fraction of bubble formation in base channel for base liquids with different kinematic viscosities (base channel 162 $\mu\text{m}$ , secondary channel 10 $\mu\text{m}$ , Gas flow rate 0.145ml/hr).....	94
Figure 6.20	Plot gives the void fraction of Nitrogen bubble formation in base channel for different magnitude of Reynolds numbers (base channel 162 $\mu\text{m}$ , secondary channel 10 $\mu\text{m}$ , Gas flow rate 0.187ml/hr).....	95
Figure 6.21	Contour plot of velocity profile in a base channel with and without flow focusing (hydraulic diameter =150 $\mu\text{m}$ , flow focusing structure =100 $\mu\text{m}$ ).....	97

Figure 6.22	Contour plot of bubble formation in base channel with different shapes of flow focusing structures (hydraulic diameter =100 $\mu$ m, flow focusing structure =50 $\mu$ m and 75 $\mu$ m, secondary channel = 20 $\mu$ m) [45] .....	98
Figure 6.23	Bubble diameter in cross-flow bubble generator with and without flow focusing structures of different shapes (hydraulic diameter =100 $\mu$ m, secondary channel = 20 $\mu$ m) [45].....	99
Figure 6.24	Bubbles formed in a cross-flow bubble generator with semi-circular flow focusing structure embedded in base channel (base channel 160 $\mu$ m, secondary channel 10 $\mu$ m, flow focusing structure height100 $\mu$ m).....	100
Figure 6.25	Plot gives the comparison between bubble diameters formed in cross-flow devices with and without flow focusing (base channel 160 $\mu$ m, secondary channel 10 $\mu$ m, flow focusing structure height 100 $\mu$ m).....	101
Figure 6.26	Plot gives the comparison between the void fractions of bubbles formed in base channel with semi-circle structure for two different secondary channel diameters (base channel 160 $\mu$ m, flow focusing structure height 100 $\mu$ m).....	103
Figure 6.27	Mask used for the manufacturing of different shapes of flow focusing structures. (base channel 150 $\mu$ m, flow focusing structure height 100 $\mu$ m).....	104
Figure 6.28	Plot gives the comparison between bubble diameters formed in cross-flow devices with three different shaped flow focusing structures (base channel 160 $\mu$ m, secondary channel 10 $\mu$ m, flow focusing structure height 100 $\mu$ m).....	105
Figure 6.29	Contour plot of velocity profile in a base channel without flow focusing and with three different shapes of flow focusing structures (hydraulic diameter =150 $\mu$ m, flow focusing structure =100 $\mu$ m).....	106
Figure 6.30	Comparison between the non-dimensionalized volume of bubbles formed in the cross-flow devices with three different shapes of flow focusing structures (base channel 150 $\mu$ m, secondary channel 10 $\mu$ m, flow focusing structure height 100 $\mu$ m).....	107
Figure 6.31	Plot gives the void fraction of bubble formation in base channel with semi-circle flow focusing structure at different magnitudes of Reynolds number (base channel 160 $\mu$ m, secondary channel 10 $\mu$ m, flow focusing structure height = 100 $\mu$ m).....	108

Figure 6.32	Plot gives the void fraction of bubble formation in base channel with triangle flow focusing structure at different magnitudes of Reynolds number (base channel 160 $\mu\text{m}$ , secondary channel 10 $\mu\text{m}$ , flow focusing structure height = 100 $\mu\text{m}$ ).....	109
Figure 6.33	Plot gives the void fraction of bubble formation in base channel with rectangle flow focusing structure at different magnitudes of Reynolds number (base channel 160 $\mu\text{m}$ , secondary channel 10 $\mu\text{m}$ , flow focusing structure height = 100 $\mu\text{m}$ ).....	111
Figure 6.34	Mask used for the manufacturing of different shapes of flow focusing structures with base length 300 $\mu\text{m}$ . (base channel 150 $\mu\text{m}$ , flow focusing structure height 100 $\mu\text{m}$ ).....	112
Figure 6.35	Plot represents the comparison between the bubble diameter formed in cross-flow device with flow focusing using semi-circle structures of two different base length (base channel 160 $\mu\text{m}$ , secondary channel 10 $\mu\text{m}$ , flow focusing structure height 100 $\mu\text{m}$ ).....	113
Figure 6.36	Contour plot of velocity profile in a base channel with flow focusing structures of different base length (hydraulic diameter =150 $\mu\text{m}$ , flow focusing structure =100 $\mu\text{m}$ ).....	114
Figure 6.37	Plot gives the comparison between the bubble diameter formed in cross-flow device with flow focusing using rectangular structures of two different base length (base channel 160 $\mu\text{m}$ , secondary channel 10 $\mu\text{m}$ , flow focusing structure height 100 $\mu\text{m}$ ).....	115
Figure 6.38	Plot gives the comparison between the bubble diameter formed in cross-flow device with flow focusing using triangular structures of two different base length (base channel 160 $\mu\text{m}$ , secondary channel 10 $\mu\text{m}$ , flow focusing structure height 100 $\mu\text{m}$ ).....	116
Figure 6.39	Schematic representation of the co-flow bubble generator.....	118
Figure 6.40	Represents the bubble formation inside a co-flow device with base liquid coming from both sides of the bubble and forcing the bubble to detach from the orifice ((base channel 150 $\mu\text{m}$ , secondary channel 10 $\mu\text{m}$ ).....	119
Figure 6.41	Plot gives the variation in bubble diameter generated in a co-flow device for six different values of gas momentum at various magnitudes of base liquid Reynolds numbers (base channel 162 $\mu\text{m}$ , secondary channel 10 $\mu\text{m}$ ).....	120

Figure 6.42	Contour plot and vector plot of velocity profile in front of the orifice in a co-flow device (bases channel 150 $\mu$ m, Reynolds number 250).....	121
Figure 6.43	Plot gives the variation in superficial velocity of gas with respect to the change in superficial velocity of the base liquid in a co-flow device (base channel 160 $\mu$ m, secondary channel 10 $\mu$ m).....	124
Figure 6.44	Plot gives the variation in void fraction inside a co-flow device for five different values of gas flow rate at various magnitudes of Reynolds numbers of base liquid flow(base channel 162 $\mu$ m, secondary channel 10 $\mu$ m) .....	125
Figure 6.45	Plot gives the variation in void fraction inside a co-flow device for five different values of gas flow rate at various magnitudes of Reynolds numbers of base liquid flow(base channel 162 $\mu$ m, secondary channel 5 $\mu$ m) .....	126
Figure 6.46	Plot gives the variation in void fraction inside a co-flow device for five different values of gas flow rate at various magnitudes of Reynolds numbers of base liquid flow(base channel 162 $\mu$ m, secondary channel 25 $\mu$ m) .....	128
Figure 6.47	Plot gives the variation in void fraction inside a co-flow device for three different values of gas momentum at various magnitudes of base liquid flow Reynolds numbers (base channel 162 $\mu$ m, secondary channel 50 $\mu$ m).....	129
Figure 6.48	Plot gives the void fraction of bubble formation in co-flow device for base liquids with different kinematic viscosities (base channel 162 $\mu$ m, secondary channel 10 $\mu$ m, Gas flow rate 0.187ml/hr).....	131
Figure 6.49	Plot gives the void fraction of bubble formation in base channel for base liquids with different kinematic viscosities (base channel 162 $\mu$ m, secondary channel 10 $\mu$ m, Gas flow rate 0.145ml/hr).....	132
Figure 6.50	Contour plot of velocity profile for base liquid flow inside base channel with and without flow focusing device (base channel 150 $\mu$ m, Reynolds number of liquid flow 250).....	133
Figure 6.51	Plot gives the comparison between bubble diameters formed in co-flow devices with and without flow focusing (base channel 162 $\mu$ m, secondary channel 10 $\mu$ m, flow focusing structure height 100 $\mu$ m).....	135
Figure 6.52	Mask layouts for manufacturing different shapes of flow focusing structures inside the base channel of co-flow device. ....	136

Figure 6.53	Plot gives the comparison between bubble diameters formed in co-flow devices with three different shapes of flow focusing structures (base channel 162 $\mu\text{m}$ , secondary channel 10 $\mu\text{m}$ , flow focusing structure height 100 $\mu\text{m}$ ).....	136
Figure 6.54	Contour plot of velocity profile for base liquid flow inside base channel with different shapes of flow focusing device (base channel 150 $\mu\text{m}$ , Reynolds number of liquid flow 250).....	137
Figure 6.55	Plot gives the variation in void fraction of bubbles formed in co-flow devices with semi-circle flow focusing structure (base channel 162 $\mu\text{m}$ , secondary channel 10 $\mu\text{m}$ , flow focusing structure height 100 $\mu\text{m}$ ).....	139
Figure 6.56	Plot gives the variation in void fraction of bubbles formed in co-flow devices with triangle flow focusing structure (base channel 162 $\mu\text{m}$ , secondary channel 10 $\mu\text{m}$ , flow focusing structure height 100 $\mu\text{m}$ ).....	140
Figure 6.57	Vector plot of velocity profile for base liquid flow inside base channel with triangular flow focusing structure (base channel 150 $\mu\text{m}$ , Reynolds number of liquid flow 250).....	141
Figure 6.58	Droplet formations in cross-flow device (base channel 162 $\mu\text{m}$ , secondary channel 75 $\mu\text{m}$ ).....	142
Figure 6.59	Plot gives the variation in the droplet diameter formed in cross-flow devices with water as base fluid and Paraffin oil as secondary fluid (base channel 160 $\mu\text{m}$ , secondary channel 75 $\mu\text{m}$ ).....	143
Figure 6.60	Droplet formation in a co-flow device at various time intervals (base channel 165 $\mu\text{m}$ , secondary channel 75 $\mu\text{m}$ ).....	145
Figure 6.61	Plot gives the variation in the droplet diameter formed in co-flow devices with water as base fluid and Paraffin oil as secondary fluid (base channel 165 $\mu\text{m}$ , secondary channel 75 $\mu\text{m}$ ).....	146
Figure 6.62	Schematic of cross-flow generator with round channel and contour plot of velocity profile inside the round channel.....	147
Figure 6.63	Bubble formation in cross-flow device with round base channel. (base channel 160 $\mu\text{m}$ , secondary channel 10 $\mu\text{m}$ ).....	148

Figure 6.64	Comparison of bubble diameter obtained from a straight base channel (with and without flow focusing) and round base channel. (base channel 160 $\mu\text{m}$ , secondary channel 10 $\mu\text{m}$ , flow focusing structure (semi-circle) height 100 $\mu\text{m}$ ).....	148
-------------	---	-----



## LIST OF TABLES

Table 6-1	Physical properties of gases used in the case study.....	88
Table 6-2	Physical properties of liquids used in the case study.....	91
Table 6-3	Diameter of bubbles generated in a base channel of hydraulic diameter 162 $\mu\text{m}$ and secondary channel diameter 2 $\mu\text{m}$ .....	96

## ACKNOWLEDGEMENTS

First of all I would like to thank the almighty God for choosing me from billions to do this research. Next I would thank my advisor Dr. Hisham Hegab for guiding me through the project and providing me with an excellent lab facility for the completion of the research. Without his valuable advice and expertise this project would never have been a success. I also thank him for the freedom of thought he has given me during the project, which helped me to develop as a better researcher over, the last four years. I thank my committee, Dr. James Palmer, Dr. Long Que, Dr. Despina Davis, and Dr. Sandra Zivanovic for the help and support they offered me during the project and for being on my committee.

I would like to thank my colleague, Mr. Bobby Mathew, for helping me throughout my research. I also thank Dr. Chad O'Neal for allowing me to use his lab. I also express my gratitude to Mr. Joel Soman, Mr. Ji Fang, and Mrs. Ancy Kunjumon for helping and supporting me at various stages of this project.

Finally, but not least, I would like to thank my wife, Sheethal Susan John, for supporting me during the laborious part of this work. Without her whole hearted support I would have found it difficult to finish this project. I express my gratitude to my sister and brother-in-law who supported me morally over the last four years. My parents and my entire family including my in-laws deserve my gratitude for support they have provided me during my stay at Louisiana Tech University.

# CHAPTER 1

## INTRODUCTION

### 1.1 Bubble/Droplet Generators

Generation of microbubbles and droplets in micro channels and their applications are areas of research which have been undergoing extensive research in the last two decades [1-11]. Microbubbles or microdroplets refer to small gas or liquid filled spheres dispersed in a liquid medium with size preferably less than 100 $\mu\text{m}$  in diameter. What makes the generation of microbubbles and droplets an interesting area for researchers is the wide area of applications that they have in the modern fields of engineering [1-10]. Microbubbles have the capability of dissolving in liquids very abruptly, thus allowing a complete change from gaseous form to liquid form in a very efficient manner. One of the most potentially useful applications of microbubbles developed recently, based on its phase changing capability, is the direct oxygenation of the blood [1]. Researchers have shown that a microbubble of a diameter less than 20 $\mu\text{m}$  will escape the pulmonary filtration and will dissolve in blood within 5 seconds [1]. This application, if used effectively, can eliminate the use of mechanical ventilators which cause damage to the lung tissues during treatment of acute respiratory distress syndrome (ARDS). It is estimated that 190,000 people are affected by ARDS annually, out of which 74,500 deaths are reported every year [1]. Other biomedical applications of microbubbles include

ultra sound activated microbubble for cancer detection and treatment, targeted drug delivery for cells, and gene therapy [2, 3]. Microbubbles, when accumulated in cancerous regions, or regions with tumor, can be imaged by passing ultrasonic radiations through the microbubbles. Drug delivery by microbubbles involves coating the bubble using desired chemicals in micro channels using the layer by layer assembly [4]. Using a microbubble as a biomedical valve is another potential application [5]. The use of microbubble/droplets in chemical reactors enables the precise mixing of the chemicals in micro reactors, which enhances the reaction rate, reduces the amount of reactants, trims down processing time, increases the ease of reactions and reduces the expense of reactions by increasing throughput [6]. It has been demonstrated recently that the properties of many polymer materials can be controlled by the use of microdroplets generated in micro channel [7]. The concept of micro mixers which evolved in this decade requires precise control of the droplet/bubble volume for its flawless operation [8]. The most recent application involving droplets is the micro and nano manufacturing of 3D structures (prototyping) [9, 10]. Few researchers have successfully demonstrated the manufacturing of nano and micro wire and 3D structures using the droplet merging techniques [9, 10]. All the above discussed applications need precise control of the bubble/droplet size for the successful implementation. Thus understanding the dynamics behind the bubble/droplet formation and investigating new efficient methods to generate smaller bubbles/droplets in micro channels is very significant for various fields of engineering.

### **1.1.1 Overview on the current bubble/droplet generation methods**

The methods used to form microbubbles and droplets have evolved into two categories over the last decade [11-13]. The first category, termed the active method, involves the formation of a microbubble/droplet using some form of an external actuation mechanism. This mechanism acts either on the microbubble/droplet or on the orifice, which helps the droplet/bubble detachment [14-16]. An external activation mechanism can be of any type, such as thermal actuation, pressure actuation, etc. The need for external actuation makes the implementation of the active bubble/droplet generation method very complicated. The study presented in this dissertation deals with the second category, known as the passive method. This method uses the viscous stress acting on the bubble/droplet (during its formation) by the pressure driven flow in micro channels to help its detachment [18, 23-47]. Passive microbubble/droplet generation is further classified into three sub-types based on the direction of the fluid flows in the micro channels: co-flow bubble/droplet generation, focused flow bubble/droplet generation, and cross-flow bubble/droplet generation [11]. The liquid into which the bubble/droplet is dispersed is referred to as the base fluid, and the liquid or gas which makes up the bubble/droplet is referred to as the secondary fluid throughout this study. Likewise the micro channel carrying the base fluid is termed the base channel and the micro channel carrying the secondary fluid is termed the secondary channel. The base fluid flows continuously in the micro channel and helps the detachment of a bubble/droplet by exerting viscous stress on the droplet/bubble during its growth. Figure 1.1 presents the schematic representation of current bubble/droplet generators.

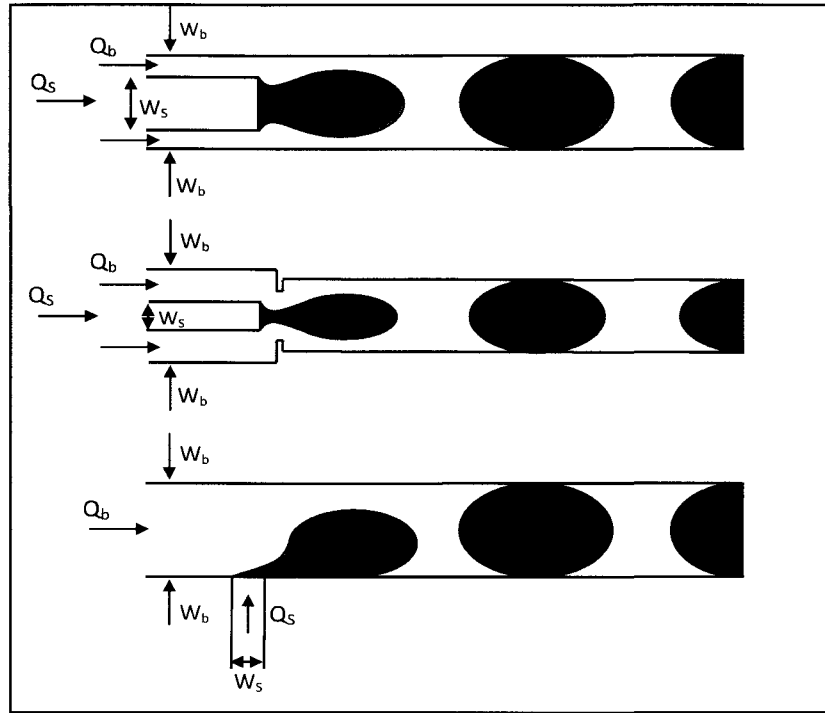


Figure 1.1 Schematic diagram showing co-flow, focused flow and cross-flow bubble/droplet generators

In the co-flow bubble/droplet generation method, the micro channel carrying the secondary liquid is placed inside the base micro channel (Figure 1.1) [18, 26, 36, 39]. Both the fluids flow in the same direction, and the viscous stress enforced by the base fluid on the sides of the secondary liquid will cause the detachment of the bubble/droplet from the orifice. The focused flow devices use the principle of co-flow bubble/droplet generators, but make use of some geometric modifications of the base channel [37, 38, 40-43]. This arrangement helps the flow of base liquid around the secondary channel to be focused at the orifice, and thus gets more viscous stress applied on the bubble/droplet during formation. In the cross-flow bubble/droplet generation method, the secondary liquid enters the micro channel carrying the base liquid through a micro channel, which is placed perpendicular to it [30-35, 44, 45]. This arrangement forms a T-junction where the

bubble/droplets are generated due to the viscous stress of the base fluid acting on the secondary fluid during bubble/droplet formation. All the different forces acting on the microbubble/droplet during its formation are discussed in the Chapter 3. Figure 1.1 shows the schematic representations of the co-flow bubble/droplet generation method, a commonly used flow focusing method and cross-flow bubble/droplet generation method, respectively.

Compared to the active method the passive method has the advantage of ease of implementation and the capability of generating uniform sized microbubble/droplets during consecutive intervals [1]. However, the major disadvantages are the formation of satellite bubble/droplets, which are small bubble/droplets that form and follow the mother bubble just after the detachment of the mother bubble/droplets. The passive method also needs high pumping power to establish flow through the micro channels [11, 21, 33]. Few researchers have tried to address this problem by properly tuning the bubble/droplet formation either by using modified geometries inside the micro channels (for co-flow) or by limiting the bubble/droplet formation to certain regions of the liquid flow rates [37-39, 40, 42].

### **1.1.2 Limitations of the current bubble/droplet generators**

Even though bubble/droplets are used in numerous applications, such as lab on chip, layer by layer assembly, drug delivery, chemical mixing, etc, the characterization of the bubble/droplet generating mechanism has not reached a satisfactory level which can be used by the scientific community [11, 12]. For example, in the co-flow and flow focusing devices, there is not a single mechanism which can predict the detachment of the bubble/droplet from the orifice [11-13]. In the cross-flow device, viscous stress and

interfacial tension between the liquids are considered to be the most dominating factors in the detachment mechanism of the bubble/droplet, and certain models have been developed based on this mechanism [26, 27]. However, these assumptions are taken from the macro level experiments done in the last decade and have not been experimentally validated in the micro channels until now [11, 17, 18]. The major limitations of the current methods used for the generation of microbubble/droplets are listed below.

### 1.1.2.1 Bubble/droplet confinement

The major constraint that adds to the complexity in the prediction of the bubble/droplet detachment mechanism and detachment diameter is the bubble/droplet confinement inside the base channel, which in turn is due to the size of the bubble/droplet. This size is often bigger than the hydraulic diameter of the micro channel in which they are formed [18, 29-43]. Figure 1.2 shows a bubble that is being confined in a micro channel and Figure 1.3 represents a cross-flow bubble generator with micro channels of same depth.

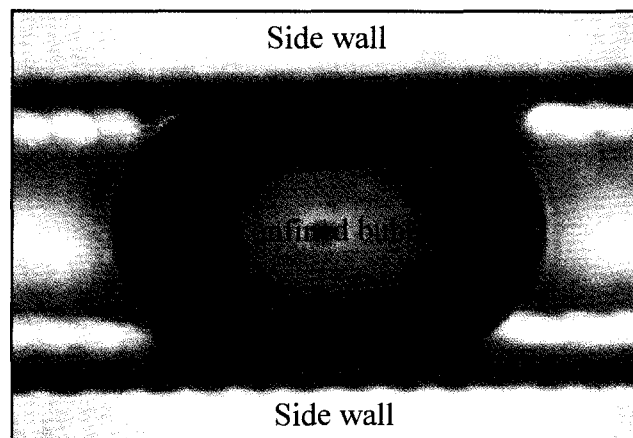


Figure 1.2 Microbubble confined inside a micro channel [45]



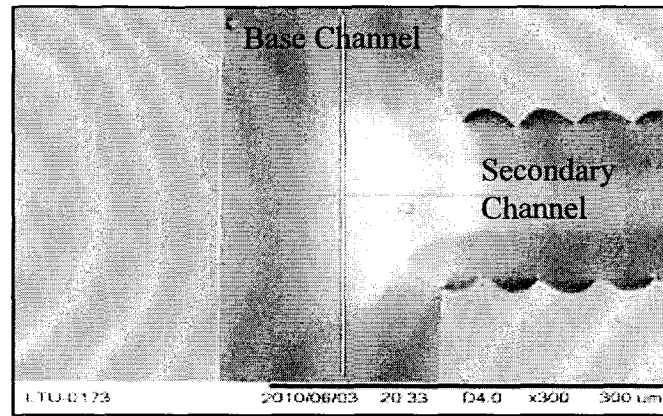


Figure 1.3 T-junction bubble/droplet made with same depth micro channels

In all currently available passive bubble/droplet generation methods, the base channel and the secondary channel are of the same depth [17-22, 29-33]. Consequently, as the bubble/droplet starts to grow inside the base channel, it is already confined to both the top and the bottom walls of the base channel. And, as the bubble/droplet continues to grow this confinement effect increases. In addition, depending on the ratio of flow rate of the base fluid to that of the secondary fluid, the bubble/droplet can get confined to the sidewalls of the base channel as well. Thus, if this ratio is high, the bubble/droplet will get confined to all the four walls of the base channel, blocking the entire flow through it (Figure 1.2). If the ratio is low, the bubble/droplet will get confined only by the top and bottom walls of the base channel. The transition between the confined bubble and unconfined bubble is given by Thomas Cubaud and Chih-Ming Ho in 2004 (Equation 1.1) [49].

$$\alpha_L = \frac{Q_L}{Q_L + Q_G} \quad (1.1)$$

The transition between the unconfined and the confined bubble occurs when the value of  $\alpha_L$  approaches 0.75 [49]. Here  $Q_L$  and  $Q_G$  represent the flow rate of liquid and

gas through the micro channels. In the case of cross-flow devices, the bubble/droplet will get confined to one of the side walls even at small ratios of liquid flow (as can be observed from Figure 1.1). The confinement of the bubble/droplet on the channel walls will require some extra force from the base fluid to get the bubble/droplet detached from the orifice, due to the interaction between the channel wall and the bubble/droplet. In addition, when the bubble/droplet gets confined to the channel walls, a thin layer of the base liquid is assumed to be formed between the walls and the bubble/droplet, preventing the bubble/droplet from being attached to the walls [20]. This phenomenon demands the usage of a fully wettable surface for the base micro channel and increases the complexity of both mathematical modeling and experimental setup [19, 20]. It has been reported in the past that if both the liquids wet the channel surface comparably, the bubble/droplet formation in the device will not be uniform in size. This effect increases as the size of the channel decreases [11]. Even though some models were proposed to predict the bubble/droplet detachment (for cross-flow) with the confinement effect, none of them provided a complete characterization of the detachment conditions with experimental validation [30, 35]. Few researchers have tried to overcome the issue of bubble/droplet confinement by making the width of the secondary channel small compared to the base channel. But none of them was able to solve the confinement problem. Other studies tried getting around this problem by using both the base and secondary micro channel of lesser depth compared to the width of the channels [33, 37, 40]. This approach helped in reducing the confinement effect of the bubble/droplet on to the side walls, but increased the confinement of the bubble/droplet on to the top and the bottom walls of the base micro channels, and forced the bubble/droplet to take a disk shape [37]. In conclusion,

none of these studies really helped in reducing the complexity of developing a model which can characterize the bubble/droplet detachment criteria and diameter at the detachment of the bubble/droplet.

#### **1.1.2.2 Merging of consecutive bubbles/droplets**

A major limitation caused by the bubble/droplet confinement effect is the merging of the subsequent bubble/droplet close to the orifice. Merging of the bubble/droplet happens just after the detachment of the bubble/droplet from the orifice. The with a bubble/droplet that is confined to the liquid channel walls moves along the base channel reduced velocity compared to the base liquid velocity. The reduction in the bubble/droplet velocity is mainly due to the bubble/droplet interaction with the channel walls. To a lesser extent, this is due to the decrease in the superficial velocity of the bubble/droplet caused by the increased cross-sectional area of the bubble/droplet. Since the subsequent bubble/droplet formation at the orifice is not affected by the reduction of the bubble/droplet velocity of the previously detached bubble/droplet, it continues to grow at a normal velocity. This phenomenon ends up in the merging of the successive bubble/droplet. As the confinement of the bubble/droplet increases, the number of bubbles being merged into the previously detached bubble/droplet increases. As the confinement of the bubble/droplet increases, the number of bubbles being merged into the previously detached bubble/droplet increases. The bubble/droplet merging causes the bubble/droplet to increase its diameter even after its detachment from the orifice, making the prediction of the bubble/droplet diameter more complicated. This issue was first observed and reported during the research work conducted for this study and is explained further in the later chapters. Figure 1.4 represents the bubble merging issue.

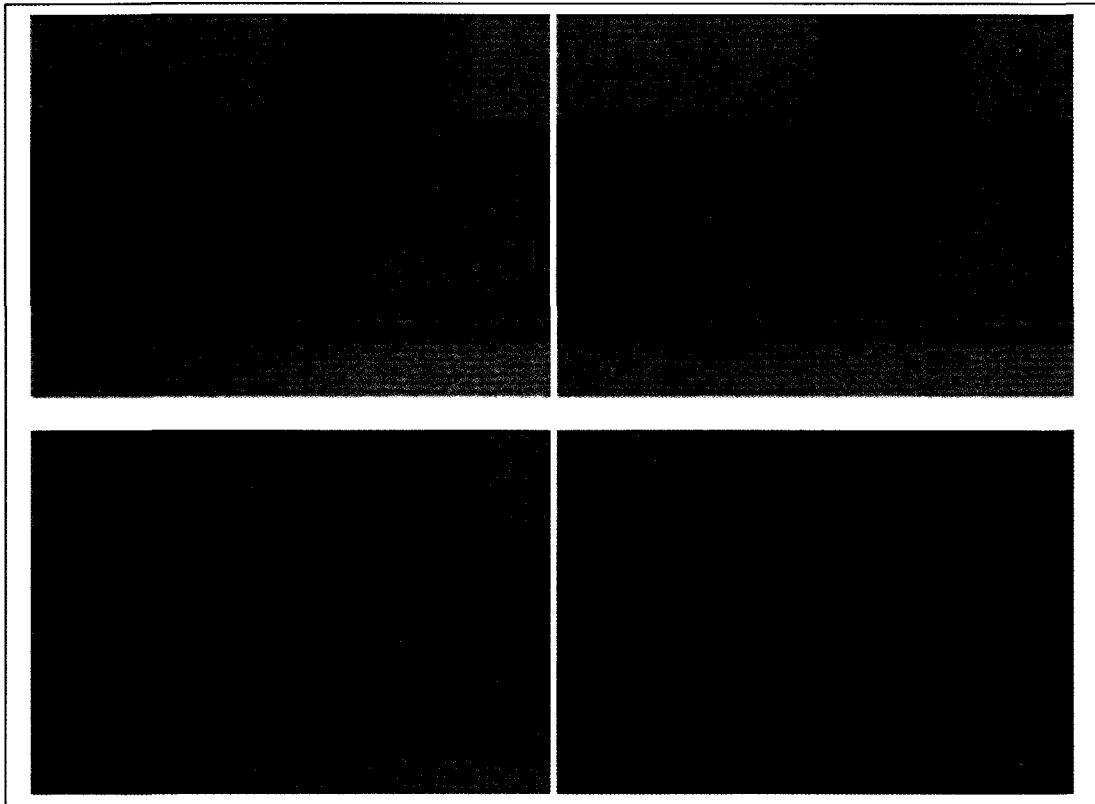


Figure 1.4 Consecutive microbubbles merging with each other right after getting detached from the orifice

### 1.1.2.3 Bubble diameter and satellite bubble formation

Another major issue associated with the usage of micro channels of the same depth for both base and secondary channel of the bubble/droplet generator is the constraint it automatically generates on the minimum size of the microbubble/droplet that can be produced. For both the co-flow and the cross-flow bubble/droplet generators, the minimum size of the bubble/droplet generated depends on the hydraulic diameter of the secondary channel. The bubble/droplet is assumed to detach from the orifice when the neck length of the bubble/droplet becomes equal to the diameter of the orifice from which it is generated [24, 26]. To obtain uniform sized bubble/droplet at regular intervals and to avoid satellite bubble/droplet formation, the diameter of the bubble/droplet generated

should be greater than the hydraulic diameter of the secondary channel. In an effort to overcome this issue, researchers started using micro channels of smaller dimensions at a cost of increasing the pressure drop across the channel. The focused flow bubble/droplet generators can solve the problem to an extent, but this technique increases the frequency of the satellite bubble/droplets following the mother bubble/droplets [31, 34, 36, 43].

#### **1.1.2.4 Determination of bubble diameter**

Additionally, the accurate determination of the diameter of the bubble/droplet formed using the existing bubble/droplet generators is a major concern as the bubble/droplet generated is not spherical. Though several effective methods for determining the volume of the bubble/droplet formed inside the micro channels have been proposed, the exact determination of the bubble/droplet diameter increases the complexity of the prediction model [33, 38, 39]. The usage of image processing software helps in reducing the complexity of calculating the bubble/droplet size experimentally, but the complexity of bubble/droplet size prediction using a mathematical model still remains high [33, 37].

## **1.2 Research Objectives**

Even though a broad investigation on the parameters that affects the bubble/droplet formation in micro channels is included in the current study, the main objective of this work throughout its phases is to generate microbubbles of size less than  $15\mu\text{m}$  in diameter for the purpose of the direct oxygenation of blood as discussed earlier. Microbubbles of dimensions less than  $15\mu\text{m}$  in diameter will dissolve in liquid (blood) in less than 5 seconds [1]. This phenomenon can be used to oxygenate blood directly without the help of mechanical ventilators, and thereby provide better options for the

treatment of medical conditions like acute respiratory distress syndrome. The secondary objective of this work is to produce and understand the mechanism behind the formation of unconfined bubble/droplets inside micro channels for a wide range of fluid flow rate through both the base and secondary channels and thereby overcome the limitations like bubble/droplet confinement discussed in the Section 1.1.

For attaining both the above objectives, a new technique was introduced in this study for the generation of fully spherical unconfined bubble/droplets inside a micro channel. The new technique can be used for both cross-flow and co-flow bubble/droplet generation methods. The microbubbles/droplets generated using the new technique are further used for understanding the phenomenon behind the bubble/droplet generation in micro channels. The experimental results obtained from the new technique are used to validate the mathematical model developed for cross-flow bubble generation model. The mathematical model is capable of predicting the formation of the microbubbles, diameter at detachment, and the detachment criteria (the main forces which are dominating the bubble detachment mechanism). A numerical model is also developed to study the feasibility of using flow focusing technique inside the cross-flow bubble/droplet generator.

The third objective of this work is to introduce flow focusing inside the cross-flow bubble/droplet generators and obtain smaller bubble/droplets at lower Reynolds number of the base fluid compared to the models which do not use the flow focusing techniques. This technique will provide a method to create small unconfined bubbles/droplets at a lower liquid pumping power through the base micro channel. The current work is the first ever reported study which introduces flow focusing in a cross-flow micro channel bubble/droplet generator. The flow focusing technique is

implemented in both cross-flow and co-flow devices and an optimization of flow focusing structure geometries are carried out during the study.

### 1.2.1 New generation bubble/droplet generators

The basic concept behind the new generation of bubble/droplet generators introduced in this work is to use secondary channels which have a hydraulic diameter much smaller than that of the base channel. The schematic for the new generation bubble/droplet generators for both co-flow and cross-flow devices is shown in Figure 1.5.

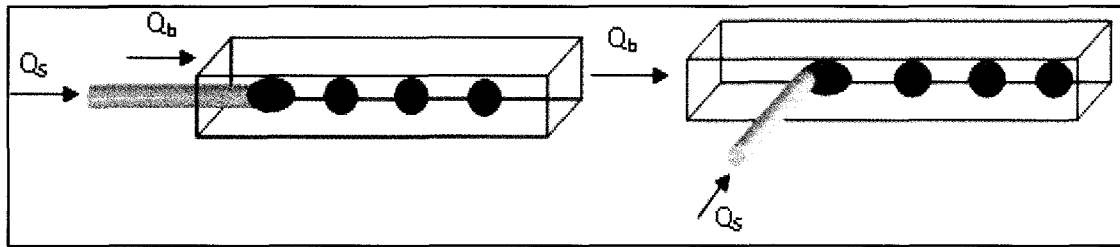


Figure 1.5 Schematic representation of the new generation bubble/droplet generator in co-flow and cross-flow device

The new concept is improvised into a device form by using fused silica tubes with less inner diameter than the hydraulic diameter of the base channel as the secondary channel. The outer diameter of the fused silica tube is selected at the same depth as the base channel. The manufacturing techniques involved in the development of new generation bubble/droplet generators are explained in Chapter 4. Using a fused silica tube as the secondary channel has two advantages. First, the hydraulic diameter of the secondary channel can be selected anywhere from  $2\mu\text{m}$  up to the desired range according to the application of the bubble/droplet generator. This provides the flexibility of attaining unconfined bubbles inside micro channels at very low Reynolds numbers of base liquid flow. The second advantage comes with the alignment of the orifice to the

base channel wall. Aligning the fused silica tube towards the side wall of the base channel positions, the orifice of the bubble/droplet generator at the center of the side wall, which is very important for the generation of the unconfined microbubbles/droplets.

The inner diameter of the fused silica tube can be selected from a wide range of values from  $2\mu\text{m}$  and above. Since the orifice diameter of the secondary channel is the same as that of the inner diameter of the fused silica tube, the bubble/droplet formation will not be confined to any channel walls. A fully spherical bubble/droplet will start growing from the orifice, and the detachment will take place before it gets confined to any of the channel walls. During the initial stages of the study, the inner diameter of the fused silica tube is selected in such a way that it is less than the base micro channel diameter by at least by a factor of 5 for air bubbles and by a factor of 2 for the bubble/droplet. This eliminates the chance of the bubble/droplet touching the side walls of the channel even at low values of Reynolds number of liquid flow. The confinement can happen only if the velocity of the base fluid is low compared to the velocity of secondary fluid, and this threshold ratio for a wide range of base channel to secondary channel ratio is found out experimentally and is discussed in Chapter 6. The fabrication steps involved in the development of the bubble/droplet generators with fused silica tube as the secondary channel is explained in Chapter 4.

The new technique introduced for bubble/droplet generation is used in the development of both the cross-flow and co-flow devices. The dimension criteria between the orifice diameter and base channel hydraulic diameter is kept same for both the cross-flow and co-flow devices. In the new generation bubble/droplet generators, the base liquid flow is more well distributed around the bubble/droplet during its formation



(unlike in the currently used droplet/bubble generators). This generator, in turn, will limit the elongation of the bubble/droplet neck from the orifice into the base channel, thus helping it to get detached from the orifice at a smaller diameter. This phenomenon will also help to eliminate the satellite bubble/droplet formation after the mother bubble/droplet gets detached. The satellite bubble/droplets are caused due to the elongation of the bubble/droplet into the base channel [33].

### **1.2.2 Flow focusing in cross-flow bubble/droplet generators**

Flow focusing is a technique currently being used in co-flow bubble/droplet generators to improve their performance. In the current study, a flow focusing technique is introduced into the cross-flow bubble/droplet generation device by modifying the base channel geometry to get the base fluid flow focused onto the orifice of the bubble/droplet formation. This flow focusing technique will help the bubble/droplet to get detached from the orifice at a smaller diameter than in the normal cross-flow devices with same channel dimensions. Until date flow focusing was limited to the co-flow devices. This technique has the advantage of getting smaller bubbles/droplets at same Reynolds number of base liquid flow inside channels of same dimensions compared to the one without flow focusing structures. A schematic representation of the flow focusing technique in the cross-flow device is given in Figure 1.6.

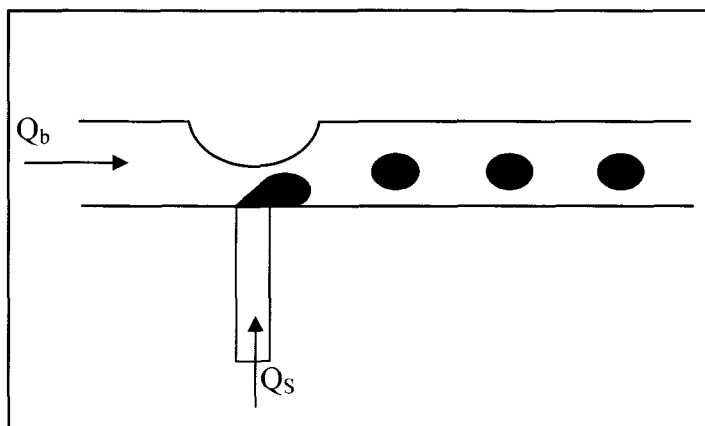


Figure 1.6 Schematic representation of flow focusing technique in a cross-flow bubble/droplet generation device

As can be seen in Figure 1.6, a semi-circular shape is introduced in front of the orifice so that the local liquid flow velocity is increased, which increases the viscous stress that is being applied to the bubble/droplet during its formation. The increased base liquid velocity will reduce the absolute pressure in front of the orifice, thereby helping the growth of the bubble/droplet. The flow focusing technique has the advantage of generating smaller bubble/droplets in bigger channels without much increase in pressure drop across the base channel. An optimization based on the shape and size of the flow focusing structures is carried out in this study, and the corresponding numerical and mathematical models are developed for the prediction of the bubble/droplet formation and detachment diameter.

## **CHAPTER 2**

### **LITERATURE REVIEW**

This chapter gives a brief literature review of bubble/droplet generation study done in the past. Some relevant macro level bubble/droplet generation studies from 1960 to this decade are also included in this review because most of the assumptions used in the micro level study is adapted from the macro level research done in the past. Relevant studies on microbubble/droplet generation using both cross-flow and co-flow technique in this decade are reviewed and presented in the order of publication date.

#### **2.1 Macro Level Bubble/Droplet Generators**

The study of the bubble/droplet generation and detachment in macro scale started in the late 1960's. One of the first works which studied bubble generation in stagnant liquid was reported in 1969 by Ramakrishnan, Kumar and Kuloor [23]. Since then, the study of bubble generation, in macro scale both mathematically and experimentally, and in stagnant as well as flowing water has been carried out by several researchers. Volume of the bubbles formed from a single orifice in horizontal flowing liquid was investigated by Nojima et.al in 1981 [24]. The study was conducted for constant gas flow rate for different gas chamber pressures. A mathematical model supported by empirical results was put forward by the researches based on some assumptions. The major assumptions

were that the bubble formation was spherical, and that the bubble moves at the same velocity of the base liquid after its detachment from the orifice. The study concluded that bubbles of smaller size can be generated in the flowing liquid (compared to the stagnant liquid), and the moving liquid has no effect on the bubble formation during the initial stages of its growth. Marshall and Chudacek proposed a mathematical model in 1993 which used potential flow theory to study the bubble formation from an orifice in cross flowing liquid [25]. The results obtained by solving the mathematical model were compared with the experimental results and were validated. The liquid inertia force was found to be the major factor in determining the single bubble growth. Bhunia et al. studied the bubble formation using a co-flow device both under normal and reduced gravity in 1998 and proved that the gas momentum flux, buoyancy, surface tension and drag force were the important factors affecting the bubble growth and detachment [26]. Nahra and Kamotani studied bubble formation in cross current liquid flow under reduced gravity conditions in 2000 [27]. They developed a simple mathematical model to predict the bubble formation, and experiments were conducted to support the mathematical model. They separated the force acting on the bubbles during its formation into two types, attaching forces and detaching forces. The study showed that the bubble detaches from the orifice when the sum of detaching forces, such as gas momentum, overcomes the attaching forces, such as the liquid drag and inertia. The study also stated that the surface tension does not have much effect on the detachment criteria, as the bubble shifts its location from the orifice along the liquid flow even before the detachment happens. The study also proved that the inclination angle of the bubble formation plays a major part in determining the forces that affect the bubble detachment from the orifices.

Later, in 2002 they came up with an improved model for the prediction of bubble growth and detachment diameter [28]. The study was further extended to bubble formation under normal gravity. A new improved force balance equation with x and y dimension was developed during the study. Experiments were conducted under both normal and reduced gravity conditions to validate the mathematical model. The study showed that under normal gravity buoyancy is also a major force acting on the bubble during its formation and detachment. However, the scope of the study was limited to the prediction of the bubbles which had a diameter of 50% of the hydraulic diameter of the liquid channel in which they were formed. The bubbles were assumed to be almost spherical during their formation, and the model cannot predict the formation of significantly deformed bubbles during its formation. Sadatomi et al. developed a microbubble generator in 2004 using a macro scale cylindrical tube with a spherical body inserted into it [29]. Water was pumped into the cylindrical tube with a spherical body, causing a very high velocity of the water flow around the spherical body. High velocity causes the absolute pressure around the spherical body to drop below the atmospheric pressure, and this reduced pressure pulls air through the nozzles placed around the spherical body in the tube. The turbulence generated by the high velocity of water breaks down the sucked in air bubbles into microbubbles. Although this method provided an easier method to generate microbubbles, it lacked control over the size of the microbubbles being generated inside the tube. An optimum size of the spherical body to be used in a known diameter of tube to generate microbubbles was developed from the work with the aid of experimental data.

## 2.2 Micro Level Cross-flow Bubble/Droplet Generators

Sung Sam Kim, in his Ph.D. dissertation, "Generation of Oxygen Microbubbles in a Micro Channel With Cross Current Liquid Flow," in 2001 studied the generation of microbubbles in micro channel using the cross-flow technique [47]. The micro channels were made of silicon wafer, and the orifice was made using an ion milling technique at the top corner of the side wall of the micro channel. The objective of the work was to generate microbubbles of less than  $20\mu\text{m}$  in size consistently, but failed to achieve its objective. The study was able to produce microbubbles around  $45\mu\text{m}$  in diameter, using variable gas pressure in a chamber close to the orifice. The major drawback of the study was the manufacturing constrains which restricted the researchers from aligning the orifice towards the center of the side wall of the base channel. Even though the study was not able to produce microbubbles of the desired size, the study provided a good stepping stone towards the current study presented in this dissertation.

Graaf et al. studied the droplet generation in cross-flow droplet generators both experimentally and numerically in 2006 [30]. The Lattice Boltzmann method was used to study the droplet formation and transportation through the micro channel numerically. The flow profile and the wetting boundary condition were validated by the experimental data generated during the study. The study analyzes the similarity in the shape of the droplet formation in both the numerical and experimental model, but lacks a good comparison of the droplet diameter and detachment frequency between the numerical and the experimental results. A parametric optimization based on the interfacial tension between the two fluids and liquid flow rate through both the channels was also included in the study. Husny and Cooper-White studied the elasticity effect of the droplet

formation in the cross channel droplet generators in 2006 [31]. The study showed that the pressure balance between the base and the secondary channel governs the droplet formation in the initial stages. But as the droplet grows bigger, the drag force will dominate its formation and detachment. The same observation was made by Nahra and Kamotani in 2000 [27]. They also studied the effect of the viscosity ratio between the base and the secondary fluid, and concluded that the usage of an elastic secondary fluid will result in the formation of the satellite droplets. Menech et al. studied the droplet formation in micro channels in 2007, and classified the droplet formation into three regions based on the capillary number; squeezing, dripping and jetting [32]. At low values of capillary number, squeezing occurs and is governed by the pressure upstream of the secondary liquid. Dripping occurs at the intermediate values of capillary numbers and is also affected by the channel dimensions. Jetting will occur only at very high values of capillary numbers.

Zhang and Wang experimentally studied the bubble formation in the cross-flow micro channel in 2009 [33]. Bubbles formed in the study were of quasi cylinder shape due to the small aspect ratio of the channels. The experiment found that both the capillary number and the pressure drop inside the base channel (from the T-junction to the outlet of the base channel) influence the bubble formation and bubble volume. The bubble volume was found to decrease exponentially with the increase in the capillary number. Xiang and LaVan studied the formation of droplet in micro channel numerically using the CFD package COMSOL in 2009 [34]. The authors reported that the results from their model were in agreement with the CFD models and that the maximum deviation is only 10%. But the results of the model showed considerable variation from the experimental results.

A two dimensional mathematical model was developed by T. J. John et.al for predicting the formation of a gas bubble and its diameter at detachment inside a micro channel in 2009 [44]. The model was developed by considering all the forces that act on the bubble during its growth, and the detachment was predicted to happen when the sum of all the attaching forces equals the sum of all detaching forces. This same approach was used by some previous researchers [27, 28]. A bubble detachment criterion was developed by matching the forces acting on the bubble using the trigonometric relation between the sides of a right triangle. This method was adopted from a previous work done in 2001 by Sung Sam Kim [47]. Substituting the expressions for each forces acting on the force balance equation and rearranging the equation gave the final expression for determining the bubble formation and diameter of the bubble at detachment. The equation obtained for predicting the bubble formation in the normal micro channel under cross fluid flow was modified to predict the bubble formation and bubble diameter for micro channels with flow focusing techniques. More than developing a mathematical model for the prediction of bubble formation the study introduced the benefit of using flow focusing in the cross-flow bubble generators for the first time. In order to study the feasibility of introducing flow focusing techniques in the bubble generators a 2D numerical model was developed using the CFD software COMSOL by T. J. John and H. Hegab in 2009 [45]. The model studied the bubble generation inside the micro channel with and without flow focusing technique for a range of liquid flow through the base channel. The gas flow through the secondary channel was kept constant. Level set function, which is a numerical method used to track the change in the interfaces between water and air, was used to determine the interface between the bubble and base liquid.



The effect of the droplet diameter on the shape of the flow focusing structures was also studied using three different shapes: semi-circle, triangle and full circle (kept at the middle of the base channel, so that liquid will flow through both sides). The semi-circular structures showed the best performance as the flow focusing structure. It was observed that as the diameter of the semi-circle increased, the size of the bubble decreased.

Timgren et al. developed a force balance model to predict droplet generations inside a cross-flow droplet generator in 2010 [35]. Experimental work for the purpose of validation was done in micro channels made out of PDMS material. The study concluded that the major factor influencing the formation of the droplet is the pressure driven force acting on the droplet by the secondary fluid and, at high values of capillary number, the neck of droplet extends more into the base channel. In 2010 T.J. John and H. Hegab introduced a new generation of cross-flow microbubble generators, which can produce unconfined spherical bubbles in a micro channel at low Reynolds numbers of liquid flow through the base channel [48]. The base micro channel was made of a silicon wafer and fused silica tube with an inner diameter of  $20\mu\text{m}$  was used as the secondary channel. The paper demonstrated some initial results in which bubbles of around  $100\mu\text{m}$  were produced in micro channels of hydraulic diameter  $360\mu\text{m}$ . Luo. G. S. et al. studied the microbubble generation in a T-Junction micro channel in 2010 [50]. The base channel was made of PMMA material by micro milling, and the smallest dimension used was  $600\mu\text{m}$ . A metal capillary tube was used as the secondary channel, and the inner dimension of the tube used was  $190\mu\text{m}$ . Flow focusing was introduced inside the base channel by extending the secondary channel into the base channel, and its effect on the bubble diameter formed was studied. Microbubbles of a size as low as  $100\mu\text{m}$  were

produced by the flow focusing technique. Huai Z. Li et al. investigated the regions of bubble formation in the T-junction micro channel in 2010 [51]. The micro channels were 160 $\mu\text{m}$  wide and 40 $\mu\text{m}$  deep and were made on a glass plate using standard photolithography and chemical wetting techniques. Three regions of bubble formation, squeezing, dripping and transition regimes, based on dimensional numbers like gas to liquid flow rate ratio, capillary number etc., were identified in the device.

### **2.3 Micro Co-Flow and Flow Focusing Bubble/Droplet Generators**

Carmer et al. studied the droplet formation from a co-flowing droplet device using a capillary tube as the secondary channel in 2004 [36]. The base channel was of macro scale (20mm high, 2.5mm wide and 200mm in length). The study investigated the effect of droplet formation on factors such as flow rates of fluids, interfacial tension, and viscous ratio between the two fluids, and concluded consequently that interfacial tension is the main attaching force acting on the droplet. The droplet tends to form a spherical shape. At high values of viscosity, ratio satellite droplets were observed in the channel. However, the study lacked the support of a mathematical model to study the droplet behavior. A group of researchers from Harvard University and the University of Toronto studied the bubble formation in a micro channel using a flow focusing device [37]. The structure was made of PDMS material, and water was filled in the channel soon after its bonding to ensure the hydrophilic character of the base channel walls. The bubbles were disk shaped and were mono dispersed into the base channel. The study mainly focused on the proof of concept, and it concluded that the major factors affecting the bubble generation included not only interfacial tension and viscous force.

Xiong et al. studied the bubble generation in a micro channel with co-flow technique [38]. In this study, the secondary channel was located towards one side of the base channel so that the base fluids interacted with the secondary fluid (air) only through one side. Syringe pumps were used to disperse both the base and the secondary fluid into the channel. The bubble formation and detachment were studied for different viscosities and surface tensions. The same group extended their work by adding CFD simulations to reinforce the experimental work in 2007 [39]. However, the bubbles formed had a capsule shape, and in addition, the paper didn't provide a good comparison between the simulation and the experimental results. Hashimoto et al. studied the feasibility of coupling parallel flow focusing devices into one device in 2008 [40]. The structures were made of PDMS materials, and measures were taken to avoid the wetting of the base channel walls by the secondary fluid. The study proved that the coupling of more than one flow focusing device, to get, multiple bubbles did not affect the bubble formation in the channel. Saeki et al. in 2008 studied the formation of the droplet from a co-flowing device having elongated thread like the flow of the secondary fluid [41]. Even though the study didn't reveal any new information about the droplet formation other than the ones already observed and published, the integration of multiple channels in one device was demonstrated in the study. Dietrich et al. experimentally investigated the bubble formation in the micro channel with three different flow focusing devices using micro PIV in 2009 [42]. The work was supported by the CFD simulations and concluded that the main factor influencing the bubble pinch off from the orifice is the pressure difference between the two phases. The bubble formation and detachment mechanism in flow focusing micro channels was investigated experimentally and numerically by Taotao et

al. in 2009 [43]. The study also focused on the formation of the satellite droplet formation, and concluded that the satellite droplet formation depended on the elongation of the secondary fluid into the base channel.

This brief review of the publications on the cross-flow, co-flow and the focused flow devices published in the last decade shows that the mechanism of the droplet formation in a co-flow device is not completely characterized until now. Almost all of the models produced confined bubble/droplets inside the micro channel. A mathematical model that can predict the droplet formation in the co-flow device is yet to be developed. None of the devices or models (either co-flow, cross-flow or focused flow) to date were successful in generating a fully spherical droplet inside a micro channel and interpreting the droplet formation mechanism and the detachment mechanism to an acceptable level.

## CHAPTER 3

### THEORETICAL MODEL

The bubble/droplet formation in cross-flow liquid flow has been studied under normal and reduced gravity throughout last two decades [25, 27, 28]. However, almost all of these studies were confined to the macro scale bubble formation. Few researchers have tried to develop a mathematical model for the prediction of bubble/droplet formation in micro channels [30]. A general approach used in the development of the model for the prediction of bubble formation in cross-flow bubble generation is by considering the forces acting on the bubbles, and balancing the forces according to the direction in which they act on the bubble during its formation [27, 28]. This approach has been widely used, but very few have tried to experimentally validate it in the micro level bubble/droplet formation. Sung Sam Kim developed a mathematical force balance model for bubble generation in micro channels in his Ph.D. dissertation in 2001 [47]. The model was based on variable gas flow rate and was achieved by placing a gas chamber near the orifice of bubble formation. The gas pressure inside the chamber varies with the bubble formation. The model was supported with the help of experimental data, but it suffered a considerable variation from the experimental data. T. J. John et al. developed a two dimensional mathematical model using the same approach to predict the bubble formation in micro channels with the constant gas flow method [44]. The constant gas

flow was attained by using an infinite long gas channel (compared to the hydraulic diameter of the secondary channel) connected to a pressurized gas chamber. The model was further modified to study the effect of introducing flow focusing inside the base micro channel. The developed model is presented in the Section 3.1.

### 3.1 Microbubble Growth and Detachment Model

The forces acting on the bubble during its formation can be classified into two types according to the direction in which it is acting. The forces acting in favor of the bubble formation can be classified as detaching forces, and those obstructing the bubble formation can be classified as attaching forces. Each of the forces acting on the microbubbles and the direction of each force is represented in Figure 3.1.

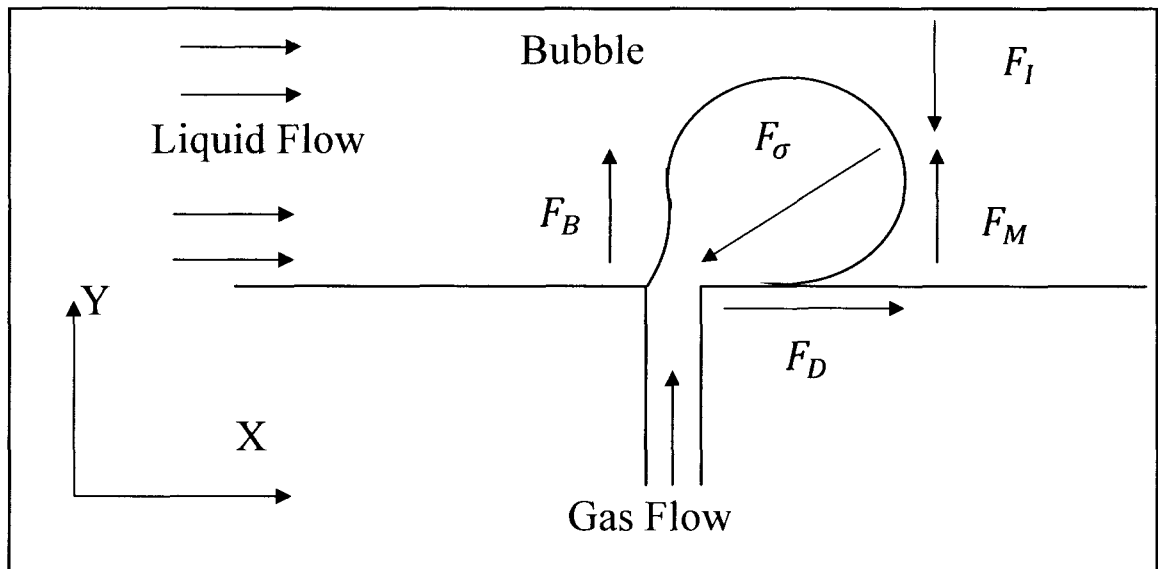


Figure 3.1 Schematic figure showing direction of different forces acting on the microbubble during its growth [44]

The general assumption behind the model development is that when the sum of the attaching forces equals the detaching forces, the bubble will get detached from the

orifice. To keep the model simple and straight forward for solving purposes, certain assumptions need to be made. They are as below:

- 1) The fluid does not undergo phase change while flowing through the device.
- 2) A non slip boundary condition is assigned to the walls in contact with the fluid.
- 3) The fluid is assumed to be incompressible.
- 4) Thermo physical properties are assumed constant.
- 5) Phenomenon such as viscous heat dissipation and flow maldistribution are considered negligible.

As stated earlier in this section, the forces acting on the microbubble during the microbubble formation are classified into either attaching or detaching forces. The dominating attaching forces that obstruct the bubble growth and its detachment are the surface tension and inertia force. While surface tension acts towards the orifice of bubble generation, inertial force acts in the negative Y-direction. The direction of surface tension force changes its angle towards both the X and Y axes as the bubble extends towards the positive X direction. The drag force is the major detaching force and it acts in the direction of the liquid flow. Since the bubble formation is inside the micro channel, the drag forces in the Y direction are considered negligible compared to the drag force in the X direction. The momentum force and the buoyancy force are the two other detaching forces. They act in the positive Y direction. Even though the momentum force is the dominating force when compared to the buoyancy force, the latter is also considered in this study. Each of the forces considered in this study is explained below, and the microbubble diameter prediction model is developed by balancing those equations. Even though all the forces are considered in developing the model, it is to be noted that all of

them may not have the same effect in determining the bubble diameter and detachment criteria in micro scale. The model is experimentally validated in Chapter 6, and the effect of each force in micro channel is studied there. The forces that are negligible will be determined experimentally in Section 6.1. The attaching forces are considered first, followed by the detaching forces. The nomenclature corresponding to the equations used in this chapter is represented in APPENDIX A.

**Surface tension force:**

$$F_{\sigma} = \sigma \pi D_o, \quad (3.1)$$

where  $D_o$  is the diameter of the orifice and  $\sigma$  is the surface tension.

**Inertia force:**

$$F_I = \frac{d}{dt} \left( M' \frac{ds}{dt} \right), \quad (3.2)$$

where  $M'$  is given as [52]

$$M' = \frac{11}{16} \rho_g V_B, \quad (3.3)$$

where  $\frac{ds}{dt}$  is the bubble velocity at the center of the bubble and  $V_B$  is the bubble volume.

**Drag Force:**

$$F_D = C_D \frac{1}{2} \rho_l U_l^2 A_{eff}, \quad (3.4)$$

where  $U_l$  is the liquid velocity,  $A_{eff}$  is the effective area and  $C_D$  is given as [53],

$$C_D \approx \frac{24}{R_e} + \frac{6}{1 + \sqrt{R_e}} + 0.4 : 0 \leq R_e \leq 2e5. \quad (3.5)$$

When the bubble starts expanding, the drag coefficient acting on the bubble and the effective liquid velocity around the region of the bubble will start changing. In order



to compensate for this effect, a modified drag coefficient and a new effective velocity is introduced in the current model. The modified drag coefficient and effective velocity is given by Equations 3.6 and 3.7. The Reynolds number of the base liquid flow around the bubble changes as the bubble expands. A new bubble Reynolds number is derived by accounting this issue and is given by Equation 3.8 [27].

$$C_{MD} = \frac{C_D}{1 - \frac{2R}{D_h}} \quad (3.6)$$

$$U_l^* = \frac{U_l A_l}{A_l - \pi R^2} \quad (3.7)$$

$$R_{eb} = \frac{\rho_l \left( U_l^* - \frac{ds}{dt} \right)^2 D_b}{\mu_l}, \quad (3.8)$$

where  $R_{eb}$  is bubble Reynolds number,  $R$  and  $D_b$  is radius and diameter of the bubble.

**Momentum force:**

$$F_m = \frac{\rho_g 4Q_g^2}{\pi D_o^2}, \quad (3.9)$$

where  $Q_g$  is the gas flow rate.

**Buoyancy Force:**

$$F_B = \frac{4}{3} \pi R^3 g (\rho_l - \rho_g) \quad (3.10)$$

The microbubble detachment condition is derived by balancing all the forces together with respect to the direction in which it is acting. When the resultant of the detaching forces equals the attaching forces, the microbubble is assumed to detach from the orifice. The detachment condition is obtained by applying the trigonometric relation

to the different forces acting on the microbubble according to their direction. In the trigonometric relation, the resultant of the momentum force, buoyancy force, and the inertia force forms the altitude of the right triangle. The drag force makes the base of the right triangle, and the surface tension is considered as the hypotenuse as shown in Figure 3.1, and is represented by Equation 3.11. The radius of the microbubble at the moment of detachment is obtained by solving the Equation 3.12 for R using MATLAB<sup>®</sup> software.

**Force balance equation:**

$$F_\sigma = \sqrt{(F_M + F_B - F_I)^2 + F_D^2} \quad (3.11)$$

$$\pi D_o \sigma = \left\{ \left( \frac{\rho_g 4Q_g^2}{\pi D_o^2} + \frac{4}{3} \pi R^3 g (\rho_l - \rho_g) - \frac{d}{dt} \left( M \frac{ds}{dt} \right) \right)^2 \right\}^{\frac{1}{2}} + \left( \frac{1}{2} \rho_l \frac{C_D}{1 - \frac{2R}{D_h}} \left( \frac{U_l A_l}{A_l - \pi R^2} \right)^2 \right)^2 \pi R^2 \quad (3.12)$$

Since the constant gas flow condition is assumed in the model, the rate of change in the volume of the microbubble over time can be used to obtain the change in radius of the microbubble over time and is represented using Equations 3.13 and 3.14.

$$\frac{d}{dt} \frac{4}{3} \pi R^3 = Q_g \quad (3.13)$$

$$\dot{R} = \frac{Q_g}{4\pi R^2} \quad (3.14)$$

### 3.2 Modified Model for Flow Focusing

The flow focusing technique is introduced into the base micro channel, which produces smaller microbubble at smaller magnitudes of Reynolds numbers compared to

the model without flow focusing. As can be observed from Figure 3.2, a semi-circle structure is placed in the base liquid channel in front of the orifice of bubble generation. Due to the presence of flow focusing inside the micro channel, the velocity of the liquid flow in the base channel around the orifice increases, and the pressure in the region decreases. The increase in liquid velocity around the orifice will increase the drag force acting on the bubble, and the decrease in absolute pressure in front of the orifice will help the bubble to grow faster. Figure 3.2 represents the flow focusing technique inside a cross-flow bubble generator.

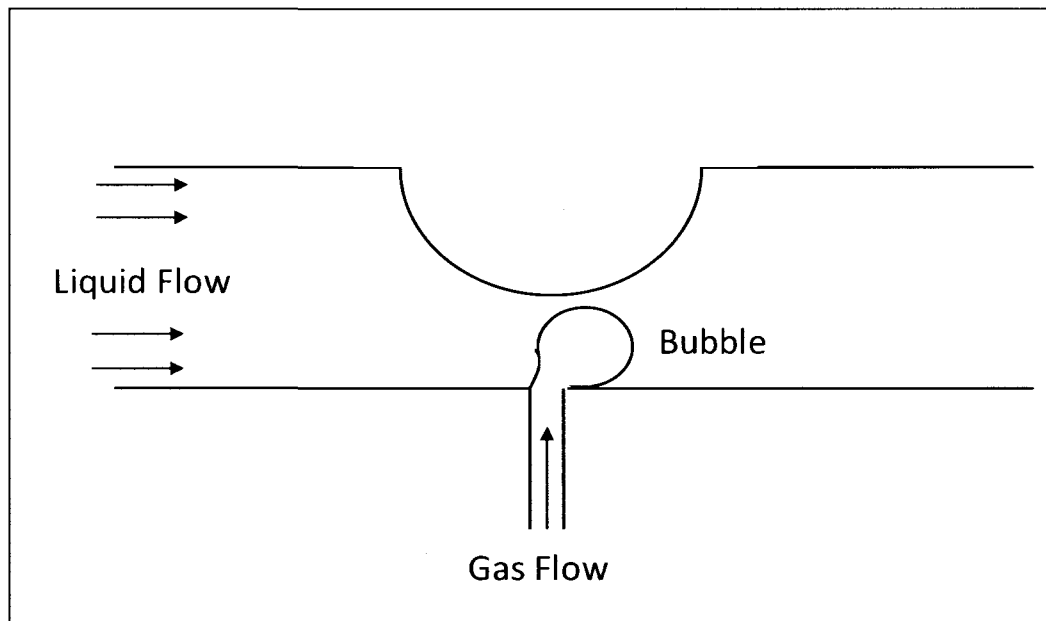


Figure 3.2 Schematic figure showing microbubble generation in a micro channel with flow focusing

The mathematical model developed for predicting the bubble diameter in the Section 3.1 can be modified for predicting the diameter of the bubbles generated in a flow focusing device by substituting modified liquid velocity  $U_{tm}$  in the place of initial liquid

velocity  $U_l$  in Equation 3.12. Equations 3.15 and 3.16 represents the modified model.

$$U_{lm} = \frac{U_l A_l}{A_{lm}} \quad (3.15)$$

$$\pi D_o \sigma = \left\{ \left( \frac{\rho_g 4Q_g^2}{\pi D_o^2} + \frac{4}{3} \pi R^3 g(\rho_l - \rho_g) - \frac{d}{dt} \left( M' \frac{ds}{dt} \right) \right)^2 \right\}^{\frac{1}{2}} + \left\{ \frac{1}{2} \rho_l \frac{C_D}{1 - \frac{2R}{D_h}} \left( \frac{U_l A_l}{A_{lm} - \pi R^2} \right)^2 \pi R^2 \right\} \quad (3.16)$$

Both the models are numerically solved for the radius of the microbubble using a MATLAB<sup>®</sup> program developed for this application. The application of this model is limited only for the bubble generation where the size of the bubbles formed in the micro channel is less than the size of the liquid channels. When the size of the bubble is more than the size of the liquid channel in which it is formed, a slip occurs between the gas and the solid interface, and the above developed model will not be sufficient for predicting the bubble diameter.

### 3.3 Feasibility Study for Flow Focusing

T. J John and H. Hegab developed a numerical mode to study the feasibility of using the flow focusing structures in the cross-flow microbubble generator with the help of a commercially available CFD package COMSOL 3.5 [45]. COMSOL uses the finite element model to solve the governing equations. The numerical model developed was used to study the bubble diameter produced in a 100 $\mu$ m base channel with a 20 $\mu$ m secondary channel, with and without flow focusing. The effect of the different shapes of flow focusing structures on the bubble generation was also studied to find the optimal

shape for the flow focusing structure. Figure 3.3 shows all the models that has been used for the feasibility study of introducing flow focusing in cross-flow bubble/droplet generators.

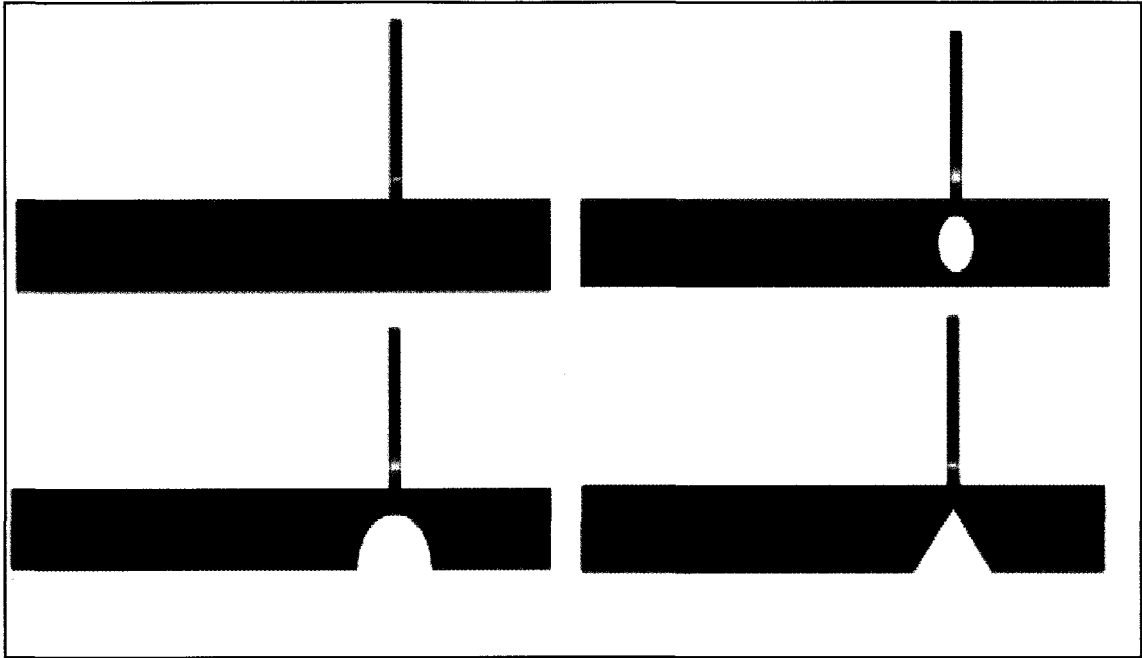


Figure 3.3 Different numerical models generated using COMSOL for feasibility study (base channel  $100\mu\text{m}$ , secondary channel  $20\mu\text{m}$ , flow focusing structures  $50\mu\text{m}$  and  $100\mu\text{m}$ , flow direction -X)

The model uses the finite element method to solve the three governing equations: momentum transport equation, continuity equation, and level set equation (Equations 3.17, 3.18, and 3.19).

$$\rho \frac{\partial u}{\partial t} + \rho(u \cdot \nabla)u = \nabla \cdot \left[ -pI + \nabla(\nabla u + (\nabla u)^T) \right] + F_{st} \quad (3.17)$$

$$\nabla \cdot u = 0 \quad (3.18)$$

$$\frac{\partial \phi}{\partial t} + u \cdot \nabla \phi = \gamma \nabla \cdot \left( -\phi(1-\phi) \frac{\nabla \phi}{|\nabla \phi|} + \varepsilon \nabla \phi \right) \quad (3.19)$$

The level set function is a numerical method used to track the change in the interfaces between water and air [45]. Level set function has the advantage of tracking the change in shape or interface with a smooth function very accurately, but has the disadvantage of poor conservation of mass [45]. COMSOL<sup>®</sup> uses a modified version of level set function which has better conservation of mass properties [45]. The density and viscosity of both liquid and air are calculated using Equations 3.20 and 3.21.

$$\rho = \rho_l + (\rho_g - \rho_l)\phi \quad (3.20)$$

$$\eta = \eta_l + (\eta_g - \eta_l)\phi \quad (3.21)$$

Certain boundary conditions are used to attain the solution of the models. Laminar flow condition with known volume flow rate is applied at the inlet boundary of the liquid channel [45]. The outlet boundary of the liquid channel is kept at pressure zero. Since the model is concerned only with the pressure drop across the channel, this assumption holds good in this case [45]. A wetted boundary condition is used for the solid boundaries. The interface between the air and the solid has a slip length, which is kept as minimal as possible, but still allows the interface between the air and the solid to move [45]. At places away from the gas solid interface, the liquid velocity at the walls is kept almost zero by adjusting the slip length [45]. The wetted boundary condition assumed on the walls is based upon a study done by Graaf et al. in 2005 on droplet formation in a 100 $\mu\text{m}$  liquid channel [30]. The gas flow in square channels of dimensions less than 65 $\mu\text{m}$  will be always slip in nature. The contact angle between the air and solid interface for the initial models are set as 135 $^\circ$ , and the effect of change in contact angle is studied later in this thesis [45]. The contact angle between the air and solid boundary is measured experimentally to validate this assumption; it was found to be around 138 $^\circ$  [45]. The

initial interface of the air and the liquid is assumed to be in the gas channel towards the orifice [45]. The diameter of the bubble formed is calculated by equating the volume of the bubble formed to a spherical bubble [45].

## CHAPTER 4

### FABRICATION

As mentioned in the introduction, the current bubble/droplet generation devices use micro channels made of materials such as silicon and PDMS [11]. The major limitation of this technique is the incapability of aligning the orifice at the center of one of the base channel side walls due to the fabrication limitation. Kim and Roy Shubert tried to come up with a new fabrication technique, which involves the fabrication of two micro channels perpendicular to each other, and connecting them using a very small micro channel of hydraulic diameter less than  $10\mu\text{m}$  etched using the ion milling technique [47]. Even though the work was able to produce microbubbles, it failed to achieve the initial objective of the project, which was to consistently produce microbubbles of size less than  $20\mu\text{m}$ . The major drawback of the model was the use of an orifice fabrication technique, which aligns the orifice towards the top corner of the micro channel. In order to improve the model and achieve the target of producing microbubbles of diameter less than  $10\mu\text{m}$  consistently, a new method of fabricating bubble/droplet generators has been developed for this study. The base channel for the new device is made of a silicon wafer and a fused silica tube with inner diameter much smaller than the hydraulic diameter of the base micro channel used as the secondary channel. The process step involved in the fabrication of microbubble/droplet generator is given in Figure 4.1



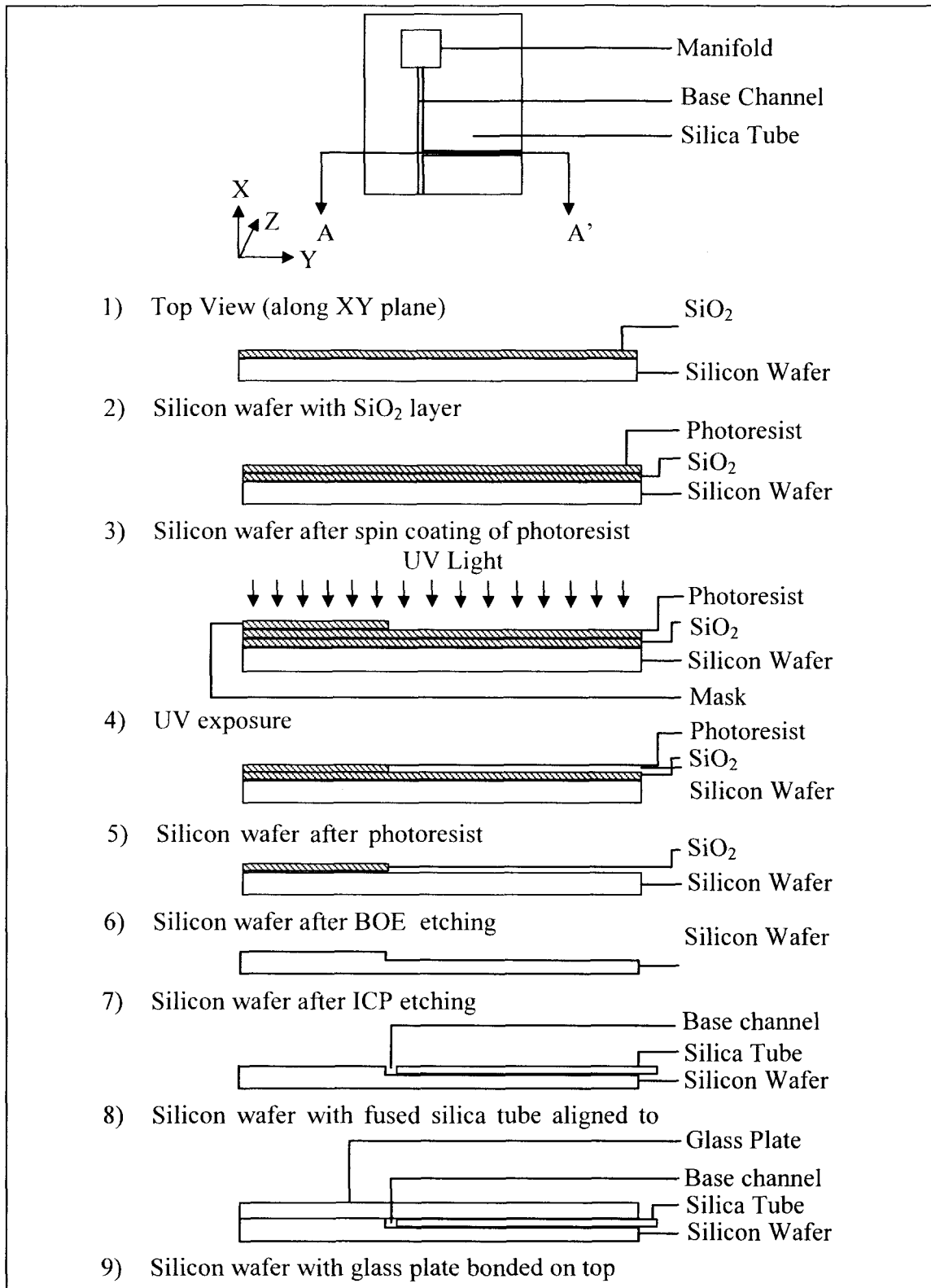


Figure 4.1 Process flow for manufacturing microbubble/droplet generator

The depth of the base channel in this technique is limited to the outer diameter of the fused silica tube, which is readily available in the market with a minimum outer diameter of 90 $\mu\text{m}$  and minimum inner diameter of 2 $\mu\text{m}$ . The major steps involved in the fabrication of a new microbubble/droplet generator includes the fabrication of micro channels, fused silica tube alignment inside the micro channel, anodic bonding, and fixing up the tubes for enabling the inflow and outflow of the fluids. Micro channels are fabricated on 4inch silicon wafers with <100> orientation using standard photolithography and dry etching techniques. Fused silica tube alignment, which is a major step in the fabrication of the microbubble/droplet generator, is achieved using a custom made microscope setup dedicated for alignment purpose. Using the microscope setup, the fused silica tube can be aligned into the micro channel made for it, while the wafer is on the anodic bonding setup. This helps to avoid the misalignment of the silica tube inside the micro channel while moving the device from one setup to the next. The anodic bonding between the silicon wafer and glass piece is achieved using the regular bonding technique, which uses high voltage and temperature for the bonding purpose. Setting up the inlet and outlet tube connections for the microbubble/droplet generator is attained by machining holes on the glass plate before bonding and fixing the tubes using UV curable glue. Each major step involved in the manufacturing of the microbubble/droplet generator is explained one-by-one in the Section 4.1.

#### **4.1 Microchannel Fabrication**

Micro fabrication of any device on a silicon wafer involves certain steps, such as the design of the mask pattern, fabrication of the mask, transfer of the mask pattern onto the photoresist material coated on the silicon wafer, transfer of the pattern on the

photoresist to the hard mask, and finally transfer of the desired pattern on the silicon wafer using etching techniques. Each of these steps includes various standard protocols that have to be very carefully followed to obtain a perfect transfer of the desired pattern into a structure on the silicon wafer.

#### **4.1.1 Mask design**

As stated earlier, the first step involved in the micro manufacturing of micro channels is the design of the mask using CAD (computer aided design) software such as AutoCAD® or Solid Edge®. The design of the mask for the microbubble/droplet generator starts with the determination of the dimensions of micro channels (width and length), depending on variable parameters such as Reynolds number of liquid flow, outer diameter of the secondary fused silica tube, etc. Analytical models developed to study the microbubble/droplet formation inside the micro channel are used to predict the suitable design dimensions for the microbubble/droplet generators. Certain fabrication constrain, like the minimum resolution of the mask printer, are also taken into consideration while designing the mask for the microbubble/droplet generator. During the initial stages of the study, Solid Edge® CAD software was used to design the mask used for the fabrication process of the microbubble/droplet generator. The mask drawn using the Solid Edge® was converted into PDF format at a resolution of 4000dpi (dots per inch) with a scaling ratio of 1:1 to ensure the proper quality and right dimensions of the mask pattern. During the initial feasibility study of the project, six devices were designed on a single mask designed for a 4inch silicon wafer. But during the final stages of the microbubble/droplet generators manufacturing, up to 12 devices were accommodated on a single mask of the same size to attain maximum yield from a 4inch silicon wafer. Ends of the base micro

channels were terminated using manifolds of a square shape with the dimensions of 5mm. These manifolds ensured the availability of space for fixing the external tubes connected to the device.

Since the minimum dimensions of the base micro channels used in the fabrication of the microbubble/droplet generator were  $90\mu\text{m}$  (due to the minimum outer diameter of the fused silica tube available in the market), the expensive masks manufacturing techniques with high resolution were not needed for the study. So, during the initial stages of the study, simple emulsion masks were printed on photographic films using a Linotronic 330 Linotype printer which has a minimum resolution of  $25\mu\text{m}$ . The film containing the mask pattern was developed using a regular film developing machine. For the final device manufacturing, chrome masks were made with high resolution to ensure high quality of repeatability of the channel dimensions each time the device was made. Final layouts of the mask for both cross-flow and co-flow device are given in Figure 4.2.

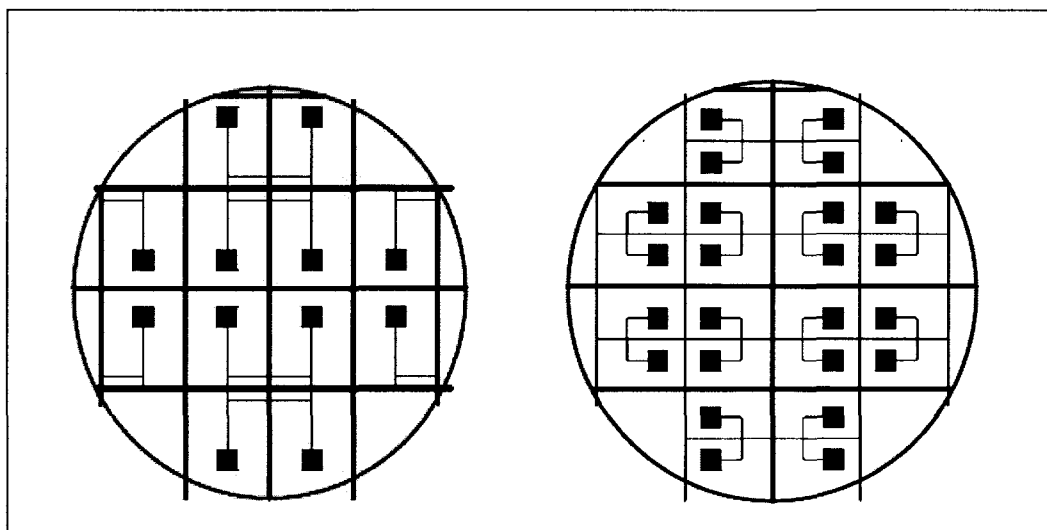


Figure 4.2 Mask pattern for cross-flow and co-flow devices

The chrome mask was made on a glass plate; initially the glass plate was coated completely with chrome material; the pattern generator machine generated the pattern on the chrome layer using precise laser heads. The chrome masks have a very high precision to ensure the actual dimensions of the layout design when transferred to the final device. Figure 4.3 gives the picture of a chrome mask containing cross-flow bubble generating devices.

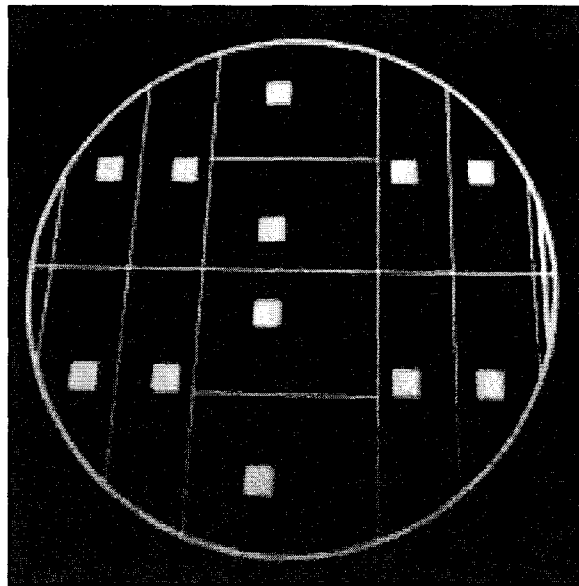


Figure 4.3 Chrome mask for generation cross-flow devices

#### 4.1.2 Photolithography

Photolithography is the fabrication step used to transfer the pattern present on the mask onto the hard mask present on the silicon wafer. The process is carried out with the aid of the photoresist material, UV light, and the developing solution. The hard mask is the protective layer on the top of the silicon wafer, which prevents the etching of the silicon from the undesired areas of the wafer. The first process involved in photolithography is the wafer preparation, which involves a series of standard protocol

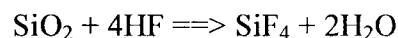
procedures to make sure that the silicon wafer surface is completely clean from any kind of contaminations. The silicon wafer is initially rinsed using isopropyl alcohol, acetone, and de ionized water. The wafer is then air dried and baked at 250°C for 30 minutes to ensure that the wafer surface is completely free from moisture. The wafer is then allowed to cool to ambient temperature and is then ready to be used for the lithography steps.

The cleaned silicon wafer is placed in the spin coating machine which is used to coat the silicon wafer with a uniform thickness of photoresist material. The thickness of the photoresist coating can be determined by the rotation speed of the spin coater and the acceleration at which the spin coater reaches its maximum rotational speed. A uniform photoresist thickness of around 2.5 $\mu$ m is obtained by setting the maximum rotational speed up to 3500rpm for one minute. The cleaned wafer is loaded on to the chuck of the spin coater with the help of vacuum pressure, and a layer of primer material is coated on it at a maximum speed of 1500rpm. HDMS is used as the primer material. It helps to provide a better adhesion of the photoresist material on to the wafer. The wafer is then coated with photoresist material SHIPLEY 1813, which is a positive photoresist. The silicon wafer coated with the photoresist material is soft baked at 115°C for 90 seconds to remove the solvents from the photoresist material. The mask is aligned on the silicon wafer using the alignment markings made on the mask during its design phase. The silicon wafer, along with the aligned mask on it, is moved to the UV station where it is exposed to the UV light at 100% intensity for about 65 seconds. Since the silicon wafer is coated with a positive photoresist material, the portions which are exposed to the UV light will become soluble in the developing solution. The wafer is then quickly moved to the developing station and is developed using MF 319 developer solution. The

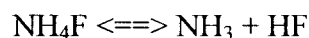
development procedure needs a lot of expertise to get a perfect pattern transfer onto the photoresist material. The patterns which are being transferred to the photoresist material are verified under an optical microscope. Next is the hard bake step. The wafer with the final pattern on the photoresist material is baked at 115°C for 90 seconds to ensure the chemical and physical stability of the photoresist layer.

#### **4.1.3 Buffered oxide etching (BOE)**

The silicon wafer which is used for the micro manufacturing in this project contains a silicon oxide layer of 2.5µm thickness. This oxide layer acts as a hard mask on the silicon substrate, which protects the silicon from being etched away from the undesired regions. Once the mask pattern is transferred to the soft mask (photoresist mask), the next step is the transfer of the pattern onto the oxide layer. This is obtained by buffered oxide etching (BOE) process. The hard-baked photoresist material on the silicon wafer acts as the mask for the oxide etching. Once the BOE etching is done, the mask pattern is permanently transferred to the oxide layer and will act as hard mask for the silicon etching. A 10:1 BOE solution containing HF, NH<sub>4</sub>F and H<sub>2</sub>O is used as the BOE etchant. The chemical reaction involved in the BOE etching is given below.



NH<sub>4</sub>F is used to maintain the concentration of the HF in the solution.



#### **4.1.4 Inductively coupled plasma etching (ICP)**

Inductively coupled plasma (ICP) etching is a dry etching technique that is used to get highly anisotropic etching of the silicon wafer. Plasma is created with the help of RF power, which is being supplied to a coil around the apparatus. The plasma reacts with

a portion of the silicon wafer which is being exposed, thus etching it to a desired depth. The etchings of the silicon material by dry etching is mainly due to the chemical reaction and to a lesser extent due to the ions being knocked out by the high power ions that reach the silicon surface. A detailed discussion of the chemistry behind ICP dry etching technique is out of the scope of this dissertation and hence not presented here.

#### **4.1.5 Anodic bonding**

The anodic bonding is used to bond the silicon wafer to the glass plate which acts as the top cover for the micro channels. The fused silica tube is placed in the micro channel made for it, and its tip is properly aligned to the side wall of the base channel. The glass plate which is bonded to the silicon wafer holds the fused silica tube intact inside the channel. Anodic bonding starts with the stripping of the leftover oxide layer from the silicon wafer after the ICP etching. The wafer is cleaned using isopropyl alcohol and acetone solution and is air dried to ensure a clean surface without any kind of contaminations. The glass plate, which is already machined to provide via for the inlet and outlet tube, is cleaned using a soap solution, isopropyl alcohol, acetone, de-ionized water and is air dried. Both the glass plate and silicon wafer are baked on a hot plate for 15 minutes at 250°C to remove the moisture completely. The temperature of the hot plate is allowed to ramp up to the desired temperature slowly after the glass plate is placed on it, and, similarly, the temperature is allowed to reach the ambient temperature gradually before the glass plate is moved to the anodic bonding setup. If the glass plate is placed on a hot plate which is already at high temperature or if it is removed from a hot plate which is at high temperature, there is a high probability of developing cracks on the glass plate. The silicon wafer is placed on the hot plate, and the glass plate is aligned on the wafer.



The aluminum plate of the hot plate acts as the positive electrode used for the bonding purpose. An aluminum block placed on the top of the glass plate serves two purposes. First, it exerts pressure on the glass plate, ensuring that the glass plate is in proper contact with the silicon wafer. Second, it acts as the negative electrode for the bonding purpose. Once the blocks are positioned and the alignment of the glass plate on the silicon wafer is checked, the hot plate is allowed to ramp up to a temperature of 400°C. After allowing the entire setup to saturate at the desired temperature, high voltage of around 900V is applied across the aluminum blocks. The high temperature, along with the high voltage, starts up ion movements at the glass silicon interface and gets them bonded together. Figure 4.4 gives the schematic representation of the anodic bonding setup.

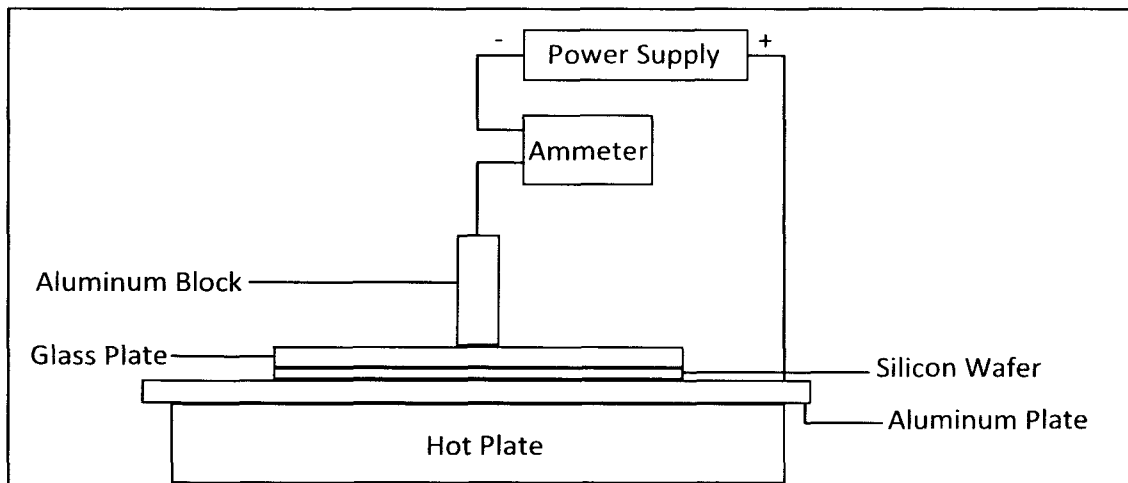


Figure 4.4 Apparatus for the anodic bonding of silicon to glass

Even though researchers had come up with theories on the mechanism of anodic bonding, the actual mechanism behind bonding procedure is still unknown to the scientific community. A microscope is used to precisely align the tip of the silica tube with the side walls of the base channel. Transporting the silicon wafer with the silica tube

aligned inside it towards the bonding setup has the risk of tube misalignment. In order to solve this issue, an anodic bonding setup which has a microscope attached to it was developed in the lab. The setup allows aligning the silica tube inside the micro channel while the wafer is placed on the hot plate. The picture of the anodic bonding setup with microscope is shown in Figure. 4.5.

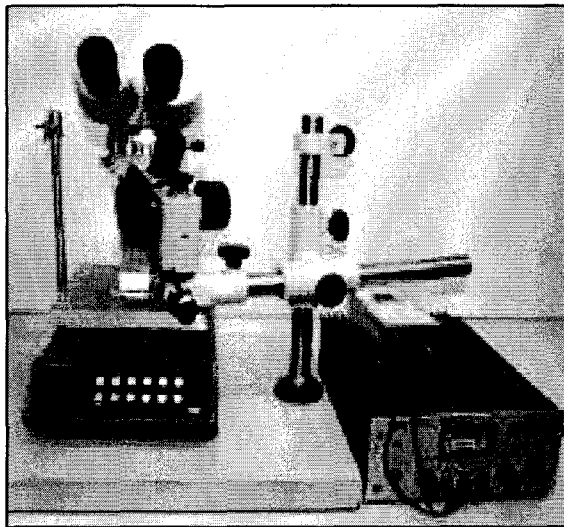
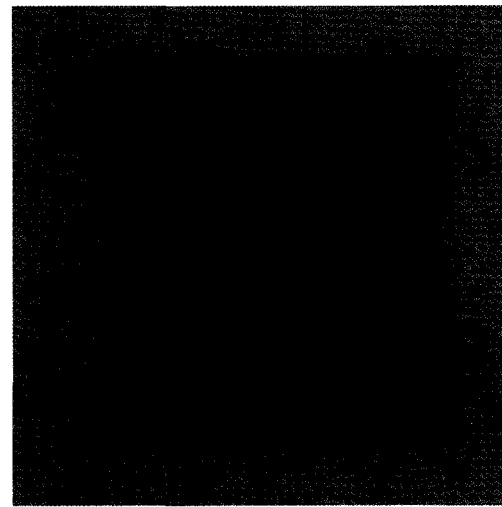
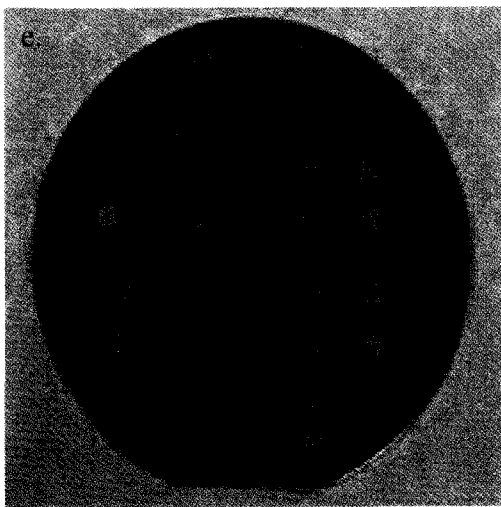
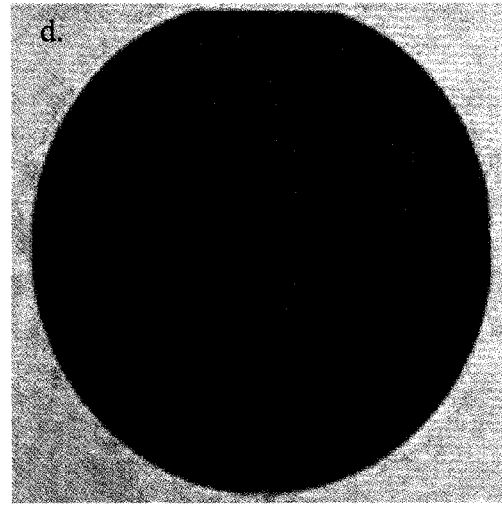
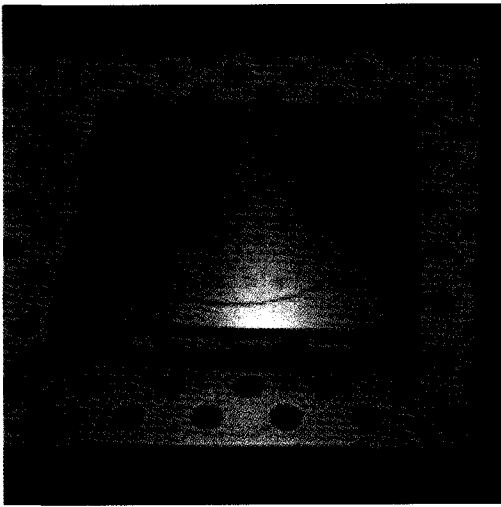
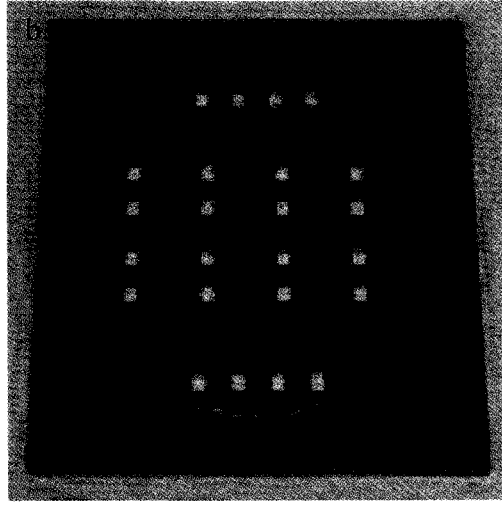
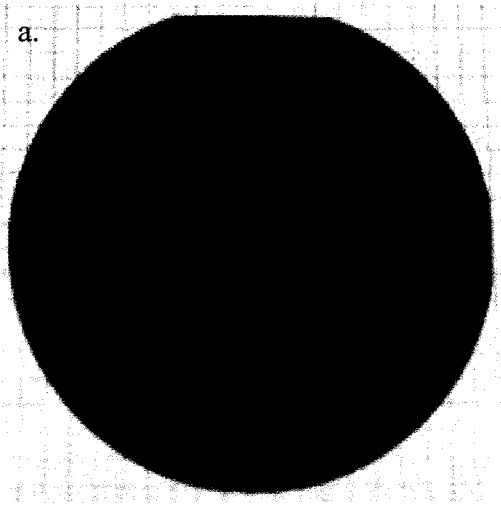


Figure 4.5 Anodic bonding setup with microscope facility

Figure 4.6 represents the pictures of various stages during the fabrication of a bubble/droplet generators, and Figure 4.7 represents both the cross-flow and co-flow bubble/droplet generators with connectors on them.



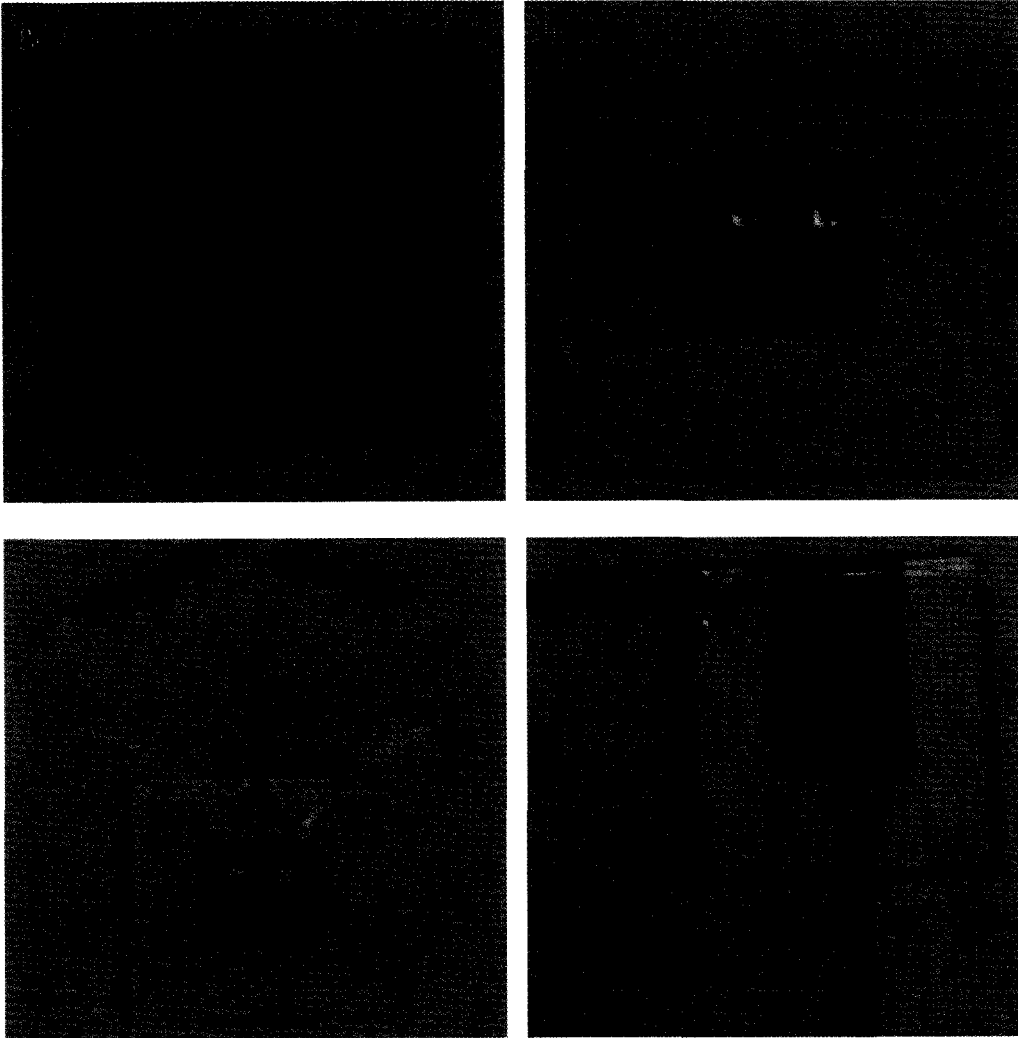


Figure 4.6 Manufacturing steps involved in making co-flow and cross-flow device

- a. Silicon wafer coated with photoresist material
- b. Chrome mask with pattern of co-flow and cross-flow devices
- c. Silicon wafer exposed to UV light with mask aligned on it
- d. Silicon wafer after photoresist development (patterns transferred on it)
- e. Silicon wafer after ICP etching
- f. Single die with a cross-flow device
- g. Single die with co-flow device
- h. Co-flow device with secondary channel aligned (after anodic bonding)
- i. Co-flow device with tubes fixed
- j. Cross-flow device with tubes fixed

#### 4.1.6 Machining and tube fixing

The glass plate is machined for via for inlets before it is bonded to the silicon wafer. The glass plate is machined using diamond coated drilling bit attached to an automated drilling machine. The drilling speed varies between 0.1mm per minute to 1mm per minute depending on the axis at which the machining takes place. Channels of 1.5mm depth are machined along the glass plate so that the inlet tube can be fixed towards the side of the device, making it suitable to be placed under a microscope. PEEK tube having an outer diameter of 1/16inch is used as an external connector from the device and is fixed to the device using UV curable glue. Figure 4.7 represents both the cross-flow and co-flow bubble/droplet generators with connectors on them.

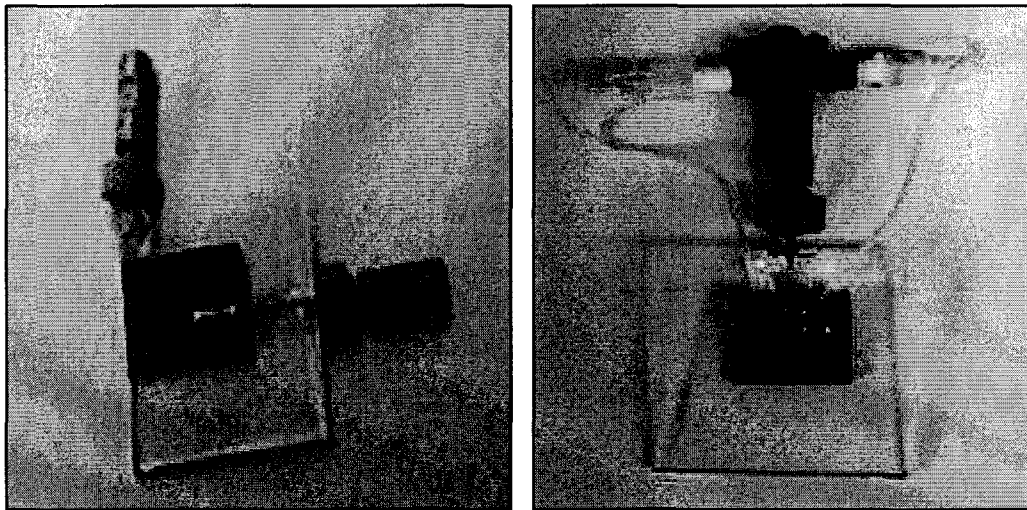


Figure 4.7 Fully finished cross-flow and co-flow device with connectors

## CHAPTER 5

### EXPERIMENTAL METHODS AND UNCERTAINTY ANALYSIS

#### 5.1 Experimental Test Bench

A complete test bench which can be used for the visualization of the microbubble/droplet formation and measuring the output parameters, like bubble/droplet diameter, flow rate of fluids, and pressure drop across micro channels was developed in the lab. In Figure 5.1, both the syringe pump and the gas tank are connected to the secondary channel; one can be selected depending on whether droplet or bubble is generated inside the base channel. A highly precise pressure valve is connected in the line of secondary fluid flow to control the secondary fluid flow rate through the channel. A similar approach was used by many researchers for bubble generation in the past [33, 37, 40, 42]. Highly precise pressure gauges are connected at both the inlet and outlet sections of the base channel to monitor the pressure drop across both the channels. A pressure gauge is connected to the outlet section of the secondary channel by means of an additional slot fabricated on the silicon wafer to study the variation of the local pressure in front of the orifice during the droplet formation inside the base channel. A high speed camera, i-speed TR which can capture up to 10000fps at a resolution of 804×600 pixels, is mounted on a microscope to capture the droplet formation in the base

channel (at a full resolution the camera can capture 2000fps at a resolution of 1280×1024 pixels). A schematic diagram of the experimental setup developed for the testing purpose is shown in Figure 5.1.

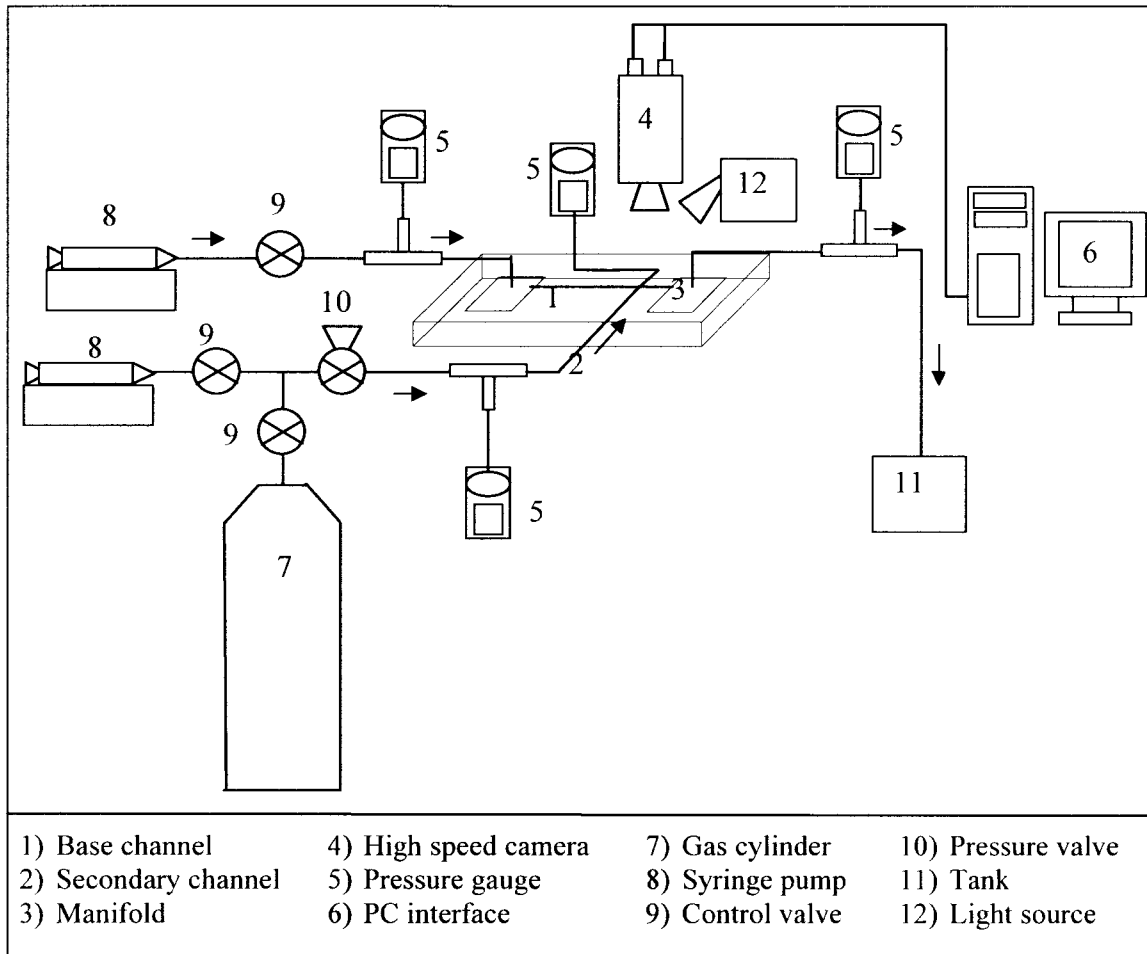


Figure 5.1 Experimental test bench used for visualizing and measuring the microbubble/droplet generation

The video being captured by the camera through the microscope is stored in a memory card integrated inside the camera and is subsequently transferred to a computer connected to the camera through the PC interface slot. The images are processed using an image processing software associated with the camera, and the formation of the

bubble/droplet and the diameter at its detachment are studied. Two light sources are used to enable the capture of the bubble/droplet images at very high speed. The first light source is connected to the microscope setup, and a 250W halogen lamp is used to illuminate it. A second light source which has two flexible fiber optical arms connected to it will guide the light to the bubble/droplet formation location very precisely. Figure 5.2 represents the high speed camera mounted on a microscope setup.

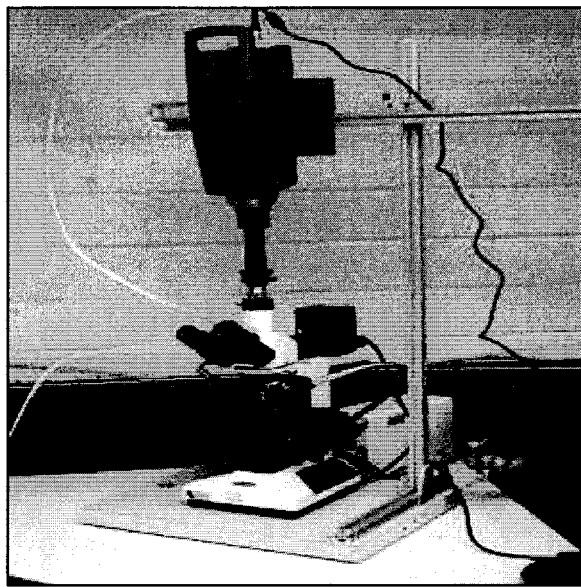


Figure 5.2 Microscope with camera and light sources mounted on it

A 150W halogen lamp provides the necessary illumination for the second light source. All the measurement gauges used in the study are calibrated before use to ensure the accuracy of the results obtained from it. The syringe pumps are calibrated by weighting the amount of liquid it pumps for a fixed amount of time on a highly precise weigh balance and back calculating the liquid volume pumped for the given period. The microscope used in the study is calibrated with image processing software. Calibration



images captured by the same microscope and camera setup using a calibration slide having very precise round structures of known dimensions. The ambient temperature of the experimental setup is measured frequently and the fluid parameters used in the experimental procedures are determined using the ambient temperature. Nitrogen, oxygen and paraffin wax oil are used as fluids in the secondary channel. De-ionized water is used as the base liquid for most of the experimental studies. For studying the effect of certain liquid based parameters, other liquids such as acetone, isopropyl alcohol, toluene and ethylene glycol are also used as the base liquids.

A major concern with the new generation bubble generators is the determination of the gas flow rate through the secondary channel. Most of the studies use syringe pumps to attain the desired gas flow rate inside the secondary channel. However, since the gas is a compressible substance, the gas flow rate obtained through the secondary channel will not be of the desired quantity [38, 39]. This flaw in the measurement can prove crucial in the characterization of the bubble generation. Since the flow rate of the gas is in milliliters per hour, there is hardly a flow meter available in the market that can measure it accurately. Hence in this project, a different approach is used to measure the gas flow rate through the secondary channel. A pressurized tank is used as the source of the gas for the secondary channel. A high precision flow valve is used to adjust the gas flow rate into the device [23, 27, 30, 32]. The pressure across the secondary channel is closely monitored and recorded. As the dimensions of the channel and the gas properties are known, the gas flow rate through the channel is obtained by recalculating the velocity of the gas flow through the channel from the measured pressure drop. The analytically calculated gas flow rate through the channel is cross examined with the experimental

results obtained for the gas flow rate by monitoring the volume of the bubbles formed inside the base channel for a specific time interval.

All the equipments used in the experimental setup of this project is calibrated before being used in the project, and measured quantities such as liquid flow rate in the base channel are cross checked with the flow rate fed into the syringe pump by collecting the liquid at the outlet of the base channel in a beaker and measuring its weight on a highly precise weigh balance. Thus, the mass flow rate of the liquid is obtained, and the volume flow rate can be analytically obtained from it.

## 5.2 Uncertainty Analysis

Even though the equipment and devices used to build the experimental setup are calibrated prior to its use in testing, still some errors can exist in the results. The errors associated with experiments can be quantified by carrying out a proper uncertainty analysis on each result that is being taken out from the experimental setups. Uncertainties associated with any system can be classified into two classes: precision error and bias error. A bias error can be related to the measurement equipment that is utilized in the experimental setup. For example, in the present study the weight of the pumped liquid through the base channel is always recorded using a precise weigh scale which can weigh up to 0.01g. Thus, any variation in the weight of the weighed liquid under 0.01g cannot be quantified and will remain as an error in the system and may reflect on the results. Such uncertainties present in the system are termed as bias error. On the other hand, a precision error occurs due to the variation in the reading of the results and can be reduced by taking repeated measurements: the more the number of measurements, the less the magnitude of precision error. The uncertainties coupled with each of the parameters

associated with the results presented in Chapter 6 are calculated individually and the methodology used for the calculations of each output parameters is presented in the Section 5.2.1 to 5.2.4.

A standard procedure to calculate uncertainty related to any function which depends on one or more variable can be calculated as shown below. Let  $P$  be a function which depends on variables  $y_1, y_2, y_3, \dots, y_n$ .

$$P = f(y_1, y_2, y_3, \dots, y_n). \quad (5.1)$$

The uncertainty associated with function  $P$  is given by  $X_p$  and can be calculated as Equation 5.2.

$$X_p = \sqrt{\left(\frac{\partial P}{\partial y_1} \times X_{y_1}\right)^2 + \left(\frac{\partial P}{\partial y_2} \times X_{y_2}\right)^2 + \dots + \left(\frac{\partial P}{\partial y_n} \times X_{y_n}\right)^2} \quad (5.2)$$

A complete analysis of the equations used for the calculation of uncertainties associated with each output parameters is presented in Section 5.2.1 to 5.2.4.

### 5.2.1 Uncertainty in bubble diameter

The most important output parameter used in this study is the bubble/droplet diameter. The diameter of the bubble/droplet is measured using the software (i-speed) associated with the camera which is used to capture the bubble/droplet generation. The software along with the microscope is calibrated before use, and the measurement is made based on the number of pixels associated with the image of each bubble/droplet. So the maximum error that can occur during the measurement of the bubble/droplet diameter is one pixel to each side of the bubble/droplet diameter. From the calibration data it was found that each pixel associated with the image is equal to  $1.10167\mu\text{m}$ , and thus the maximum uncertainty associated with the bubble diameter is  $2.0234\mu\text{m}$ . Repeated

measurements will be made on ten consecutive bubble/droplets to get rid of the precision error related to the diameter calculation.

### 5.2.2 Uncertainty in Reynolds number

Reynolds number of liquid flow through the base channel is another major input parameter used to study the variation in the bubble characteristics for different liquid flow rates, different liquids, different base channel hydraulic diameter etc. The Reynolds number of liquid flow through the base channel is represented by Equation 5.3.

$$R_e = \frac{\rho V D_h}{\mu} \quad (5.3)$$

In Equation 5.3, for Reynolds numbers the uncertainty associated with density and viscosity of the liquid is avoided by constantly monitoring the ambient temperature related to the experimental setup. So, considering these two quantities to be constant, the uncertainty related to the Reynolds number is represented as  $X_{R_e}$  and is calculated using Equation 5.4.

$$X_{R_e} = \sqrt{\left(\frac{\partial R_e}{\partial v} \times X_v\right)^2 + \left(\frac{\partial R_e}{\partial D_h} \times X_{D_h}\right)^2}, \quad (5.4)$$

where  $X_v$  and  $X_{D_h}$  are uncertainties related to the velocity of the liquid and hydraulic diameter of the base channel. By simplifying Equation 5.4, the equation for calculating the uncertainty of Reynolds number can be rewritten as Equation 5.5.

$$X_{R_e} = \sqrt{\left(\frac{\rho}{\mu} \times D_h \times X_v\right)^2 + \left(\frac{\rho}{\mu} \times v \times X_{D_h}\right)^2} \quad (5.5)$$

In order to calculate the uncertainty related to the Reynolds number given by Equation 5.5, the uncertainties related to both the velocity of the liquid flow through the base channel and the uncertainty related to the hydraulic diameter of the base channel has

to be calculated. The uncertainty of the velocity is considered first, and the velocity through the liquid channel is represented by Equation 5.6.

$$v = \frac{Q}{A_c} \quad (5.6)$$

The uncertainty of the velocity can be calculated using the standard equation by treating the liquid flow rate and cross-sectional area of the base channel as the dependent variables. Equation 5.7 represents the uncertainty of the liquid velocity through the base channel where the uncertainty of the velocity is represented as  $X_v$ .

$$X_v = \sqrt{\left(\frac{\partial v}{\partial Q} \times X_Q\right)^2 + \left(\frac{\partial v}{\partial A_c} \times X_{A_c}\right)^2} \quad (5.7)$$

The equation for the uncertainty related to the liquid velocity can be modified and can be rewritten as Equation 5.8.

$$X_v = \sqrt{\left(\frac{1}{A_c} \times X_Q\right)^2 + \left(-\frac{Q}{A_c^2} \times X_{A_c}\right)^2} \quad (5.8)$$

The simplified Equation 5.8 contains two unknown terms,  $X_Q$  and  $X_{A_c}$ .  $X_Q$  is the uncertainty related to the liquid flow through the base channel. From the repeated measurements on the liquid flow through the channel calibrated by measuring the weight of the pumped liquid, each minute the maximum uncertainty related to the liquid flow rate is found to be 0.01ml/min. This maximum value of uncertainty for the liquid flow assumption is taken from the repeated measurements and is experimentally validated. The uncertainty related to the cross-sectional area of the base liquid channel can be calculated using the standard uncertainty calculation method and is represented by Equation 5.9.

$$X_{A_c} = \sqrt{\left(\frac{\partial A_c}{\partial W} \times X_W\right)^2 + \left(\frac{\partial A_c}{\partial D} \times X_D\right)^2} \quad (5.9)$$

The uncertainty equation for the cross-sectional area of the base channel is simplified and is rewritten as Equation 5.10.

$$X_{A_c} = \sqrt{(D \times X_w)^2 + (W \times X_D)^2} \quad (5.10)$$

The uncertainty in the velocity of the liquid flow through the base channel can be calculated plugging back the uncertainties in the liquid flow rate and uncertainty in the cross-sectional area of the base channel. In order to calculate the uncertainty in the Reynolds number the uncertainty associated with the hydraulic diameter also has to be calculated. The hydraulic diameter of a rectangular channel is given by the Equation 5.11.

$$D_h = \frac{4 \times A_c}{P} \quad (5.11)$$

And the uncertainty associated with hydraulic diameter can be calculated using Equation 5.12

$$X_{D_h} = \sqrt{\left(\frac{\partial D_h}{\partial A_c} \times X_{A_c}\right)^2 + \left(\frac{\partial D_h}{\partial P} \times X_P\right)^2} \quad (5.12)$$

Simplifying the above equation gives the uncertainty in the hydraulic diameter of the base channel and is represented by Equation 5.13.

$$X_{D_h} = \sqrt{\left(\frac{4}{P} \times X_{A_c}\right)^2 + \left(-\frac{4 \times A_c}{P^2} \times X_P\right)^2} \quad (5.13)$$

As can be noticed from Equation 5.13, in order to calculate the hydraulic diameter uncertainty, the uncertainty in the perimeter of the base micro channel must be calculated first. The uncertainty associated with the cross-sectional area of the base channel is calculated earlier for the calculation purpose of the uncertainty of liquid velocity. The

perimeter of the base channel is represented by Equation 5.14 where  $D$  and  $W$  represents the depth and width of the base channel.

$$P = 2 \times (W + D) \quad (5.14)$$

The uncertainty associated with the perimeter calculation in the generalized form and in a further simplified form are represented by Equations 5.15 and 5.16.

$$X_p = \sqrt{\left(\frac{\partial P}{\partial W} \times X_w\right)^2 + \left(\frac{\partial P}{\partial D} \times X_D\right)^2} \quad (5.15)$$

$$X_p = \sqrt{(2 \times X_w)^2 + (2 \times X_D)^2} \quad (5.16)$$

Plugging back the uncertainties related to the velocity and the hydraulic diameter of the base channel, the uncertainty in the Reynolds number can be calculated.

### 5.2.3 Uncertainty in void fraction

Another important term used to represent the results obtained from the experimental setup is the void fraction. Void fraction is defined as the area of the bubble/droplet divided by the area of the cross-sectional area of the base channel. In simple words, void fraction defines the area occupied by the microbubble/droplet inside the base channel. The Equation 5.17 is used for calculating the void fraction.

$$VF = \frac{\pi R^2}{A_c} \quad (5.17)$$

The uncertainty related to the void fraction is calculated in the general form as follows where  $X_{AB}$  and  $X_{AC}$  are the uncertainties related to the cross-sectional area of the base channel and cross-sectional area of the bubble/droplet. The uncertainty related to the cross-sectional area of the base channel is already calculated, and the uncertainty of the bubble/droplet cross-sectional area has to be calculated. The uncertainty related to the

void fraction is represented in both the generalized form and the simplified form using Equations 5.18 and 5.19.

$$X_{VF} = \sqrt{\left(\frac{\partial VF}{\partial A_B} \times X_{A_B}\right)^2 + \left(\frac{\partial VF}{\partial A_C} \times X_{A_C}\right)^2} \quad (5.18)$$

$$X_{VF} = \sqrt{\left(\frac{1}{\partial A_C} \times X_{A_B}\right)^2 + \left(-\frac{A_B}{A_C^2} \times X_{A_C}\right)^2} \quad (5.19)$$

The uncertainty related to the cross-sectional area of the bubble/droplet is calculated below. As the cross-sectional area of the bubble/droplet has only one variable parameter, the equation has only one form. The generalized equation is simplified in Equation 5.20.

$$X_{A_B} = \sqrt{\left(\frac{\partial A_B}{\partial D_B} \times X_{D_B}\right)^2} \quad (5.20)$$

$$X_{A_B} = \frac{\partial A_B}{\partial D_B} \times X_{D_B} \quad (5.21)$$

$$X_{A_B} = \frac{\pi \times D_B}{2} \times X_{D_B} \quad (5.22)$$

Plugging back the uncertainties in the bubble/droplet cross-sectional area and cross-sectional area of the base channel, the uncertainty in the void fraction can be calculated.

#### 5.2.4 Uncertainty in superficial velocity

Another quantity used for the representing the results obtained from the experimental setup is the superficial velocity of the bubble. It defines the velocity at which the bubble travels through the base channel. The superficial velocity of the bubble is calculated using Equation 5.23.



$$v_{SB} = \frac{Q_g}{A_B} \quad (5.23)$$

The term  $Q_g$  represents the gas flow rate. As the gas flow rate in this study is calculated back from the experimental value of the pressure drop across the secondary channel, the uncertainty associated with the gas flow rate must be calculated. Since the secondary channels are of hydraulic diameter less than  $25\mu\text{m}$  in most of the cases, the slip flow equations are used for its calculation (Equation 5.24). The flow rate of gas through a channel with slip is calculated as follows where  $\Delta P$  is the pressure drop across the secondary channel and  $\Delta L$  is the length of the secondary channel.

$$Q_g = \left( \frac{\pi r_0^4}{8\mu} \right) \times \left( -\frac{\Delta P}{\Delta L} \right) \times \left( 1 + \frac{8 \times l}{D} \right) \quad (5.24)$$

Equation 5.24 used for determining the gas flow rate the variable terms are the pressure drop and channel length. All the other quantities including the diameter of the secondary channel are held constant. The uncertainty associated with the pressure drop across the secondary channel is avoided by the differential pressure measurement technique. Two separate measurements of the pressure drop across the secondary channel of two different lengths are taken, and the difference between the two pressure drops is taken as the actual pressure drop. This method helps to avoid the uncertainties in the pressure drop across the secondary channel. As the uncertainty of pressure drop across the secondary channel is avoided, the only variable term in the measurement of gas flow rate is the channel length. The uncertainty in gas flow rate is derived and simplified and is represented using Equations 5.25 and 5.26.

$$X_{Q_g} = \sqrt{\left( \frac{\partial Q_g}{\partial L} \times X_L \right)^2} \quad (5.25)$$

$$X_{Q_g} = \left( \frac{\pi r_o^4}{8\mu} \right) \times \left( 1 + \frac{8 \times l}{D} \right) \times \left( -\frac{\Delta P}{\Delta L^2} \right) \times X_L \quad (5.26)$$

After calculating the uncertainty associated with the gas flow rate, the uncertainty in the superficial velocity of the gas bubble flow through the base channel can be calculated using Equation 5.27.

$$X_{v_g} = \sqrt{\left( \frac{1}{A_B} \times X_{Q_g} \right)^2 + \left( -\frac{Q_g}{A_B^2} \times X_{A_B} \right)^2} \quad (5.27)$$

## CHAPTER 6

### RESULTS AND DISCUSSIONS

The results obtained from the experimental work conducted during this investigation are presented in this chapter in six different sections. The Section 6.1 deals with the cross-flow bubble generators, followed by the cross-flow bubble generators with flow focusing technique in the Section 6.2. Along with the study of bubble generation mechanism in cross-flow generators, a parametric study based on both the geometry and variable properties of the both the base and secondary fluid is also included in the Sections 6.1 and 6.2. The Section 6.3 deals with the bubble generation techniques in co-flow generators, followed by flow focusing techniques in the Section 6.4. Sections 6.5 and 6.6 studies the droplet generation using both cross-flow and co-flow droplet generators and novel techniques to generate smaller and unconfined microbubbles in micro channels.

Before each of the cases is considered separately, the method used to calculate the gas flow rate through the secondary channel into the devices, which is common for all the cases, is discussed briefly in this section. As discussed in previous chapters, the current study uses fused silica tubes with an inner diameter ranging from  $2\mu\text{m}$  to  $50\mu\text{m}$  as the secondary channel of the bubble generating device. The hydraulic diameter of the secondary channels used in the devices is very small, making the gas flow rate very low.

Hence, an efficient gas flow sensor which can accurately measure the gas flow rate through the secondary channel is hard to acquire. Thus, in order to measure the gas flow rate through the secondary channel efficiently, a method based on using the experimentally measured pressure drop across the channel is developed in this study. The pressure drop across the secondary channel is measured using very precise pressure gauges. A differential pressure drop calculation scheme is used in this study to avoid the measurement flaws in the pressure drop estimation. The pressure drop across the entire loop from the gas tank to the entrance of the secondary channel is measured first without connecting the secondary channel on to the loop. The pressure drop across the loop is again measured with the secondary channel present in the loop, and the difference in the pressure drop of both the cases is taken as the pressure drop across the secondary channel. As the inner diameter of the secondary channels used in the bubble generating devices falls within the slip boundary condition limit (less than 66 $\mu\text{m}$  of nitrogen flow), equations which consider the slip flow of gas through a channel are used for calculating the gas flow rate through the secondary channel. The equation used for calculating the gas flow rate through the secondary channel is given by Equation 6.1 [53].

$$Q_g = \left( \frac{\pi r_0^4}{8\mu} \right) \times \left( -\frac{\Delta P}{\Delta L} \right) \times \left( 1 + \frac{8 \times l}{D} \right), \quad (6.1)$$

where  $L$  is the known length of the secondary channel,  $l$  is the mean free path of the gas used and  $D$  is the hydraulic diameter of the secondary channel.

The research done on bubble formation in micro channels in the past using conventional bubble/droplet generators has defined the bubble/droplet generation regions into five different regimes: bubbly, wedging, slug, annular, and dry [49]. The transition

between each regime is defined using the ratio of base fluid flow rate to secondary fluid flow rate, and is given by Equation 6.2 [49].

$$\alpha_L = \frac{Q_L}{Q_L + Q_g} \quad (6.2)$$

The transition between the bubbles to the wedging region is found experimentally to be around 0.75 [49]. In the current study of bubble generation using new generation bubble/droplet generators, most of the bubble formation falls under the bubbly region, even for very high values of pressure drop across the secondary channel due its very small hydraulic diameter.

### 6.1 Cross-flow Bubble Generators

As discussed in Chapter 3, a mathematical model was generated to predict the bubble generation in cross-flow bubble generators. The mathematical model was developed on the base of force balancing techniques in which the forces that are acting on the bubble during its formation are considered separately and are grouped together depending on their direction to obtain the final force balance equation. The model is capable of predicting both the bubble formation and bubble diameter at its detachment from the orifice. A similar approach was used in models to predict bubble formation in both cross-flow and co-flow bubble generators at the macro level [26-28]. The models developed at the macro level are based on some simplifying assumptions such as bubble formation is spherical and has limitation of being able to predict the bubble diameter correctly only when the bubble diameter is less than 2/3 of the hydraulic diameter of the base channel [27]. The model prediction deviates from the experimental value when the bubble diameter is close to the hydraulic diameter of the channel. The same trend was

observed in the model developed for the micro scale in this study. The model predicts the bubble diameter correctly when the Reynolds number of liquid flow in base channel is high, causing the bubble to detach from the orifice when it is smaller than the hydraulic diameter of the base channel. Figure 6.1 gives the comparison plot between bubble diameters predicted by the mathematical model and the experimentally obtained value of bubble diameter.

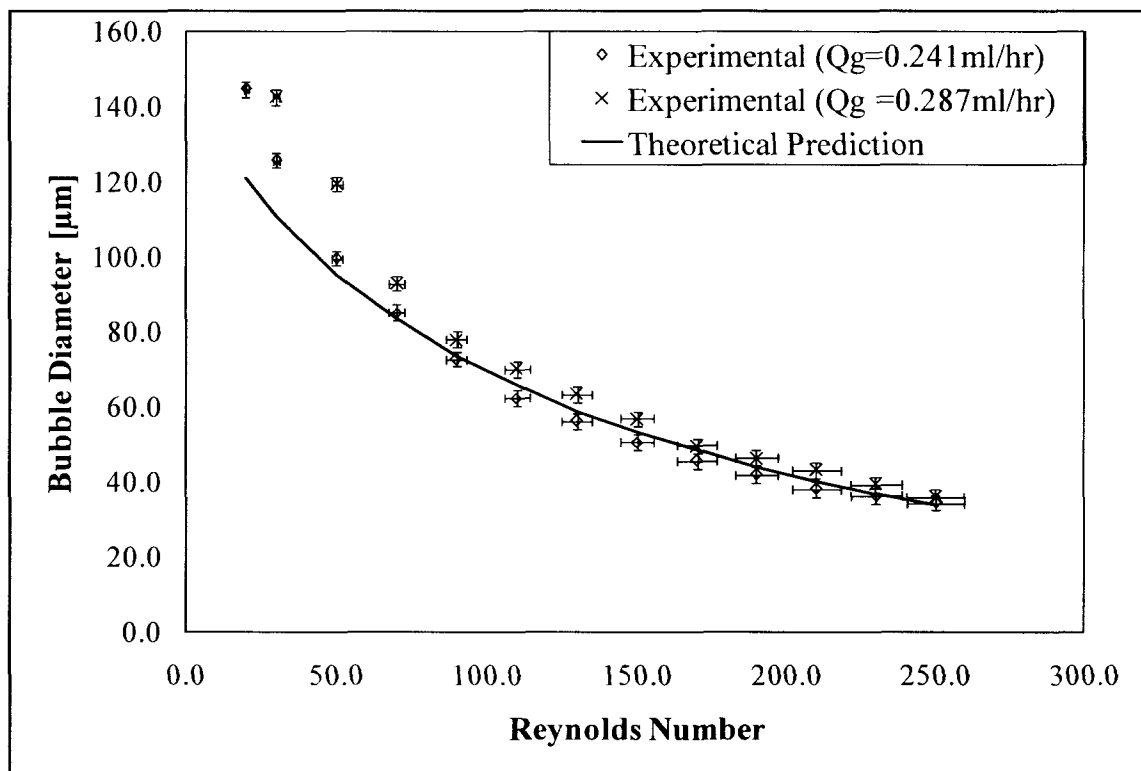


Figure 6.1 Plot compares bubble detachment diameter prediction by the mathematical model with the experimental data (base channel 150 $\mu\text{m}$ , secondary channel 10 $\mu\text{m}$ )

Figure 6.1 represents the values of bubble diameter obtained from the theoretical model and the bubble diameter obtained experimentally for two different gas flow rates over a range of Reynolds numbers of liquid flow rate in the base channel. It can be noted from Figure 6.1 that at high magnitudes of base liquid Reynolds number, the model

predicts the bubble diameter almost accurately. But when the bubble diameter is more than  $100\mu\text{m}$  (that is, when the bubble diameter is more than  $2/3$  of the hydraulic diameter of the base channel) the theoretical bubble diameter prediction tends to underpredict the experimental bubble diameter. Also, it can be noted that as the momentum of the gas flow through the secondary channel changes, the bubble diameter shift its diameter, and it is more predominant at lower values of base liquid flow rate. The deviation of the experimental bubble diameter from the theoretical prediction can be accounted for due to two reasons. The first one accounts to the limitation of the mathematical model which is a simple one dimensional model. The bubble that is being formed from the orifice will have a deformation of shape in all the three directions as it grows closer to the hydraulic diameter of the base channel. As the model is a one dimensional model, it is not capable of predicting this deformation of the bubble during its formation and ends up in the underprediction of the bubble diameter at low Reynolds number of base liquid flow. This problem was observed by some previous researchers who studied the bubble generation at the macro level [27, 28]. The second reason for the underprediction of the bubble diameter by the mathematical model at low values of base liquid Reynolds number is due to the possible merging of the bubbles. As the bubble grows larger in diameter, the velocity at which it drifts down the base channel to the outlet will decrease. This initiates the merging of the successive bubbles into the already detached bubbles. The phenomenon of bubble merging is a very quick process and is extremely difficult to observe as the hydraulic diameter of the secondary channel increases. This issue was observed and reported for the first time during the experiments conducted for this investigation. The new generation device seems to have solved this problem to a very

good extent but the problem still exist at very low Reynolds numbers of liquid flow through the base channel. Figure 6.2 represents bubbles merging into the previous bubbles after detachment.

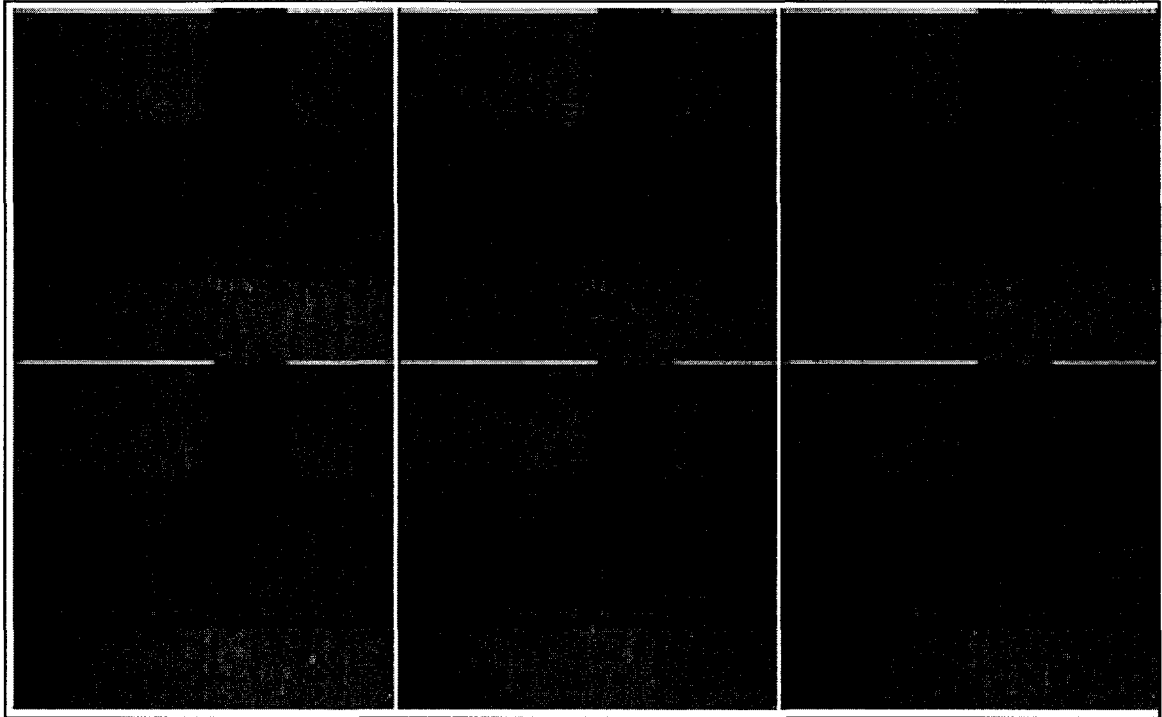


Figure 6.2 Merging of successive bubbles into the previous bubble, causing an increase in the diameter of the already detached bubble

Figure 6.2 shows the bubble merging in details. The bubble merging problem was explained briefly in Chapter 1. Another limitation that was observed in the mathematical model developed for the prediction of bubble diameter is small, the shift in the bubble diameter with the change in the gas flow rate through the secondary channel. This effect is equally contributed by both experimental uncertainties (present in both the Reynolds number of liquid flow in a base channel and bubble diameter measurement) and the failure of the model to consider the change in absolute pressure near the orifice with the



change in gas momentum. This effect is not predominant in the macro level, but has to be included in the micro scale due to the small hydraulic diameter of the base channel. Even though the mathematical model developed in the study has some small limitations, it can predict the bubble diameter almost accurately, especially when the bubble size is lesser than the  $2/3$  of the hydraulic diameter of the base channel. Figure 6.3 gives the comparison of bubble diameter obtained both mathematically and experimentally for a cross-flow bubble generator device with a base channel hydraulic diameter of 160 and a secondary channel of hydraulic diameter of  $15\mu\text{m}$ . Figure 6.4 represents the bubble formation in a cross-flow bubble generator.

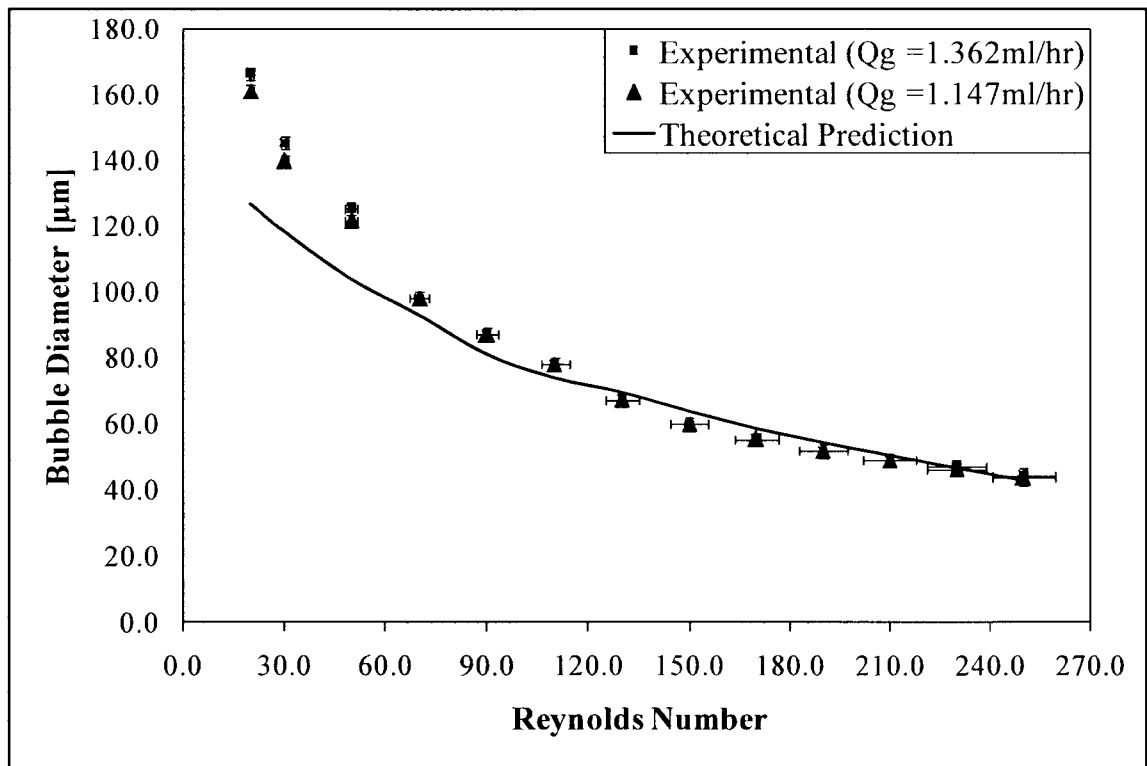


Figure 6.3 Plot compares bubble detachment diameter prediction by the mathematical model with the experimental data (base channel  $150\mu\text{m}$ , secondary channel  $15\mu\text{m}$ )

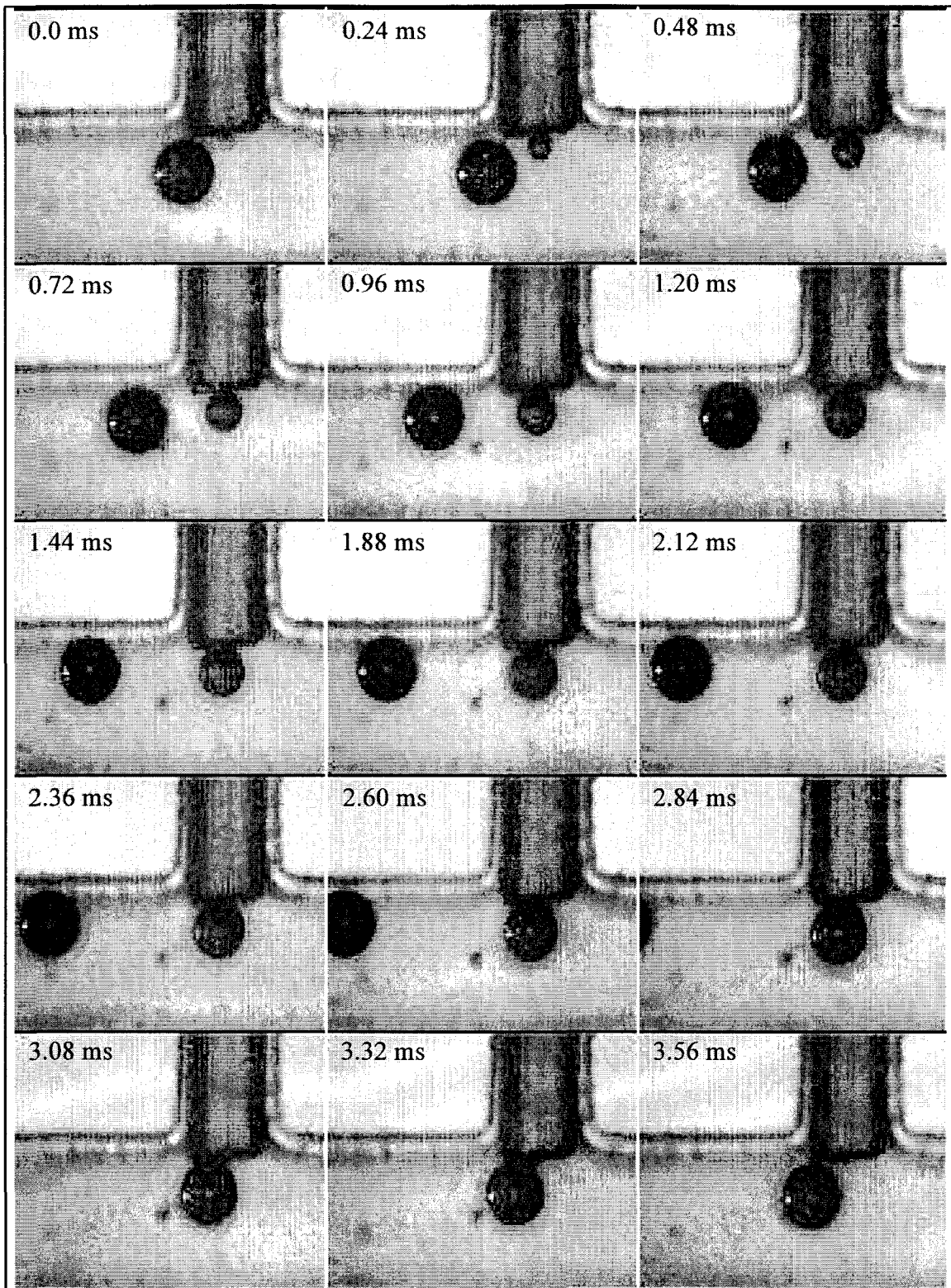


Figure 6.4 Bubble formation in a cross-flow bubble generator at various time interval taken at 7500 fps. (Base channel 270 $\mu$ m, secondary channel 10 $\mu$ m)

In order to represent the bubble detachment and transportation inside a base channel, a non-dimensionalized term void fraction is used in this study. Void fraction is defined as the cross-sectional area of the bubble divided by cross-sectional area of the base channel. In other words, void fraction determines how much fraction of the base channel cross-section is occupied by the bubble moving inside it. Void fraction provides a good non-dimensionalized parameter for the comparison of variations in bubble diameter, with variation in variable parameters like Reynolds number, geometric dimensions etc. The parametric study presented in this chapter is separated into different cases where one variable parameter is varied for each case while keeping the other parameters constant.

#### **6.1.1 Case 1: Variable parameter: Reynolds number of base liquid flow**

Figure 6.5 represents the change in the void fraction with change in the Reynolds number of liquid flow in the base channel for two different values of gas flow through the secondary channel. It can be noted in Figure 6.5 that as the Reynolds number of liquid flow in base channel increases the void fraction of bubble decreases. It can also be noted that the decrease in the void fraction is very abrupt during the initial increase in the Reynolds numbers, and the rate of change of void fraction decreases at higher values of Reynolds numbers. It has been stated earlier in this chapter that the bubble formation in this study is limited to the bubbly region ( $\alpha_L > 0.75$ ) even for very high pressure drop of gas flow across the secondary channel.

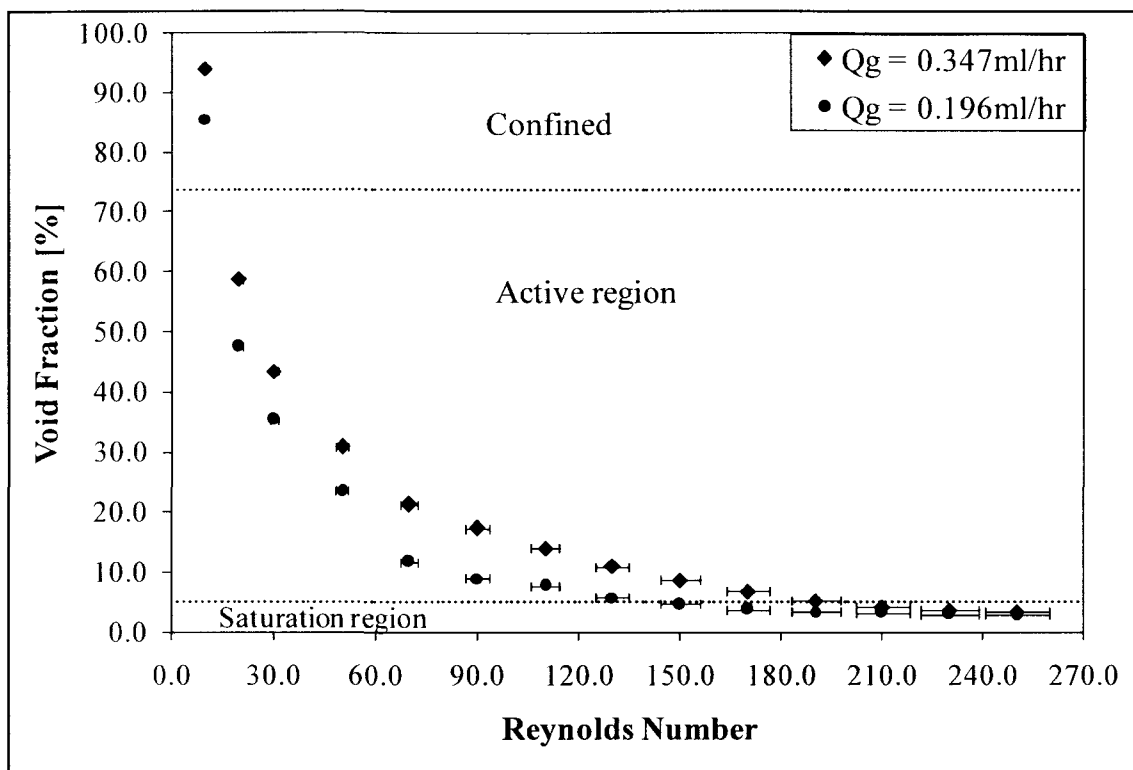


Figure 6.5 Plot gives the void fraction of bubble formation in base channel for different magnitudes of Reynolds number (base channel  $150\mu\text{m}$ , secondary channel  $10\mu\text{m}$ )

In order to have a better understanding of the bubble formation in the new generation device, the bubbly region is again divided into three regimes in this study: confined region, active region and saturation region. Confined region, as shown in Figure 6.5 is defined as the region where the void fraction corresponding to the bubbles formed in the base channel is touching more than one side wall of the base channel (that is, the diameter of the bubble is more than the shortest side of the base channel). In other words, the void fraction corresponding to the cross-sectional area of the bubble when the diameter of the bubble is equal to the shortest side of the base channel is taken as the transition point from the confined region to the active region. The active region is defined as the region where void fraction corresponding to the cross-section area of the bubble

whose diameter is lesser than the shortest side of the base channel but hasn't yet reached the saturation region. The bubble diameter changes its diameter very abruptly in the active region, and the rate of change of bubble diameter slows down as the bubble formation diameter gets close to the void fraction corresponding to the saturation region. The saturation region is defined as the region corresponding to the cross-sectional area of the bubble whose diameter does not change much with the increase in the Reynolds number of liquid flow in the base channel. That is, the rate of change of bubble diameter is very low or almost negligible (In this study the rate of change of bubble diameter is considered low when the change in bubble radius for successive values of Reynolds numbers is less than  $1\mu\text{m}$ ). The transition from the active region to the saturation region is defined using the ratio of the secondary channel to the base channel hydraulic diameter. Previous research done in the field of bubble formation in macro channels has shown that the minimum size of the uniform bubble that can be formed from an orifice depends on its hydraulic diameter. The percentage corresponding to the void fraction at which the transition from active region to saturation region occurs is defined by Equation 6.3.

$$\alpha_{sat} = \frac{D_o}{D_h} \times 100, \quad (6.3)$$

where  $D_o$  and  $D_h$  are the hydraulic diameter of orifice and base channel respectively. The value of  $\alpha_{sat}$  found from Equation 6.3 is validated using the void fractions of the bubble formed from secondary channels of different hydraulic diameter experimentally.

### 6.1.2 Case 2: Variable parameter: Gas flow rate in secondary channel

The superficial velocity of gas flow inside the cross-flow device is plotted against the superficial velocity of liquid flow in the same device in Figure 6.6.

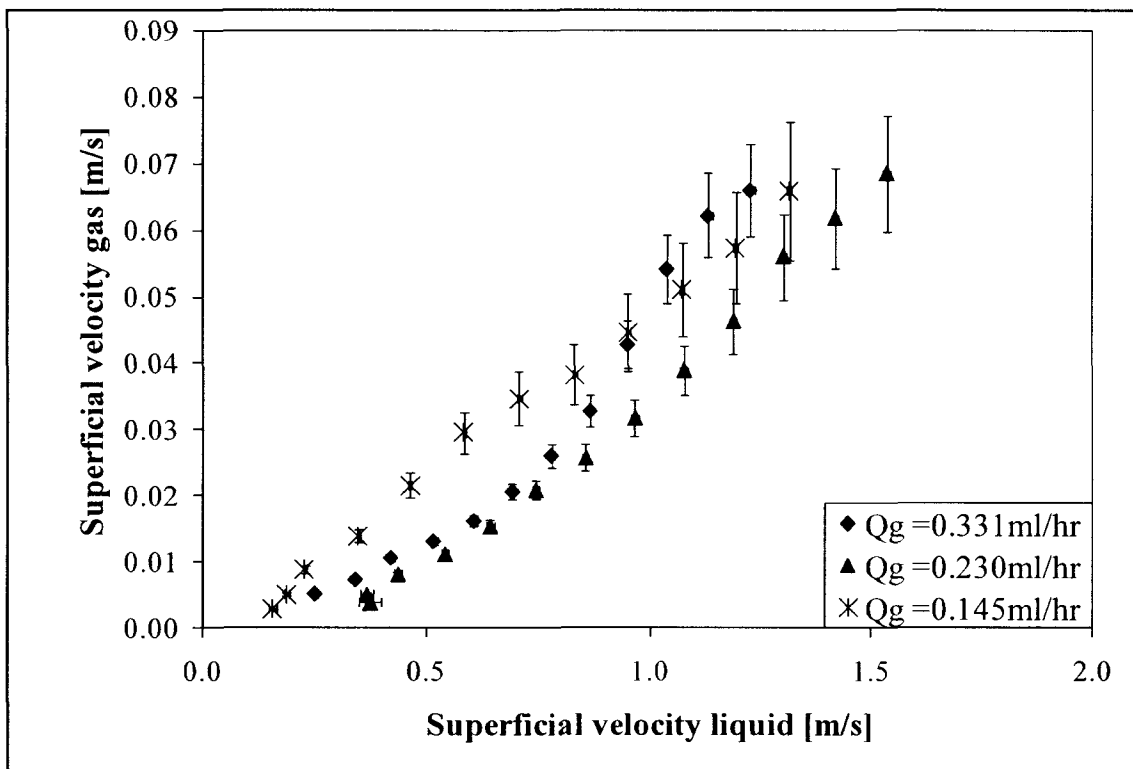


Figure 6.6 Plot gives the variation in superficial velocity of gas with respect to the change in superficial velocity of the base liquid in a cross-flow device (base channel 150 $\mu$ m, secondary channel 10 $\mu$ m)

The change in the superficial velocity of gas flow with respect to the superficial velocity of liquid flow through the base channel is plotted at three different gas flow rates in Figure 6.6. The superficial gas velocity through the channel for corresponding superficial velocities of base liquid confirms that the bubble formation is in the bubbly region, even for very high values of pressure drop across the secondary channel. The

variation in the bubble diameter with the change in the gas flow rate through the secondary channel is given in Figure 6.7.

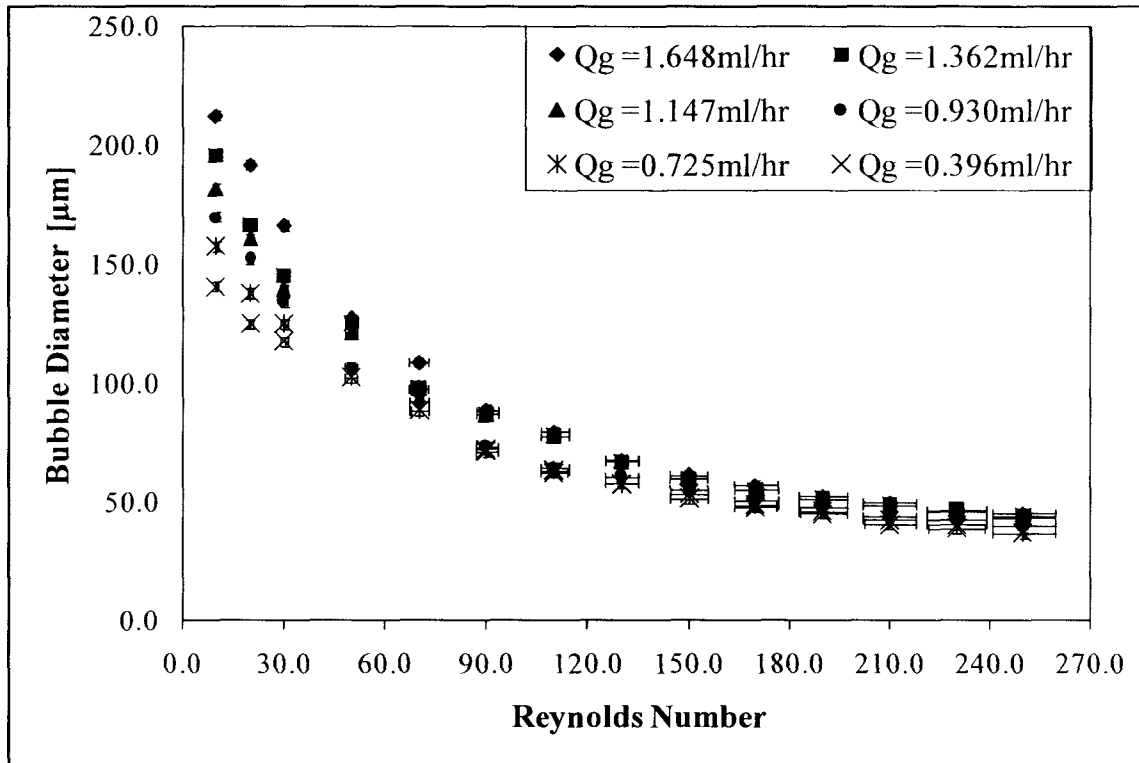


Figure 6.7 Plot gives the variation in the bubble diameter with change in base liquid Reynolds number for six different gas flow momentum (base channel  $160\mu\text{m}$ , secondary channel  $15\mu\text{m}$ )

The general trend of decrease in bubble diameter with the increase in the Reynolds number of liquid flow through the base channel is observed in Figure 6.7. As discussed in the validation section (Section 6.1) of the mathematical model, the bubble diameter increases slowly as the gas flow through the secondary channel increases. Even though the gas momentum through the secondary channel is a detaching force which helps the bubble growth, its magnitude is very small compared to the other detaching and attaching forces that act on the bubble during its formation. Another factor that is

affecting the change in the radius of the bubble formation with the change in the gas flow rate through the secondary channel is the change in the absolute pressure that is acting around the orifice inside the base channel. The variation in the bubble diameter with the change in gas flow rate is more dominant for lower values of base fluid Reynolds number. At low values of Reynolds number, the pressure drops across the base channel, and the change in the absolute pressure in front of the orifice with the change in gas flow rate is more dominant. But as the base fluid Reynolds number increases, the pressure drop across the base channel increases, and the change in absolute pressure in front of the orifice due to change gas flow rate becomes negligible. This effect can be observed for all values of hydraulic diameter of secondary channels.

### **6.1.3 Case 3: Variable parameter: Hydraulic diameter secondary channel**

The variation in the bubble diameter with the variation in hydraulic diameter of the secondary channel is studied in this section. The hydraulic diameter of the secondary channel is varied between  $2\mu\text{m}$  and  $50\mu\text{m}$ , and the variation in bubble diameter is studied in terms of void fraction and is plotted from Figure 6.8 through Figure 6.13. For each value of the secondary channel hydraulic diameter, the confined, active and saturation region are identified for comparison purposes. Figure 6.8 gives the variation in void fraction for bubbles generated from a cross-flow device having a secondary channel of hydraulic diameter  $5\mu\text{m}$ . It can be noted from Figure 6.8 that the void fraction of bubbles with a secondary channel of  $5\mu\text{m}$  diameter falls mostly in the active region. Even the bubbles formed at the highest gas flow rate and the lowest value of the base fluid Reynolds number fall in the active region.



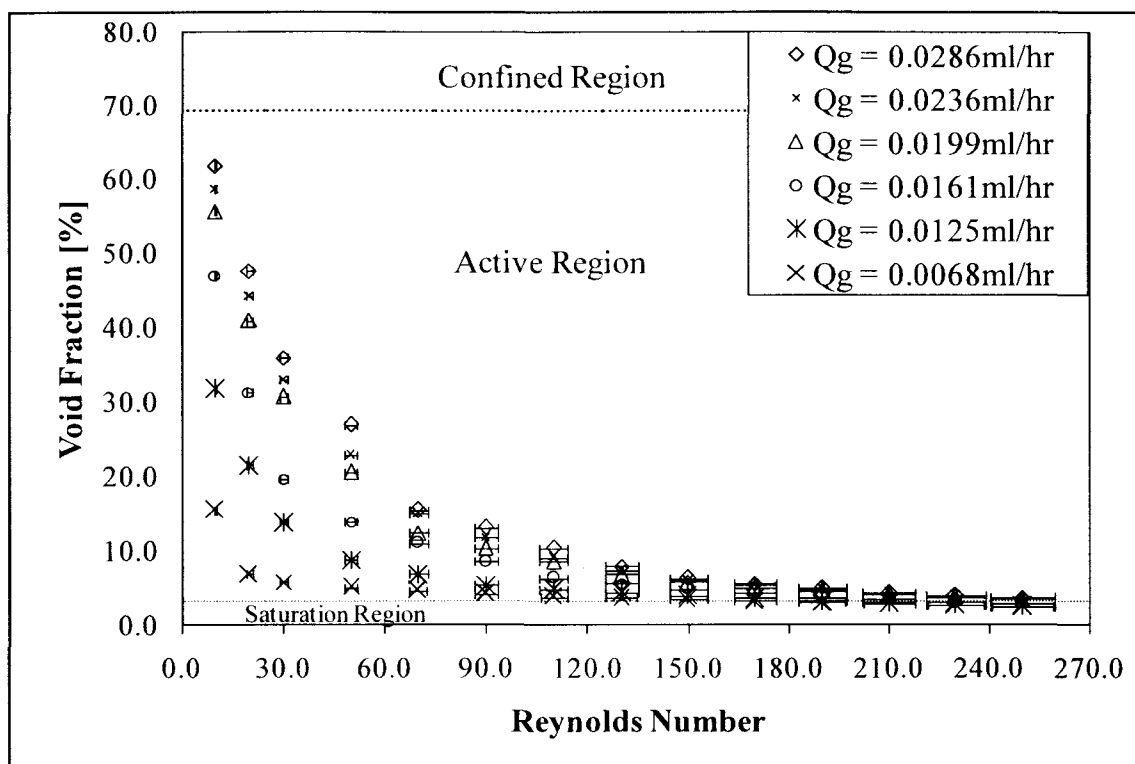


Figure 6.8 Plot gives the variation in void fraction of bubble formation in a cross-flow device for different magnitudes of Reynolds number of base fluid flow (base channel 160 $\mu$ m, secondary channel 5 $\mu$ m)

At high values of the base fluid Reynolds number, the bubble formation takes place mostly near the saturation region. For some lower values of gas flow rate, the bubble formation fall entirely in the saturation region. It can also be noted that at a very low value of gas flow rate (0.0068ml/hr), the bubble formation is very close to the saturation region even at very low values of base fluid Reynolds number. The gas flow rate (0.0068ml/hr) is very close to the minimum gas flow needed to establish a gas flow though the secondary channel of diameter 5 $\mu$ m and length 2.5cm. It can be inferred that there is a minimum threshold value of the gas flow rate through each dimensions of the secondary channel above which the bubble formation in the micro channel is dominated by the different forces that are discussed in the Section 3.1. The determination of this

threshold value can be done experimentally by varying the gas flow rate though the secondary channel of different diameters. The void fraction of bubbles formed using a  $10\mu\text{m}$  secondary channel is plotted for six different gas flow rates in Figure 6.9.

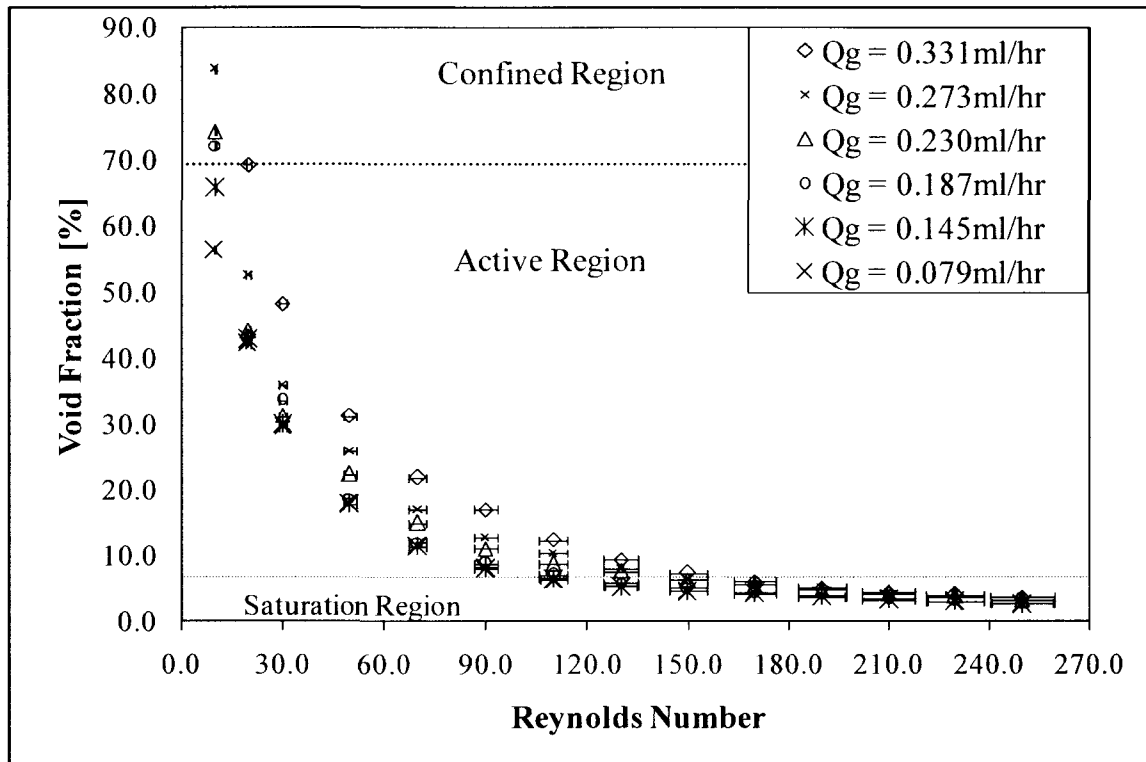


Figure 6.9 Plot gives the void fraction of bubble flow in micro channel for different magnitudes of Reynolds number (base channel  $160\mu\text{m}$ , secondary channel  $10\mu\text{m}$ )

It can be noted from Figure 6.9 that the void fraction of bubble formation using a secondary channel of  $10\mu\text{m}$  is well spread over three regions of bubble formation. At a very low value of liquid Reynolds number (10), the bubble formation for higher values of gas flow rate falls in the confined region. The bubble touches the base channel walls and moves as confined bubbles through the base channel. But when the liquid Reynolds number approaches 20, all of the bubble formation starts to form under the active region. As the Reynolds number of liquid flow increases further, the bubble formation reaches

the saturation level, and as the gas flow rate decreases, the Reynolds number of base liquid flow at which the bubbles reaches the saturation region decreases. Figure 6.10 represents the void fraction of bubble formation with a secondary channel of diameter  $15\mu\text{m}$ .

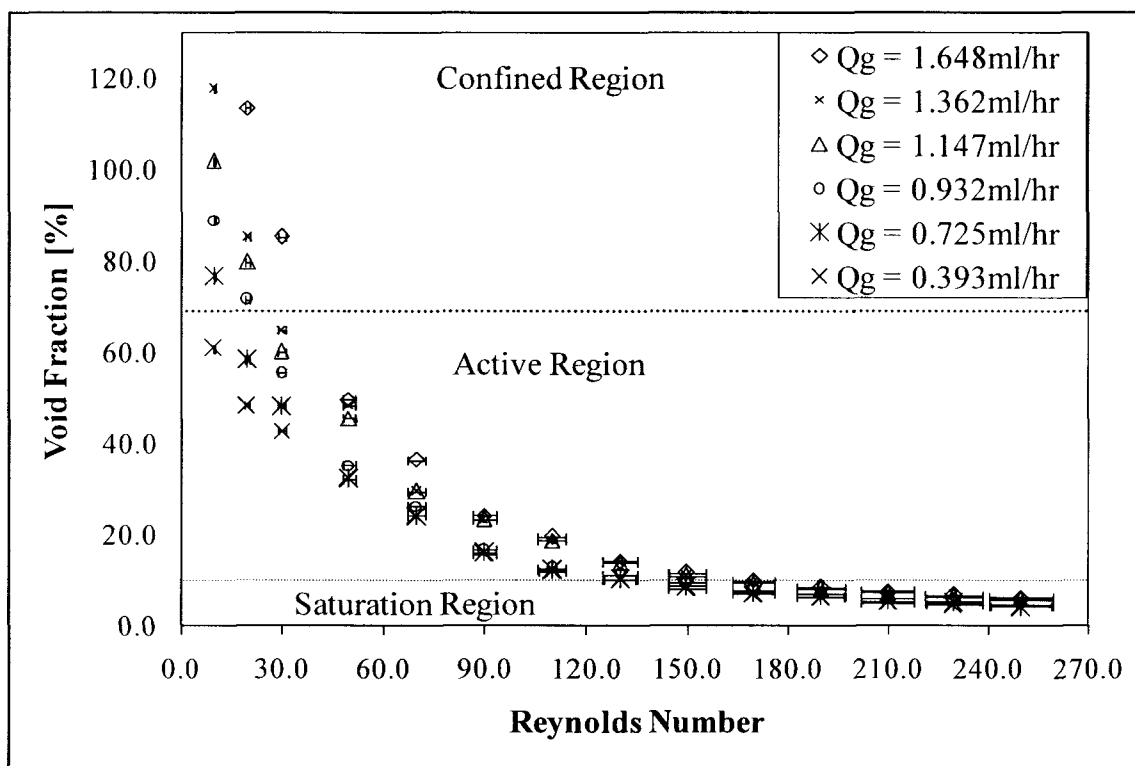


Figure 6.10 Plot gives the void fraction of bubble flow in micro channel for different magnitudes of Reynolds number (base channel  $160\mu\text{m}$ , secondary channel  $15\mu\text{m}$ )

As in the previous graphs, the base channel is  $160\mu\text{m}$ , and six different gas flow rates are used in the study. The pattern of bubble formation shown in the previous two graphs (Figures 6.8 and 6.9) is obtained in Figures 6.10 also. But the Reynolds number at which the entire bubble formation for the different gas flow rate reaches the active region shifted from 20 to 30. It can be noted that while using a bigger secondary channel, more and more bubbles tends to be formed in the confined region. In Figure 6.10 transitions

from the active region to the saturation region occur at a Reynolds number around 140. It is worth noting that in the previous case where a secondary channel of  $10\mu\text{m}$  was used, the transition from active region to saturation region started to occur at a Reynolds number of around 120, and while  $5\mu\text{m}$  tubes was used (Figure 6.8) the transition started around Reynolds number of 110. From these observations, it can be inferred that as the size of the secondary channel increases, the transition to the saturation region occurs at higher values of Reynolds numbers of base liquid flow. Figure 6.11 represents the void fraction of bubble formation while using a secondary channel of  $25\mu\text{m}$ . Unlike the previous cases, the variation in the void fraction for bubble formation is studied only for four different values of gas flow rate in Figure 6.11 because any further increase in the gas flow rate will result in the transition of bubble formation from bubbly region to wedging region as reported by Cubaud T. and Ho Chin-M [49]. From Figure 6.11 shows that as the hydraulic diameter of the secondary channel increases, the percentage of the voids fraction of bubble formation that falls under the active region decreases. More bubbles tend to form in the confined region even at small pressure drops across the secondary channel. The transition from the active to saturation region occurs at a Reynolds number of 150. The absolute pressure variation around the orifice in the base channel increases as the gas flow rate through the secondary channel varies. This effect becomes dominant as the size of the secondary channel increases.

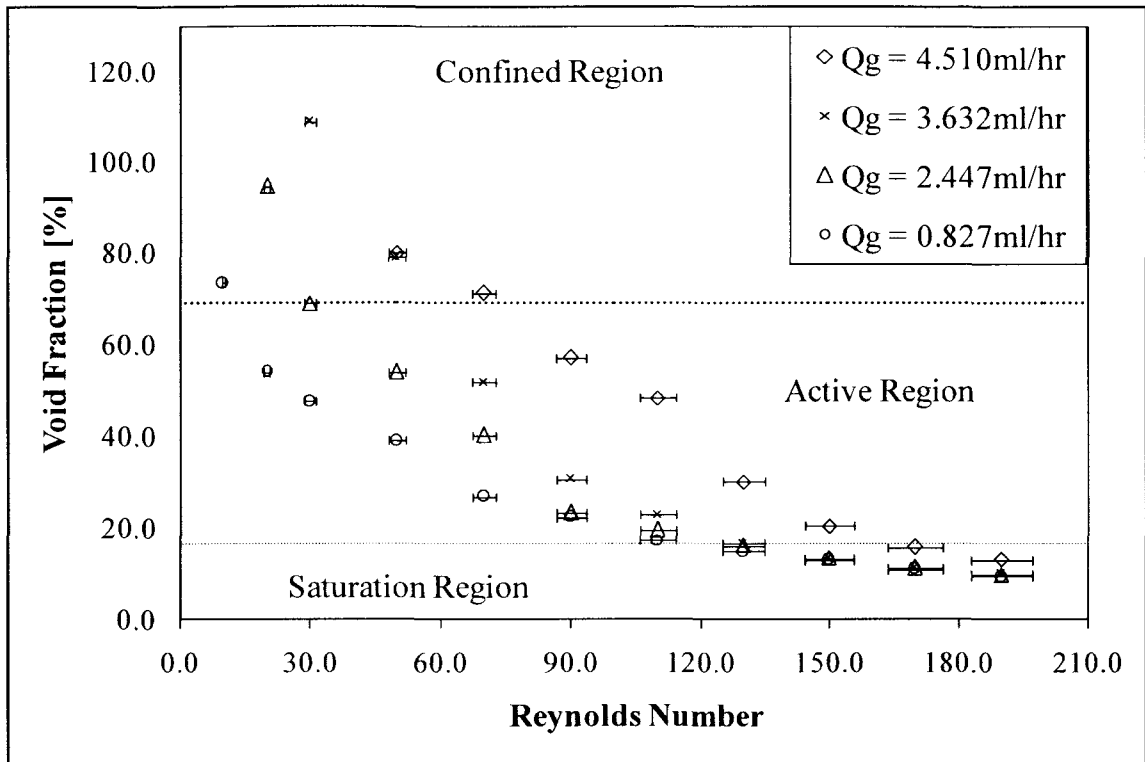


Figure 6.11 Plot gives the void fraction of bubble flow in micro channel for different magnitudes of Reynolds number (base channel  $160\mu\text{m}$ , secondary channel  $25\mu\text{m}$ )

Figure 6.12 gives the variation in void fraction of bubble formation with a secondary channel diameter  $50\mu\text{m}$ . The variation in the void fraction for bubble formation with  $50\mu\text{m}$  secondary channels is studied only for three values of gas flow rates. In Figure 6.12, it can be noted that even though the gas flow rate through the secondary channel varies widely, the diameter of the bubbles formed in the base channel is not varying much, and, at higher values of Reynolds number, the bubble diameter, obtained for all three gas flow rates remains the same. This occurs because even though the gas flow rate is varying widely, the corresponding pressure drop across the secondary channel varies a little (0.96 to 1.86PSI). This observation can be used to infer that the variation in the bubble diameter with the change in gas flow rate is contributed mainly by

the change in pressure drop across the secondary channel. As discussed earlier, the shrinking of an active region with the increase in the secondary channel diameter occurs in this case study also, and the transition of the void fraction of bubble formation from active to saturation region occurs at a Reynolds number of around 150.

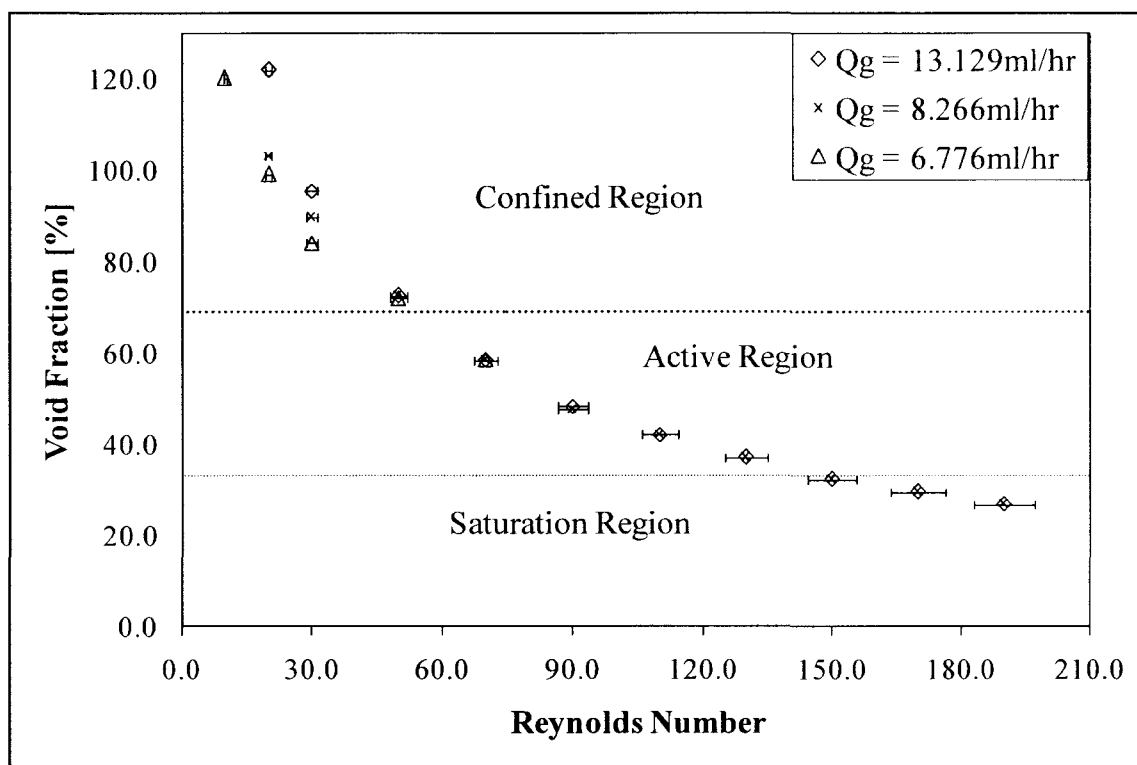


Figure 6.12 Plot gives the void fraction of bubble flow in micro channel for different magnitudes of Reynolds number (base channel  $160\mu\text{m}$ , secondary channel  $50\mu\text{m}$ )

#### 6.1.4 Case 4: Variable parameter: Hydraulic diameter base channel

In Chapter 1, it was stated that many researchers have tried to resolve the issue of bubble confinement by using base micro channels of high width to depth ratio [33, 37, 40]. Here in this section, the variation in the bubble diameter and void fraction of bubble formation in base channels of different hydraulic diameters is analyzed. The depth of the

base micro channel is kept constant, and the width is varied from 130 $\mu\text{m}$ , 170 $\mu\text{m}$  and 270 $\mu\text{m}$ , thus changing the hydraulic diameter of the base channel. Figure 6.13 represents the variation in bubble diameter with the variation of hydraulic diameter of base channel.

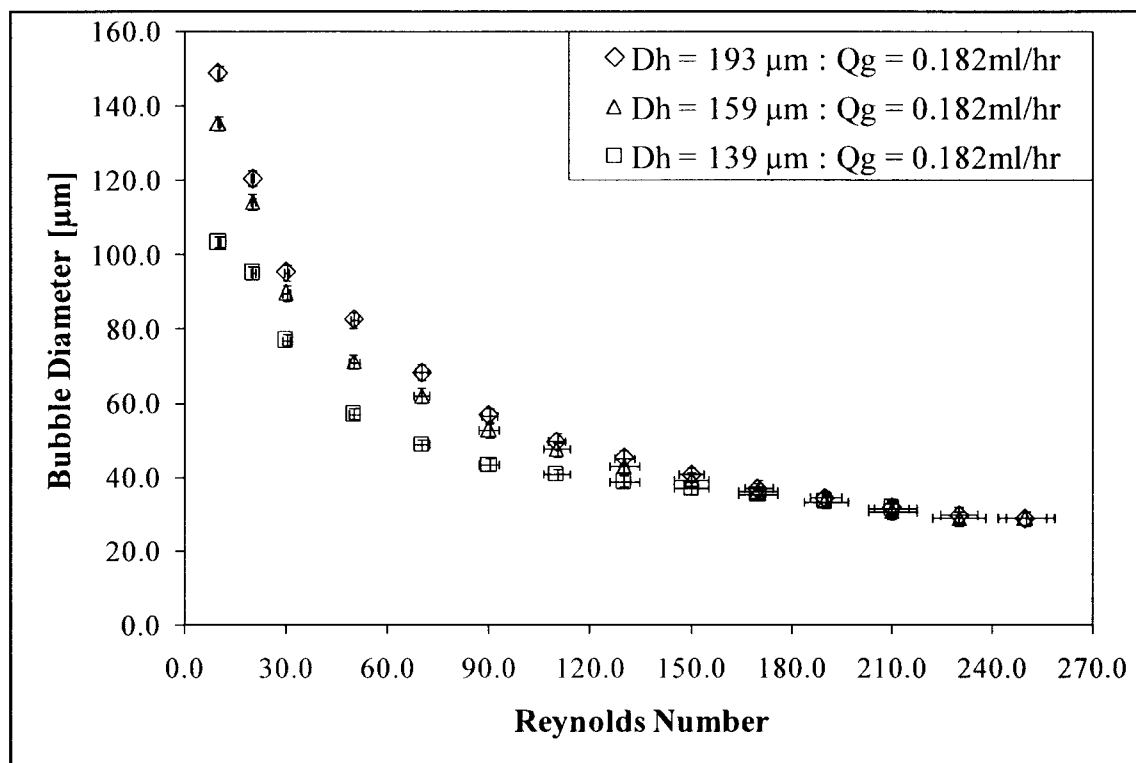


Figure 6.13 Plot gives the comparison of bubble diameter for three different hydraulic diameters of base channel (secondary channel = 10 $\mu\text{m}$ )

Figure 6.15 represents the variation in the void fraction of bubble formation in the base channel of hydraulic diameter 193 $\mu\text{m}$  (width 270 $\mu\text{m}$  and depth 150 $\mu\text{m}$ ) for two different gas flow rates. From Figure 6.13 it can be seen that with change in the hydraulic diameter of the base channel from 139 $\mu\text{m}$  to 193 $\mu\text{m}$ , there is not much change in the bubble diameter formed in the base channel. At low values of Reynolds number, the bubbles formed in the channels with bigger hydraulic diameter tend to be little bigger than those formed in the smaller channel, but as the Reynolds number increases, the

bubble diameters are very close to one another and fall within the uncertainty limit of each other. One interesting thing that can be noted about the formation of bubbles in the base channel with higher width to depth ratio is that the bubbles that are formed in the confined region are not confined to all the four walls of the base channels. The bubbles take on a disk shape (sphere with both the top and bottom end chopped off) and will be confined to the top and bottom walls of the base channel, letting the base liquid flow freely through both sides of the bubble. Figure 6.14 shows the picture of a bubble formed in a high aspect ratio base channel. The bubble shown in Figure 6.14 is confined only to the upper and lower walls of the base channel.

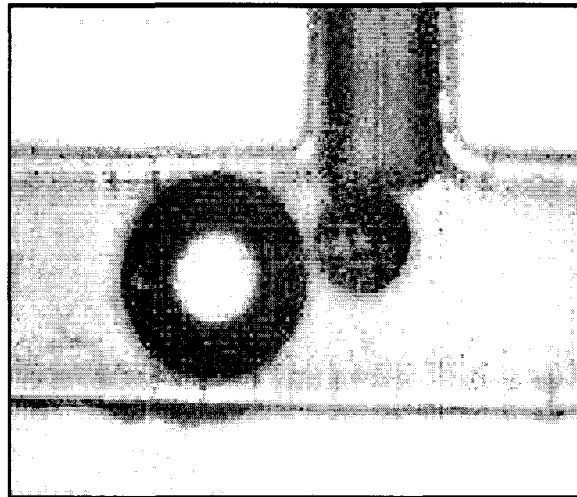


Figure 6.14 Bubble formed in base channel of width to depth ratio greater than one (Base channel =  $193\mu\text{m}$ , secondary channel =  $10\mu\text{m}$ )

Figure 6.15 represents the void fraction of bubble formation in a base channel with width to depth ratio larger than one for two different values of gas flow rate through the secondary channel. Since the transition between the confined and active region is determined by the area of the bubble with the diameter equal to the shortest side of the



base channel, the transition region occurs below 45% in Figure 6.15. The transition from the active region to saturation region occurs at a base liquid Reynolds number of around 120, and there is not much change in the void fraction of bubble formation at higher Reynolds number when the gas flow rate is varied.

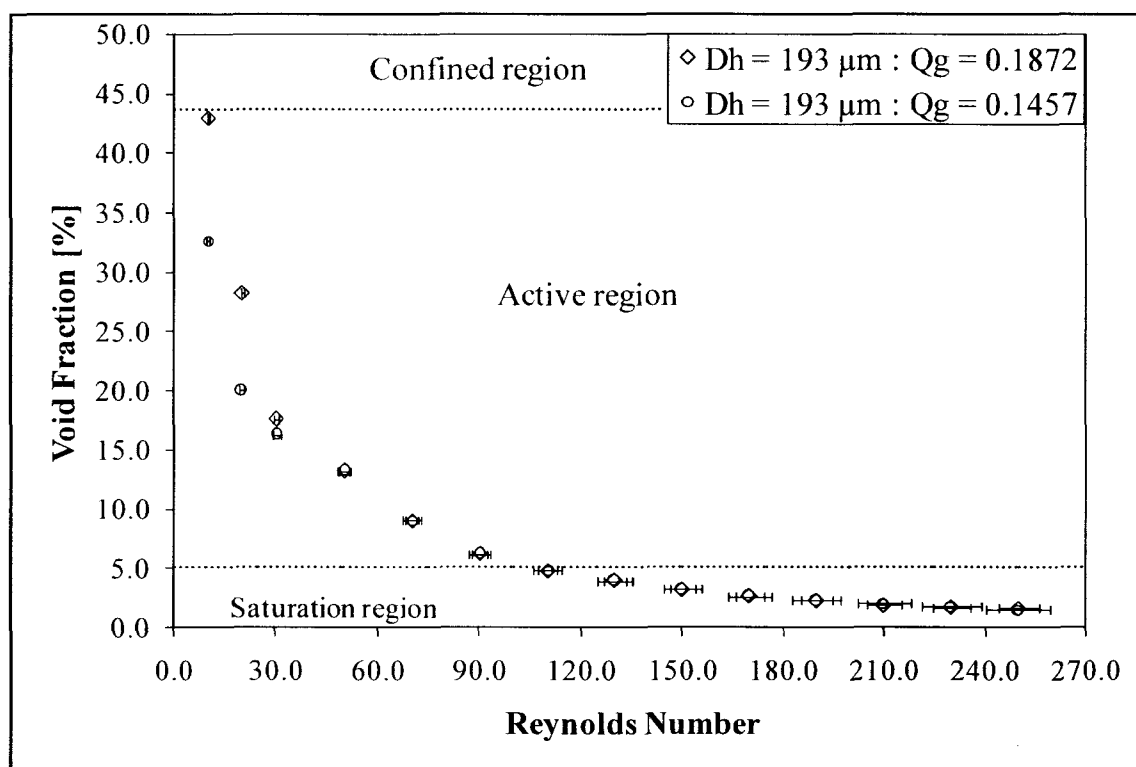


Figure 6.15 Plot gives the void fraction of bubble formation in base channel with high aspect ratio for different magnitudes of Reynolds number of base liquid (base channel 193 $\mu\text{m}$ , secondary channel 10 $\mu\text{m}$ )

### 6.1.5 Case 5: Variable parameter: Different gas through secondary channel

The change in the void fraction of bubble formation in a base channel with a change in the gas that is being flown through the secondary channel is studied in this section. The gases used in this study are oxygen and nitrogen, and their physical properties at 27°C are given in Table 6.1.

Table 6-1 Physical properties of gases used in the case study

<b>Gas</b>	<b>Density [kg/m<sup>3</sup>]</b>	<b>Dynamic Viscosity [kg/ms]</b>	<b>Kinematic Viscosity [m<sup>2</sup>/s]</b>
<b>Oxygen</b>	1.421	1.78E-05	1.59E-05
<b>Nitrogen</b>	1.123	1.91E-05	1.34E-05

The void fraction of bubble formation in the base channel with two different gases is represented in Figure 6.16. It can be noted that the void fraction of bubble formation for both the gases at two different gas flow rate lies very close to each other. As was discussed in most of the previous cases, the void fraction of bubble formation varies with Reynolds number of the base fluid. At low Reynolds number of liquid flow, the void fraction of bubble formation shows a good variation with respect to the gas flow rate, but stays very close to one another at high Reynolds number. But even at very low values of Reynolds number of base liquid, the void fraction of bubble formation while using two different gases (oxygen and nitrogen) is very close to each other in their respective flow rates.

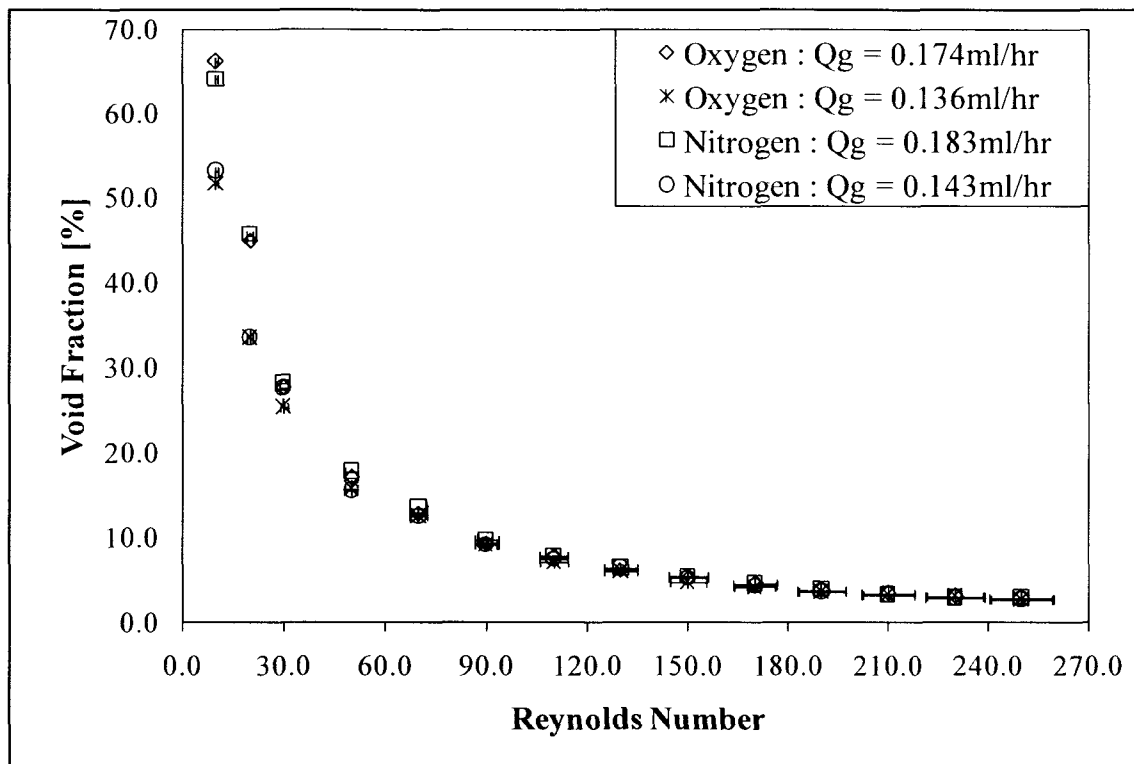


Figure 6.16 Plot gives the comparison of void fraction of bubble formation for two different gases at same pressure drop across the secondary channel (base channel  $150\mu\text{m}$ , secondary channel  $10\mu\text{m}$ )

The study on the effect of using different gases on the bubble formation and detachment diameter is limited only to two gases. While the forces acting on the bubble formation, are considered the properties of the gas being used has influence only on the momentum force and inertial force, and both the forces are negligible compared to the surface tension force and the drag force. This assumption is well supported by the results obtained from the study presented in this case. So even if a third gas, for example, argon, which has high viscosity and density compared to the currently used gases is used, the bubble detachment diameter will remain the same (Argon: density  $1.784\text{kg/m}^3$ , viscosity  $2.272\text{e-}5\text{kg/ms}$ , kinematic viscosity  $1.273\text{e-}5\text{m}^2/\text{s}$ ). The slight variation in the gas flow rates between oxygen and nitrogen at a constant pressure drop across the secondary

channel is accounted for by the change in density and viscosity of the respective gases. The void fraction of bubble formation in the base channel for three different gas flow rates of oxygen through the secondary channel is plotted in Figure 6.17. As discussed in the Section 6.1.3, while using a secondary channel of diameter  $10\mu\text{m}$  and gas as nitrogen, transition from active to saturation region happens at a Reynolds number of around 120.

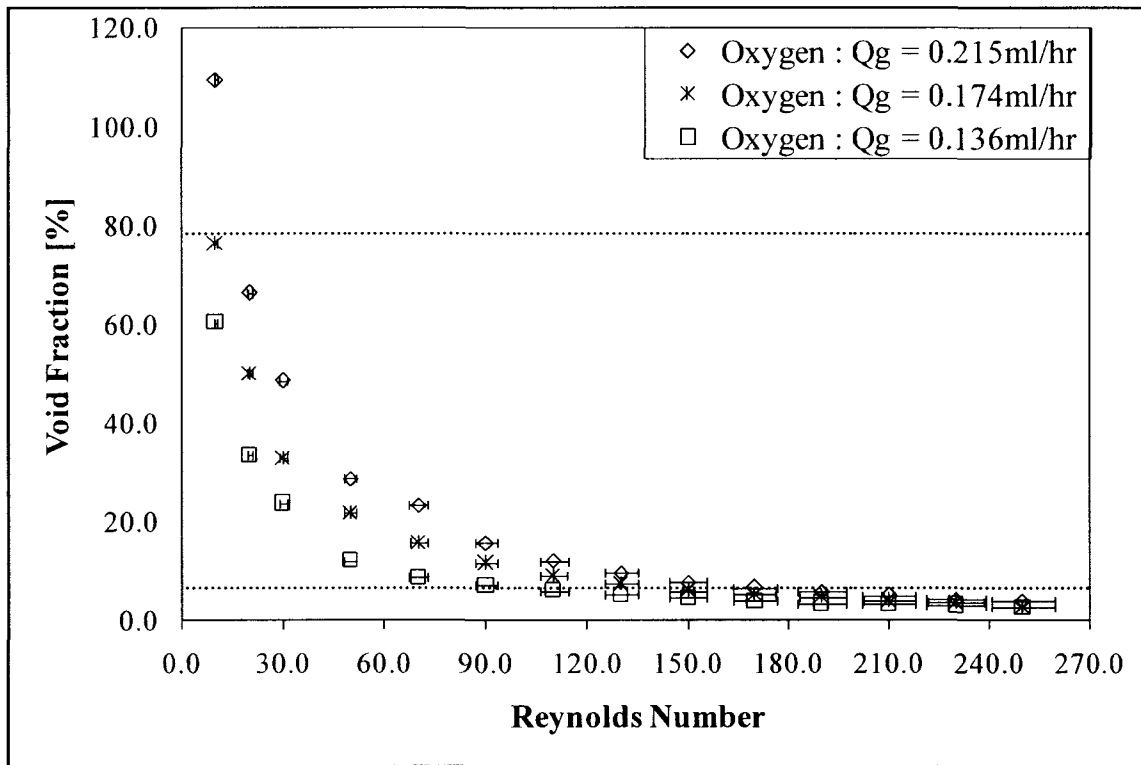


Figure 6.17 Plot gives the void fraction of oxygen bubble formation in base channel for different magnitudes of Reynolds number (base channel  $150\mu\text{m}$ , secondary channel  $10\mu\text{m}$ )

### 6.1.6 Case 6: Variable parameter: Different base liquids

As discussed in the Section 6.1, the dominating forces acting on the bubble formation and bubble detachment from an orifice in a cross-flow device is the surface tension force and the drag force. The surface tension force depends on the surface tension

of the base liquid flowing through the base channel, and the drag force depends on the Reynolds number of the base liquid flow. The Reynolds number of a liquid flowing through a tube is determined by the velocity of the liquid, hydraulic diameter of the tube and inverse of kinematic viscosity of the liquid. So, if the hydraulic diameter of the base channel and velocity of liquid flow is kept constant, then the Reynolds number of the liquid flow will be determined by the kinematic viscosity of the liquid that is flowing through the base channel. Thus, in order to understand the factors affecting the bubble formation inside the base channel, a study based on varying kinematic viscosity of the base liquid is relevant here. This section studies the variation in bubble diameter while using different liquids having different kinematic viscosities flowing through the base channel of the same dimension. Four liquids are used in this study: 70% Isopropanol, de-ionized water, Toluene and Acetone. The physical properties of these liquids that are used in this study are listed in Table 6.2.

Table 6-2 Physical properties of liquids used in the case study

<b>Liquid</b>	<b>Density [kg/m<sup>3</sup>]</b>	<b>Dynamic Viscosity [kg/ms]</b>	<b>Kinematic Viscosity [m<sup>2</sup>/s]</b>	<b>Surface Tension [N/m]</b>
<b>70% Isopropanol</b>	874	2.27E-04	2.60E-06	2.27E-02
<b>Water</b>	997	9.11E-04	9.13E-07	7.28E-02
<b>Toluene</b>	862	5.69E-04	6.60E-07	2.84E-02
<b>Acetone</b>	784.58	3.22E-04	4.10E-07	2.33E-02

Figure 6.18 represents the void fraction of bubble formation with four different liquids flowing through the base channel and having a constant gas flow rate of 0.187ml/hr through the secondary channel.

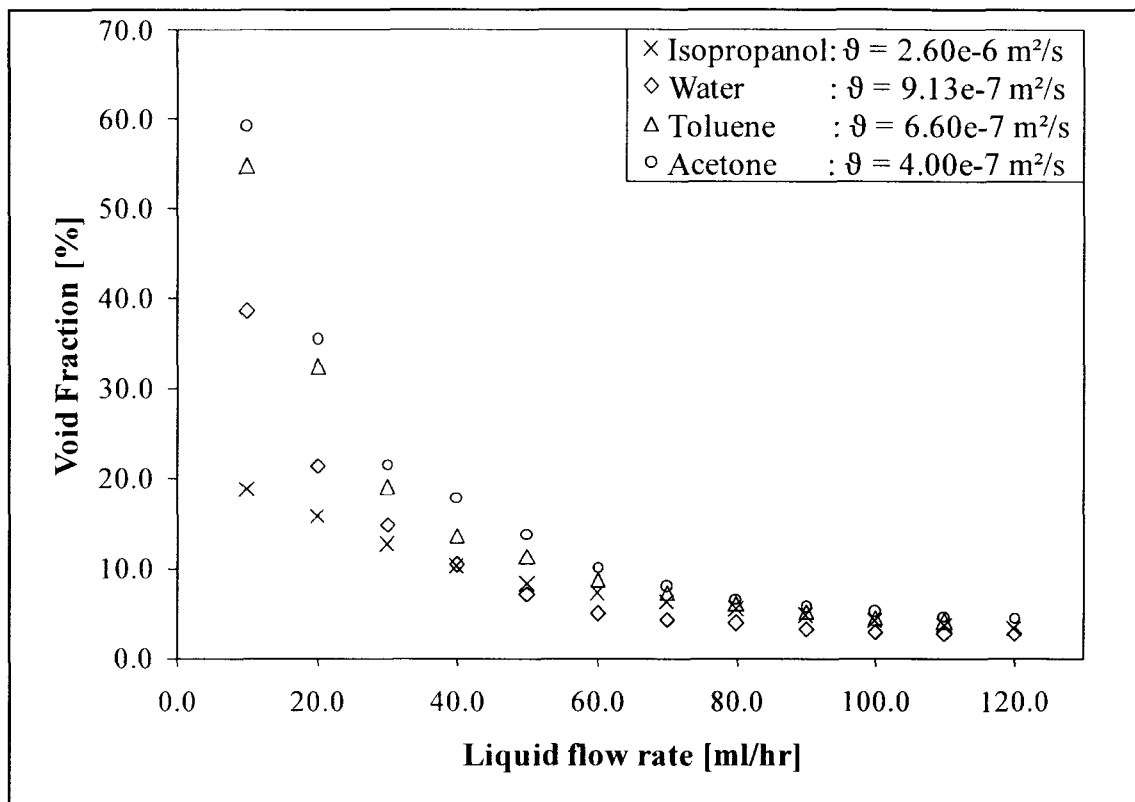


Figure 6.18 Plot gives the void fraction of bubble formation in base channel for base liquids with different kinematic viscosities (base channel  $162\mu\text{m}$ , secondary channel  $10\mu\text{m}$ , Gas flow rate  $0.187\text{ml/hr}$ )

It can be noted from Figures 6.18 and 6.19 that the graphs are plotted with a liquid flow rate in the base channel at X axis (instead of constant Reynolds number) to keep the velocity of liquid flow constant even when different liquids are used. Since the velocity of the liquid flow through the base channel is kept constant, the variation in the void fraction of bubble formation will depend only on the dynamic viscosity and density of the base liquid, and these properties are combined together to obtain the kinematic viscosity of the base liquids. The figure representing the void fraction of bubble formation while using different liquids with distinct physical properties are plotted for two different constant gas flow rates to check whether the trend shown by the graph at one gas flow

rate is repeated for other gas flow rates also. It can be noted from Figure 6.18 that the void fraction of bubble formation is inversely proportional to the kinematic viscosity of the base liquid. As the kinematic viscosity decreases, the void fraction of bubble formation and the bubble diameter increases, so does the bubble diameter. This change is very obvious at low flow rates of the base liquid. As the magnitude of base liquid flow rates increases, the variation in the void fraction of bubble diameter with variation in kinematic viscosity decreases. At very high values of liquid flow rates, the plots of void fraction tends to stay closer to one another. Another important observation that can be made from Figure 6.18 is that the variation of the void fraction with the flow rate of base liquid is more when the kinematic viscosity is low. For example, Isopropanol has the highest kinematic viscosity compared to the other testing liquids and it can be observed that the variation in the void fraction of bubble formation while using Isopropanol is lower than the other liquids. Acetone has the lowest value of kinematic viscosity and has the maximum variation of void fraction of bubble formation. Figure 6.19 represents the void fraction of bubble formation for different base fluids for a gas flow rate of 0.145ml/hr through the secondary channel.

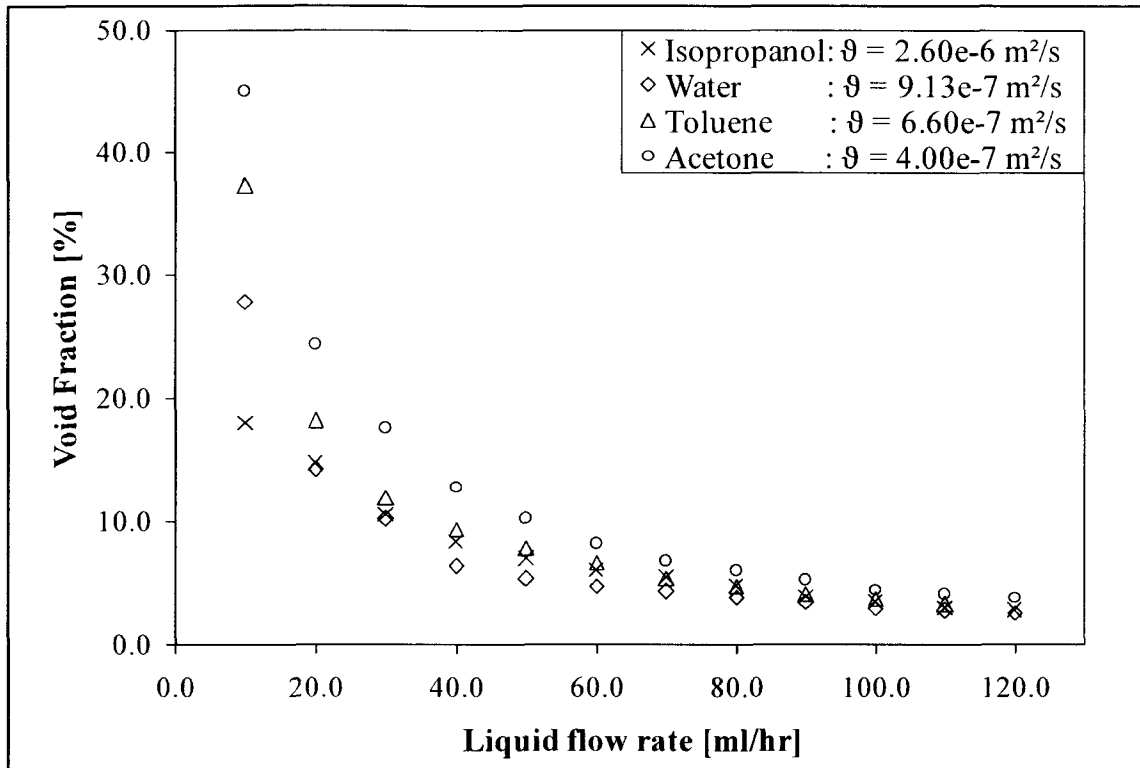


Figure 6.19 Plot gives the void fraction of bubble formation in base channel for base liquids with different kinematic viscosities (base channel  $162\mu\text{m}$ , secondary channel  $10\mu\text{m}$ , Gas flow rate  $0.145\text{ml/hr}$ )

It can be observed from Figure 6.19 that the trends shown in Figure 6.18 are followed very closely for a different flow rate of gas through the secondary channel. The void fraction for bubble formation with Isopropanol has the lowest value as before, and Acetone has the highest void fraction. Figure 6.20 represents the variation in the void fraction of bubble formation at constant values of Reynolds numbers for different liquids flowing through the base channel.



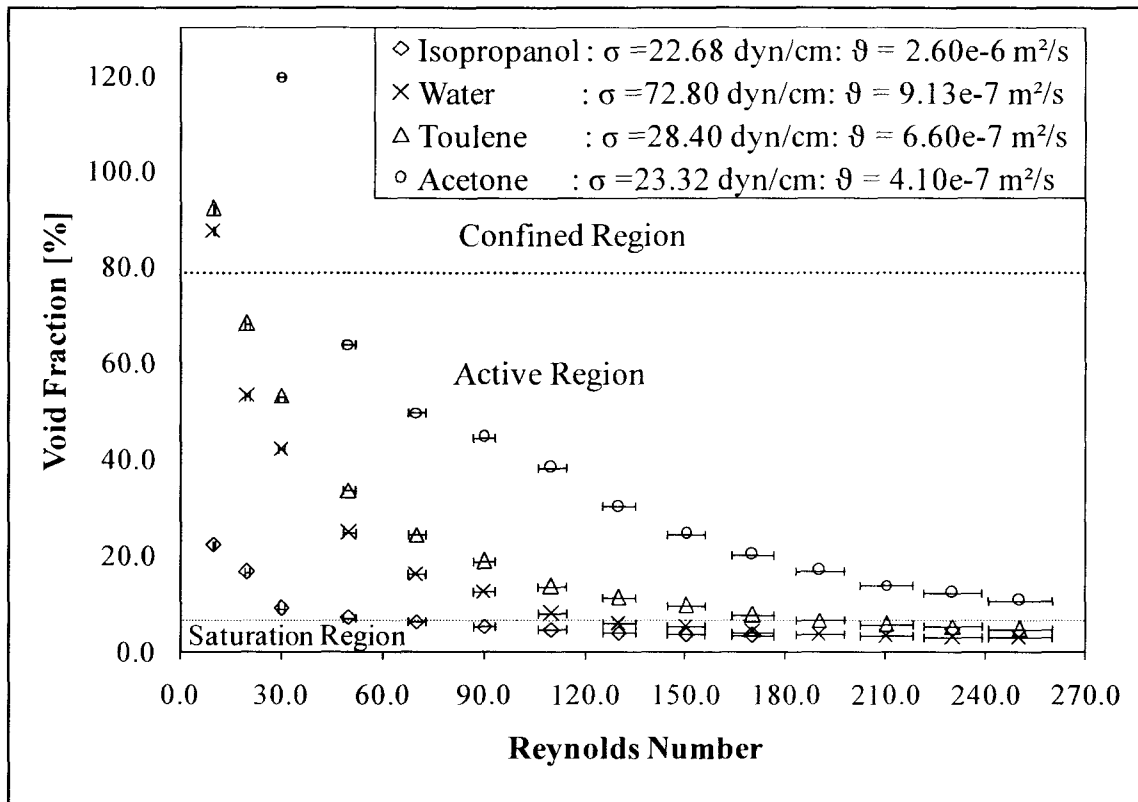


Figure 6.20 Plot gives the void fraction of Nitrogen bubble formation in base channel for different magnitude of Reynolds numbers (base channel  $162\mu m$ , secondary channel  $10\mu m$ , Gas flow rate  $0.187 ml/hr$ )

The effect of surface tension of the base liquid on the void fraction of bubble formation is also included in Figure 6.20. It can be observed that the trend shown in the previous study with a constant base liquid flow rate is repeated while using constant Reynolds number of liquid flow. While using a constant liquid flow rate for the comparison of the void fraction of bubble formation, the plot tends to merge at higher liquid flow rates. But in this study, with constant Reynolds numbers, the plots for the void fraction is clearly distinct from one another except for water and Isopropanol, which merges at very high values of Reynolds numbers. As the void fraction of bubble formation decreases with the increase in kinematic viscosity of the base liquid, more and

more bubbles tends to form in the active or saturation region. The surface tension of the base liquid alone seems to have less effect on determining the bubble diameter at detachment because even though water has a surface tension of almost three times that of Isopropanol, the bubble diameter obtained while using water as base liquid is much greater than that obtained while using Isopropanol as the base fluid.

The major goal of this project is to produce microbubbles which have a diameter less than  $15\mu\text{m}$ . The flow focusing technique in the cross-flow bubble/droplet generators as introduced to attain this objective. But even without using the flow focusing technique, the objective was attained by producing microbubbles of a size less than  $15\mu\text{m}$  in base channels of hydraulic diameter  $160\mu\text{m}$ , using a secondary channel of diameter  $2\mu\text{m}$ . Microbubbles of a size as small as  $11\mu\text{m}$  were produced in the base channel at a flow rate of  $10\text{ml/hr}$ . Table 6.3 gives the bubble diameter with corresponding base liquid flow rate obtained while using secondary channel of hydraulic diameter of  $2\mu\text{m}$ .

Table 6-3 Diameter of bubbles generated in a base channel of hydraulic diameter  $162\mu\text{m}$  and secondary channel diameter  $2\mu\text{m}$

<b>Liquid Flow rate[ml/hr]</b>	2	3	4	5	7	10
<b>Bubble Diameter [<math>\mu\text{m}</math>]</b>	21.79	18.15	16.34	13.62	12.71	10.89

## **6.2 Cross-flow Bubble Generator with Flow Focusing**

The flow focusing technique introduced in the cross-flow microbubble/droplet generators in this study is the first ever reported study to introduce flow focusing in cross-flow bubble generators. The purpose of using the flow focusing technique in cross-flow bubble generators is to focus the base liquid flow onto the side wall of the base

channel on which the orifice is situated, and thereby make the drag force acting on the bubble (during its formation from the orifice) more effective. Usually when the liquid flows through a channel, the maximum flow velocity will be located towards the center of the channel, and the velocity of liquid flow towards the side walls of the channel will be zero. Figure 6.21 represents the velocity profile of liquid flow through a base channel with and without the flow focusing technique imposed. It can be noted from Figure 6.21 that the velocity of the liquid flow near the walls of the base channel without flow focusing is zero, and in base channels with flow focusing, the maximum velocity of the base liquid flow is shifted near to the base channel wall around the orifice. This focused velocity in front of the orifice will help the detachment of the bubble from the orifice at a smaller diameter than in a normal channel.

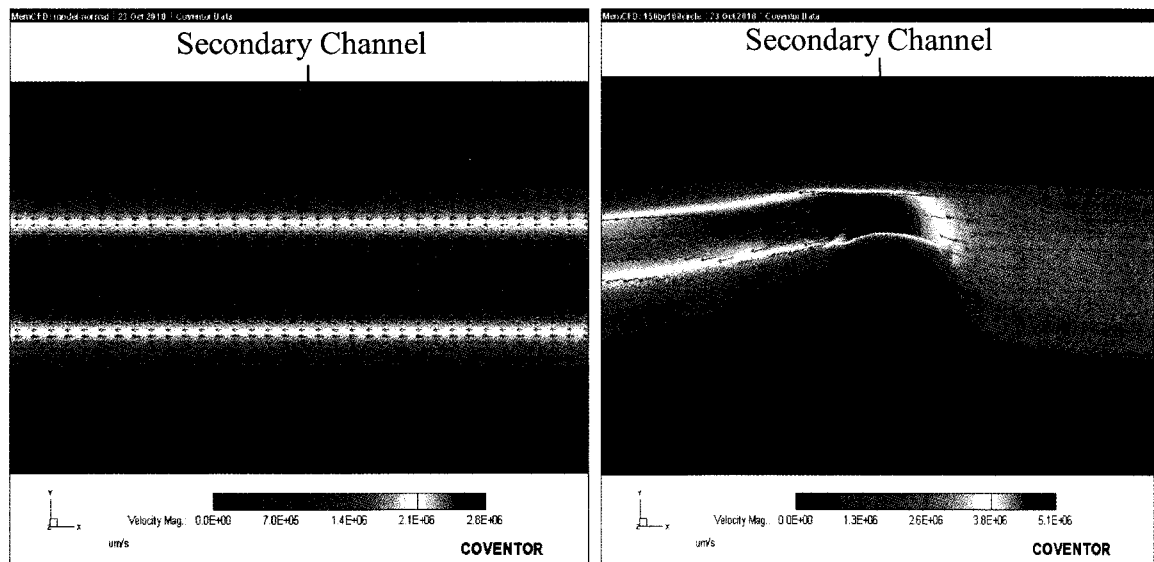


Figure 6.21 Contour plot of velocity profile in a base channel with and without flow focusing (hydraulic diameter = 150 $\mu$ m, flow focusing structure = 100 $\mu$ m)

As stated in Chapter 3, a feasibility study on introducing the flow focusing device was done using the computational fluid dynamics software COMSOL<sup>®</sup> [45]. In addition to proving the superiority of using the flow focusing technique in the cross-flow bubble generators, an optimization study was done based on the shape and geometry of the flow focusing structures. The shapes used in the optimization study were discussed in Chapter 3 and a few of the contour plots obtained from the results of the study are presented in this chapter. The base channel used in the study was 100 $\mu\text{m}$  in hydraulic diameter with 20 $\mu\text{m}$  secondary channel. Shapes used in the study were a circle of 50 $\mu\text{m}$  diameter placed in the middle of the base channel, a semi-circle of radius 75 $\mu\text{m}$ , and a triangle of height 75 $\mu\text{m}$ . Figure 6.22 gives the contour plot of the results obtained in the study for a particular Reynolds number.

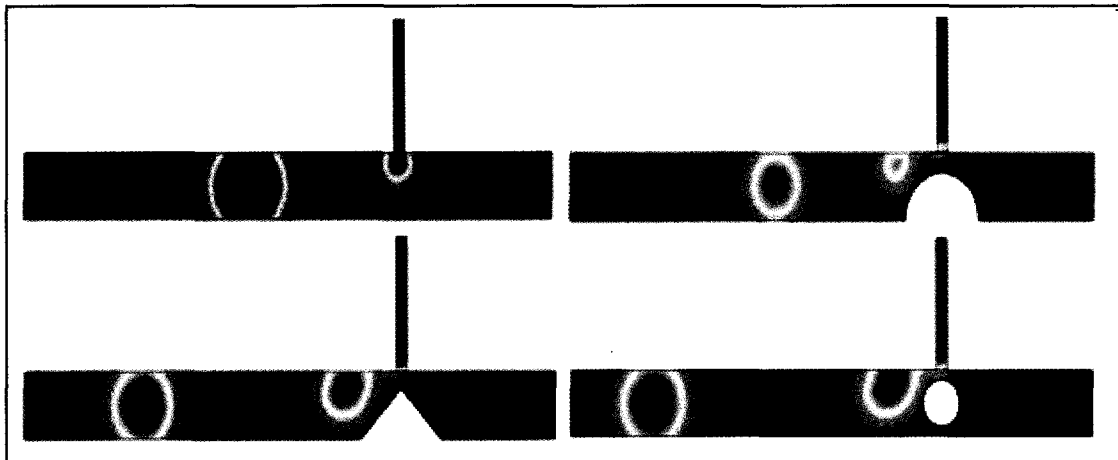


Figure 6.22 Contour plot of bubble formation in base channel with different shapes of flow focusing structures (hydraulic diameter =100 $\mu\text{m}$ , flow focusing structure =50 $\mu\text{m}$  and 75 $\mu\text{m}$ , secondary channel = 20 $\mu\text{m}$ ) [45]

Figure 6.23 represents the variation in bubble diameter with the introduction of flow focusing structures inside the base channel, and variation in bubble diameter with the change in shape of the flow focusing structures.

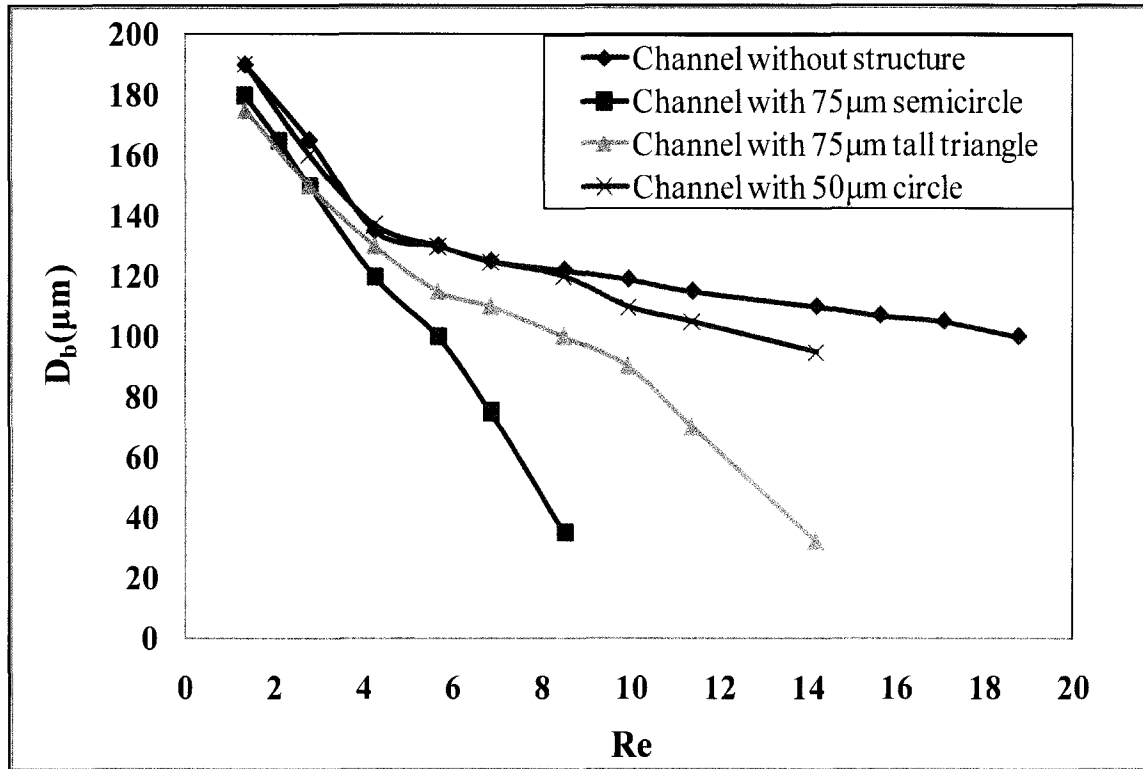


Figure 6.23 Bubble diameter in cross-flow bubble generator with and without flow focusing structures of different shapes (hydraulic diameter = 100 μm, secondary channel = 20 μm) [45]

The circular structure placed in the middle of the base channel in front of the orifice seems to have a very slight effect on the bubble formation compared to the base channel without flow focusing. So, in the experimental study of introducing flow focusing structures in the base channel of the cross-flow device a circular structure is avoided. Instead, a rectangular structure is introduced. The flow focusing study in the cross-flow device is divided into four different cases in this study. The first case studies

the benefit of introducing a flow focusing structure inside the cross-flow device, and the second case studies the bubble formation in the base channel with flow focusing with two different diameters of the secondary channel. The third case studies the effect of introducing different shaped flow focusing structures inside the base channel, and the fourth case studies the variation in bubble diameter by changing the base width of the flow focusing structures. Figure 6.24 shows bubble formation in a cross-flow device with flow focusing structure.

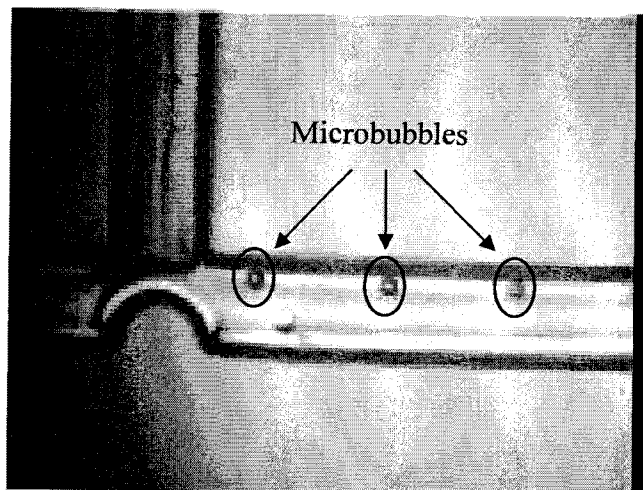


Figure 6.24 Bubbles formed in a cross-flow bubble generator with semi-circular flow focusing structure embedded in base channel (base channel  $160\mu\text{m}$ , secondary channel  $10\mu\text{m}$ , flow focusing structure height  $100\mu\text{m}$ )

### 6.2.1 Case 1: Comparison of cross-flow device with and without flow focusing

A comparison of the velocity profile of liquid flow in the base channel of a cross-flow bubble generator with and without flow focusing structure is shown in Figure 6.21. In the base channel with the flow focusing structure, the maximum velocity of the liquid flow is shifted towards the side wall of the base channel around the orifice. This will help

in the detachment of the bubbles inside the channel at a smaller diameter compared to the bubbles formed in the normal channel. Semi-circular structures used for flow focusing in the base channels are used for the purpose of comparison because of their better performance in the feasibility study. Figure 6.25 represents the comparison between normal base channel and base channel with semi-circle structure of  $100\mu\text{m}$  radius.

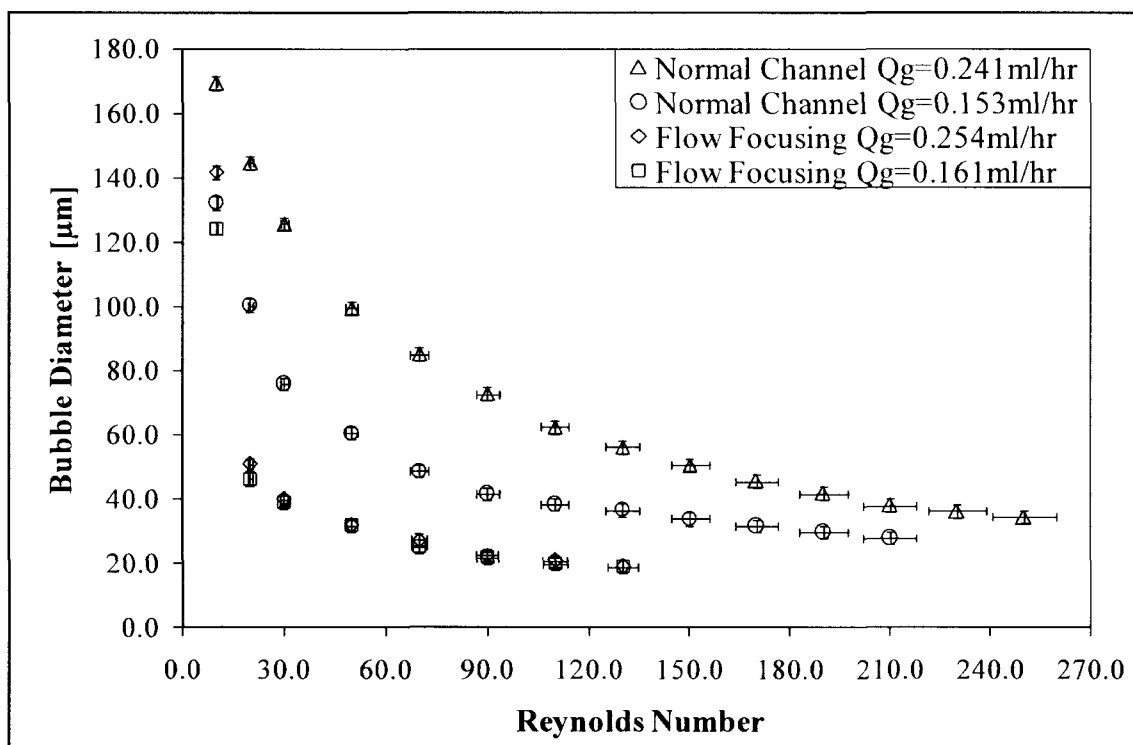


Figure 6.25 Plot gives the comparison between bubble diameters formed in cross-flow devices with and without flow focusing (base channel  $160\mu\text{m}$ , secondary channel  $10\mu\text{m}$ , flow focusing structure height  $100\mu\text{m}$ )

It can be observed from the figure that the bubble diameter decreases very abruptly with the use of a flow focusing structure inside the cross-flow bubble generator for two distinct gas flow rates through the secondary channel. At a very low value of base liquid flow Reynolds number (10), the bubble diameter formed using the flow focusing

technique is close to the bubble formed in the normal channel. This happens due to the blocking of the entire channel by the bubble formed from the orifice. The base fluid has some delay to build up enough pressure to push the bubble off from the orifice. But as the Reynolds number of liquid flow increases, the bubble diameter falls off very quickly and reaches the saturation region. Another interesting thing that can be noted is that the bubble diameter generated in the cross-flow bubble generator with flow focusing structure does not change with the change in the gas flow through the secondary channel. It shows a slight variation at the liquid flow Reynolds number of 10, but stays close to one another for higher magnitudes of Reynolds numbers. The smallest bubble formed by introducing the flow focusing technique in this case study was around  $20\mu\text{m}$  in diameter.

### **6.2.2 Case 2: Comparison of bubble formation in secondary channel with different hydraulic diameters**

Figure 6.26 gives the comparison of the void fraction of bubble formation in the base channel with a semi-circle flow focusing structure embedded in it, and having two different secondary channels of different diameters, and the same length with the same pressure drop of gas flow applied across them. The secondary channels used in the study have hydraulic diameters of  $10\mu\text{m}$  and  $5\mu\text{m}$ . The graphs are plotted for two different gas flow rates through both the secondary channels. The void fraction of the bubble formation from the secondary channels of smaller diameter is less compared to the void fraction of the bubbles from the bigger channel.



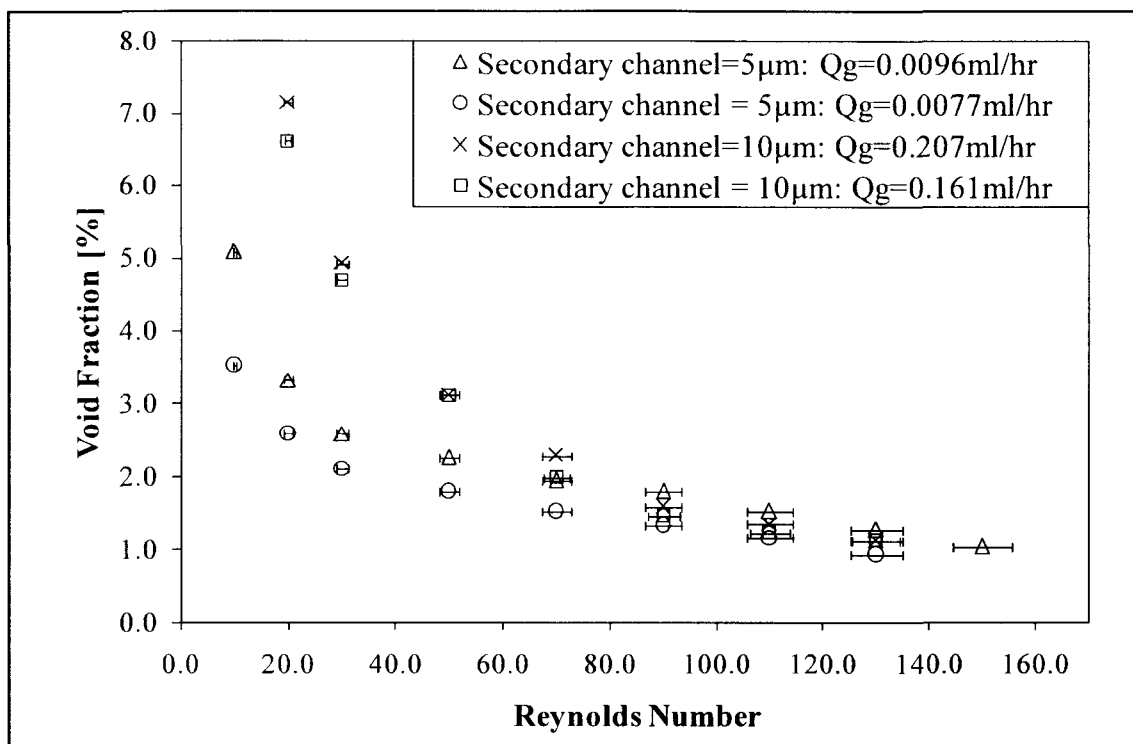


Figure 6.26 Plot gives the comparison between the void fractions of bubbles formed in base channel with semi-circle structure for two different secondary channel diameters (base channel 160 $\mu\text{m}$ , flow focusing structure height 100 $\mu\text{m}$ )

The comparison plot represented in Figure 6.26 is located mostly in the saturation region and lower portion of the active region. It can be noted that at low values of Reynolds numbers, the plot of void fraction varies with the change in the secondary channel diameter, and at higher magnitude of Reynolds number and as the bubble formation hits the saturation region, the void fraction of bubble formation from both the channels comes closer. It can be inferred that the bubble formation in the base channel using the flow focusing technique in the active region is well affected by the hydraulic diameter of the secondary channel, but the bubble formation in the saturation region is not much affected by the change in the secondary channel hydraulic diameter.

### 6.2.3 Case 3: Comparison of different shapes of flow focusing structures on cross-flow device performance

This section compares the bubble generation efficiency of cross-flow bubble generators with different shapes of structures used for flow focusing in the base channel. The chrome mask used for the manufacturing of the flow focusing structures inside the base channel is shown in Figure 6.27. The flow focusing structure is placed in the base channel, and the channel perpendicular to the base channel holds the fused silica tube.

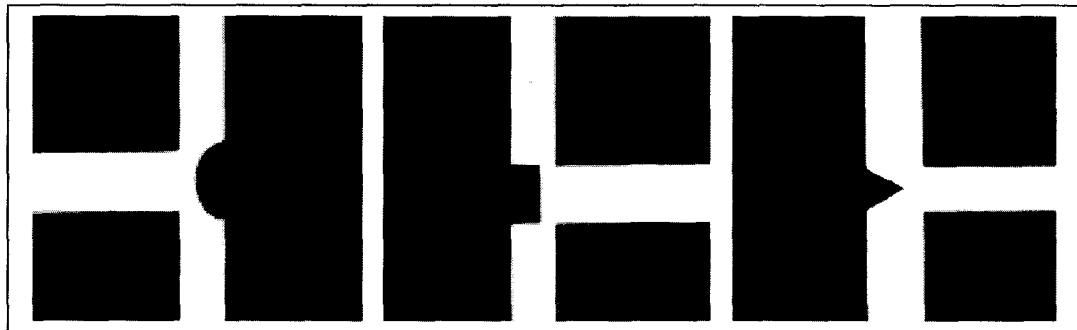


Figure 6.27 Mask used for the manufacturing of different shapes of flow focusing structures. (base channel  $150\mu\text{m}$ , flow focusing structure height  $100\mu\text{m}$ )

Figure 6.28 represents the comparison of bubble diameters formed in a cross-flow device with three different shapes of flow focusing structures embedded in the base channel. As predicted by the feasibility study, the base channel with a semi-circle structure shows the best performance during the experimental study followed by the triangular structures. The rectangle shows the least performance. In order to understand the reasoning behind the variation in bubble diameter even while the cross-sectional area in front of the orifice remains the same while using all the three different shaped structures, the flow pattern in the region has to be studied. This is attained by using CFD software CoventorWare.

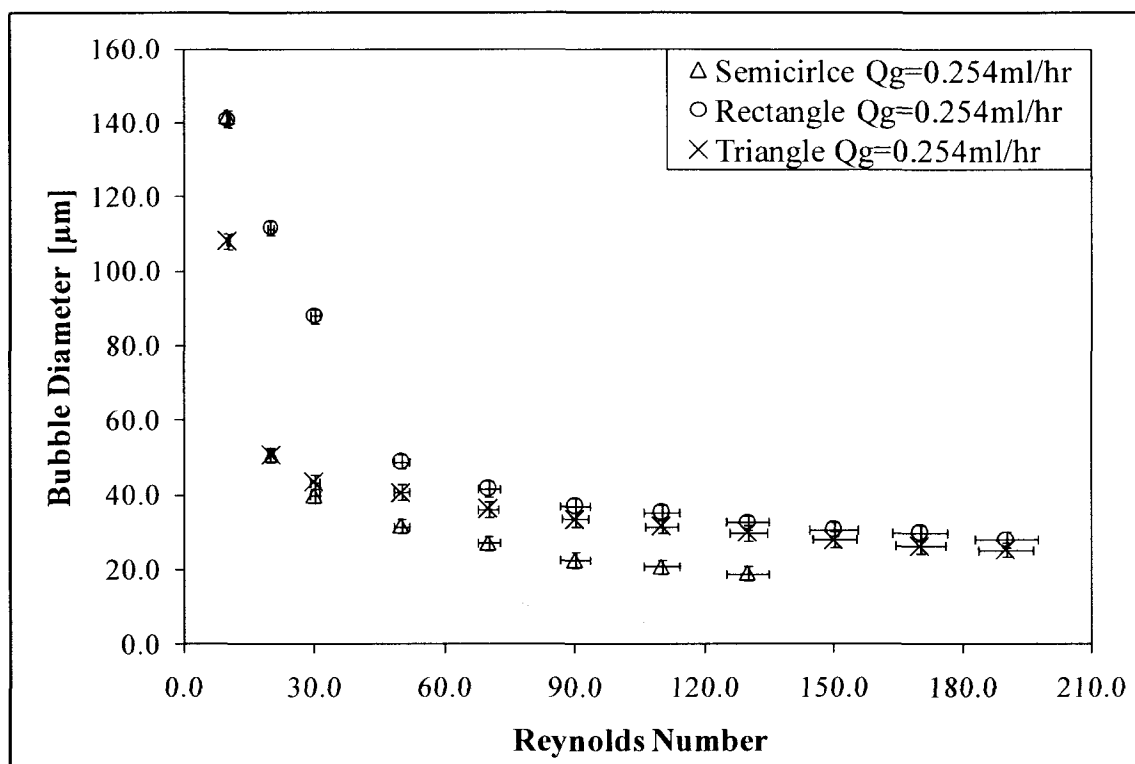


Figure 6.28 Plot gives the comparison between bubble diameters formed in cross-flow devices with three different shaped flow focusing structures (base channel  $160\mu\text{m}$ , secondary channel  $10\mu\text{m}$ , flow focusing structure height  $100\mu\text{m}$ )

Figure 6.29 represents the flow pattern in front of the orifice while using three different shapes of flow focusing structures inside the base channel. The orifice of bubble formation will be situated on the wall of the base channel opposite to the flow focusing structures towards the center of the structure. It can be observed from Figure 6.29 that as the flow focusing structure is introduced inside the base channel, the maximum velocity in the channel is shifted towards the side wall having the orifice, as expected. It can be noted that, while using a rectangular structure, the velocity vectors are parallel to the side wall of the base channel, creating an effect of using a narrow base channel for bubble generation. In the case of using the circular and triangle channels, the velocity vectors are

pointed on the orifice, creating an increase in the drag of the base liquid on the bubble formation.

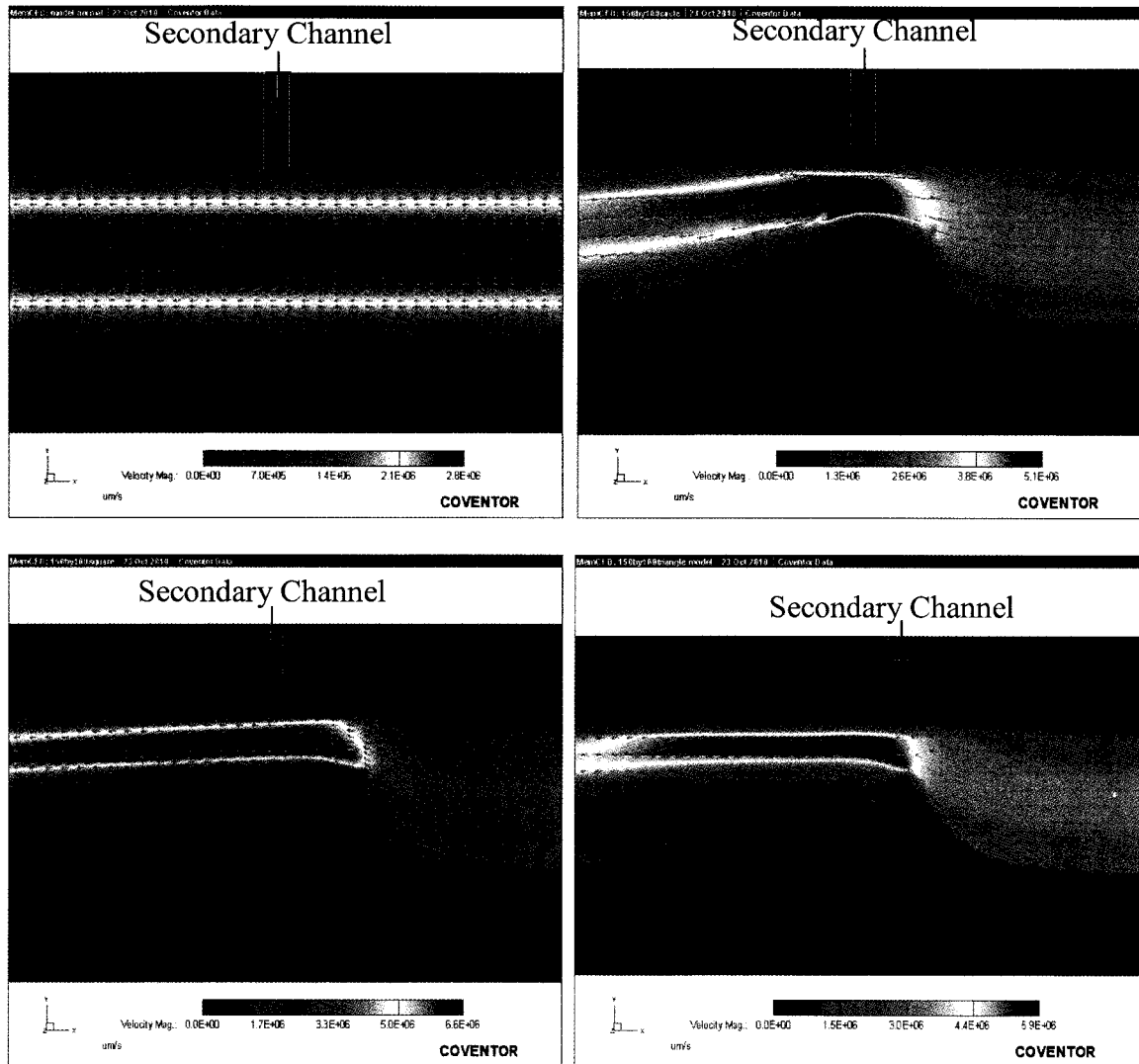


Figure 6.29 Contour plot of velocity profile in a base channel without flow focusing and with three different shapes of flow focusing structures (hydraulic diameter =  $150\mu\text{m}$ , flow focusing structure =  $100\mu\text{m}$ )

But while using the triangular structure, the focusing of the velocity vector is directed to the region slightly away from the orifice. This happens because the tip of the triangle is pointed towards the center of the orifice and causes the flow focusing to

happen slightly after the orifice in the flow direction. The semi-circular structure focuses the flow to the region just before the orifice, causing the formation of smallest bubble among the three flow focusing structures. The non-dimensional comparison of bubble formation at a higher gas flow rate inside the base channel using the three different flow focusing structures are done using non-dimensional volume of the bubbles formed in the base channel in Figure 6.30.

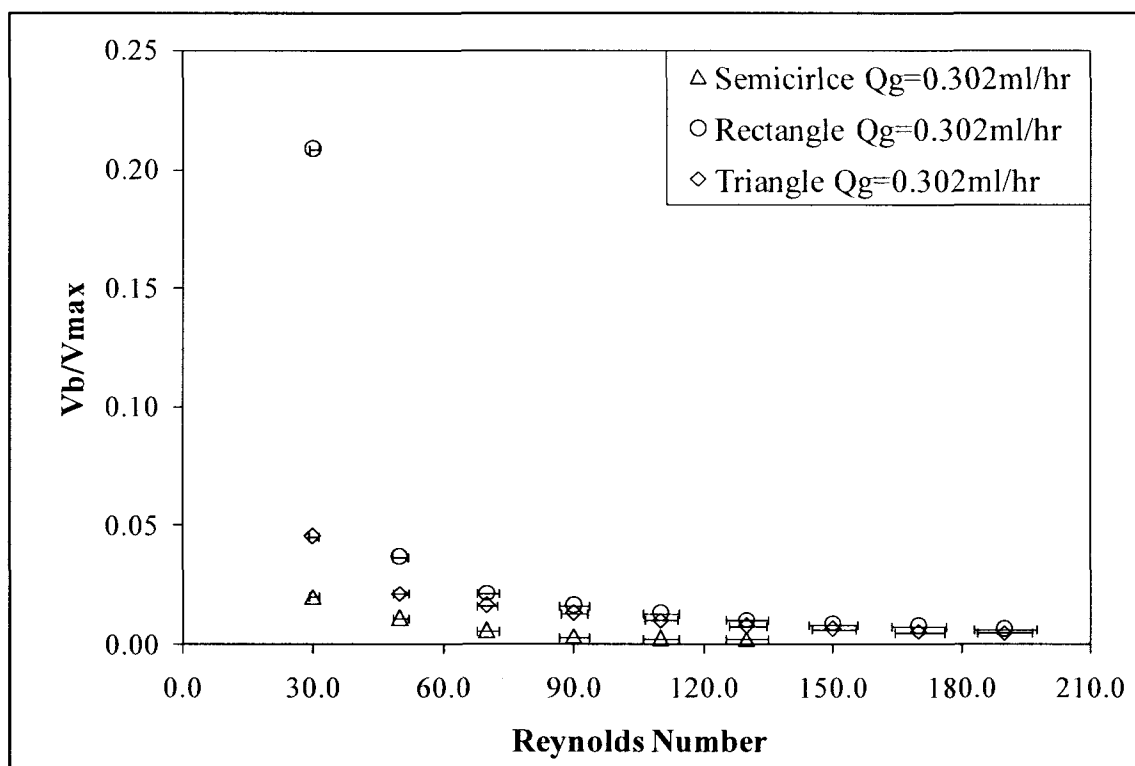


Figure 6.30 Comparison between the non-dimensionalized volume of bubbles formed in the cross-flow devices with three different shapes of flow focusing structures (base channel  $150\mu\text{m}$ , secondary channel  $10\mu\text{m}$ , flow focusing structure height  $100\mu\text{m}$ )

Here  $V_{max}$  is the volume of the biggest unconfined bubble that can be formed in the base channel without the flow focusing structure, and  $V_b$  is the volume of the bubble formed at each Reynolds number of liquid flow. The void fraction of microbubble

formation inside the base channel with different shapes of flow focusing structures is presented in Figures 6.31 through 6.33. The void fraction of bubble formation is plotted for six different gas flow rates through the secondary channel. Figure 6.31 represents the void fraction of bubble formation while embedding a semi-circular flow focusing structure inside the base channel. Figure 6.32 gives the void fraction of bubble formation inside a base channel with triangular flow focusing technique embedded inside it.

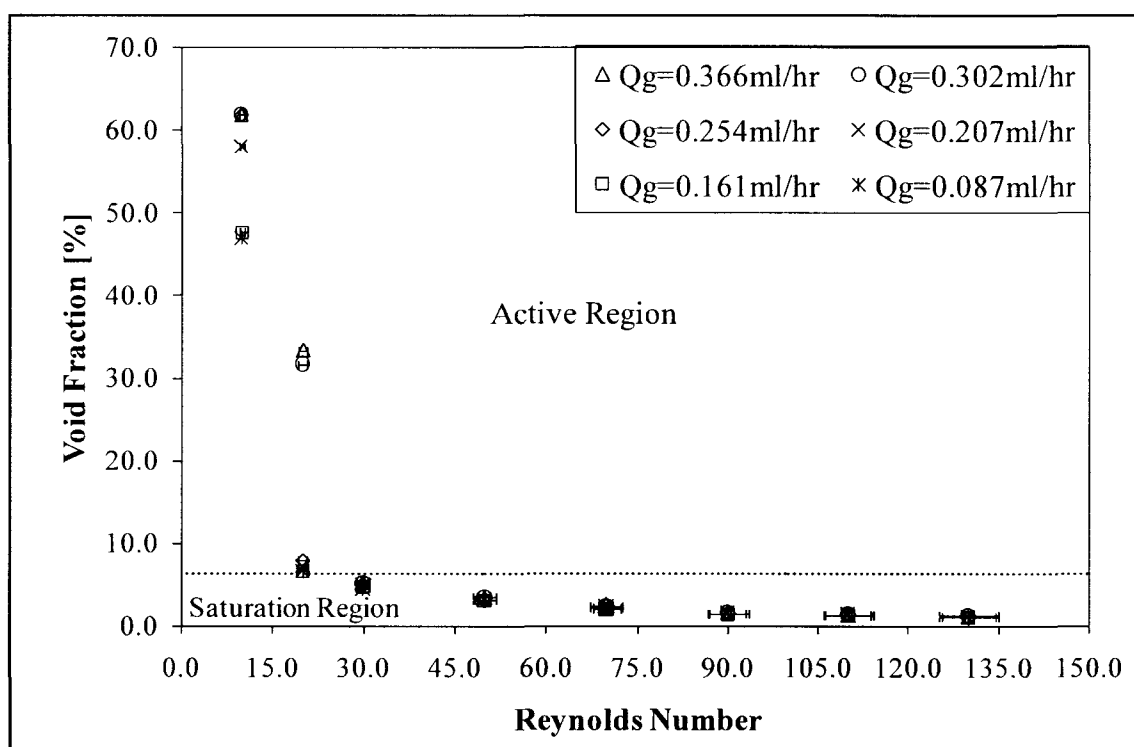


Figure 6.31 Plot gives the void fraction of bubble formation in base channel with semi-circle flow focusing structure at different magnitudes of Reynolds number (base channel  $160\mu\text{m}$ , secondary channel  $10\mu\text{m}$ , flow focusing structure height =  $100\mu\text{m}$ )

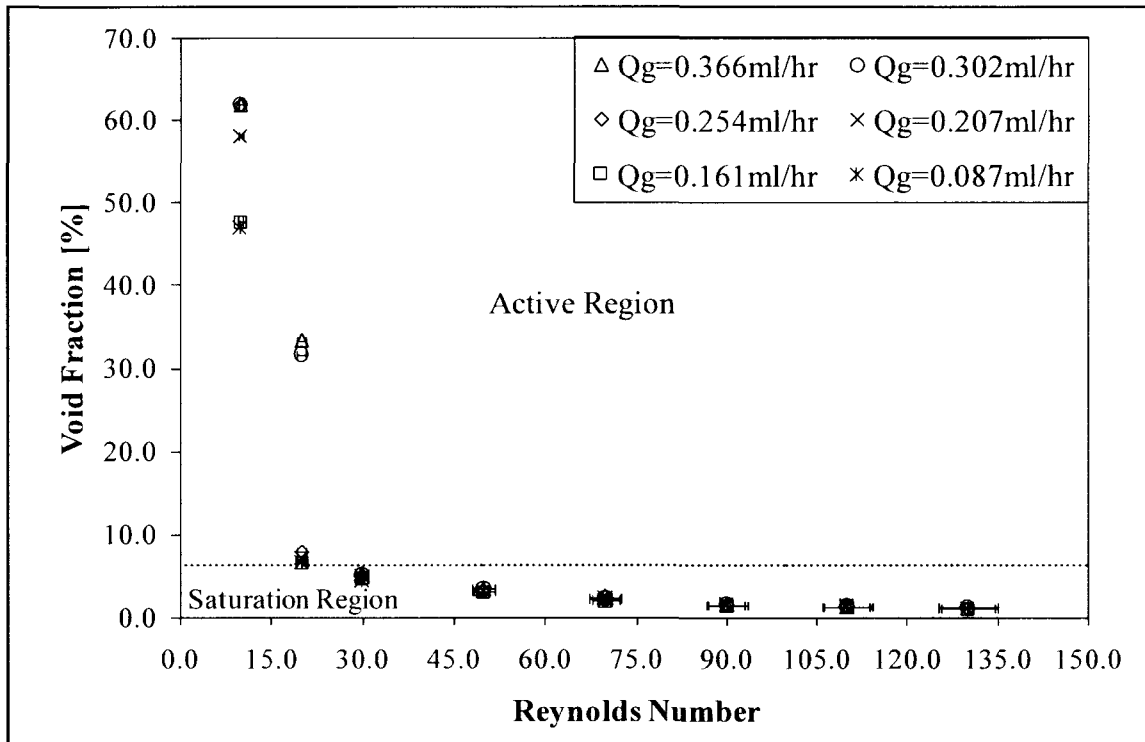


Figure 6.32 Plot gives the void fraction of bubble formation in base channel with triangle flow focusing structure at different magnitudes of Reynolds number (base channel  $160\mu\text{m}$ , secondary channel  $10\mu\text{m}$ , flow focusing structure height =  $100\mu\text{m}$ )

It can be observed from the Figures 6.31 and 6.32 that the void fraction of bubble formation does not change much with the change in the gas flow rate. A slight variation in the void fraction is observed at very low values of Reynolds numbers, but as the magnitude of Reynolds number increases the void fraction stays close to one another for different gas flow rates. Same observation was made in the plot of the void fraction without flow focusing techniques.

Another point to be noted from Figure 6.31 is the regions under which the bubble formation takes place. Even at very low magnitudes of Reynolds numbers, the bubble formation is limited to the active region. The bubble formation shifts to the saturation region as the Reynolds number reaches around 30. While using a secondary channel of

diameter  $10\mu\text{m}$ , the transition from the active to saturation region took place at a Reynolds number of around 120 for a base channel of same dimension that did not utilize the flow focusing technique. This once again proves the advantage of introducing the flow focusing technique inside the base channel of a cross-flow bubble generation device.

As in the previous case, the bubble formation is confined to the active and the saturation region, but the variation in the void fraction with change in the gas flow rate is more obvious in this case. At very low values of the gas flow rate, the bubble formation is limited to the saturation region. The reason behind the increase in the variation in void fraction can be turned back onto the flow pattern around the orifice discussed in Figure 6.29. The transition of the bubble formation region from the active to saturation region occurs at a higher Reynolds number around 60. Figure 6.33 represents the void fraction of bubble formation while using a rectangular flow focusing device. The variation in the void fraction at low magnitudes of Reynolds numbers is less compared to the last case while using a triangular flow focusing structure. The bubble formation is confined to the active and saturation regions, and the transition from the active region to saturation region occurs at a Reynolds number around 70 and is slightly higher than for the triangular flow focusing structure.



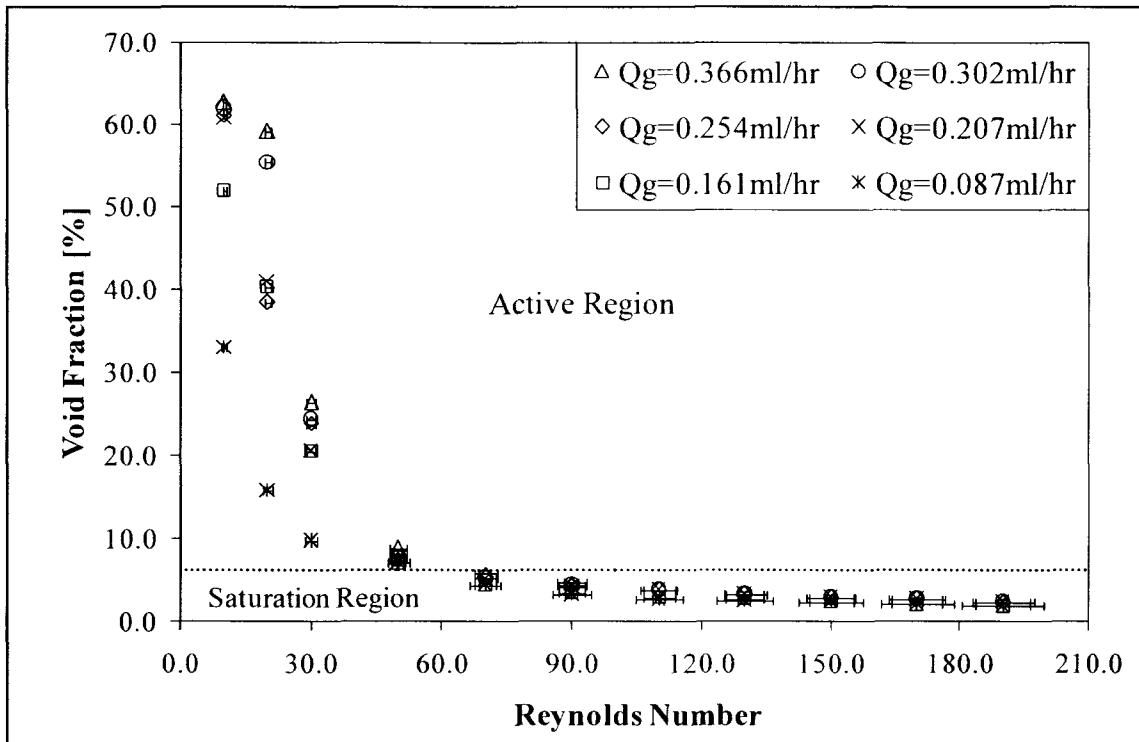


Figure 6.33 Plot gives the void fraction of bubble formation in base channel with rectangle flow focusing structure at different magnitudes of Reynolds number (base channel  $160\mu\text{m}$ , secondary channel  $10\mu\text{m}$ , flow focusing structure height =  $100\mu\text{m}$ )

#### 6.2.4 Case 4: Comparison of cross-flow device performance with different base length flow focusing structures

For the optimization purpose of the flow focusing structures inside the base channel, the dimensions of the flow focusing structure are varied and their performance is studied in this section. Varying the height of the flow focusing structure was studied in the feasibility study done using the CFD software [45]. The results showed that as the height of the flow focusing structure inside the base channel is increased (in other words, the cross-sectional area available for bubble formation in front of the orifice is decreased), the diameter of the bubbles formed from the orifice decreases. So, in this experimental study, instead of varying the height of the flow focusing structure, the width at the base of the flow focusing structures is varied to see its effect on the bubble

formation from the orifice. Figure 6.34 gives the mask used for manufacturing focus flow structures of base length 300 inside the base channel.

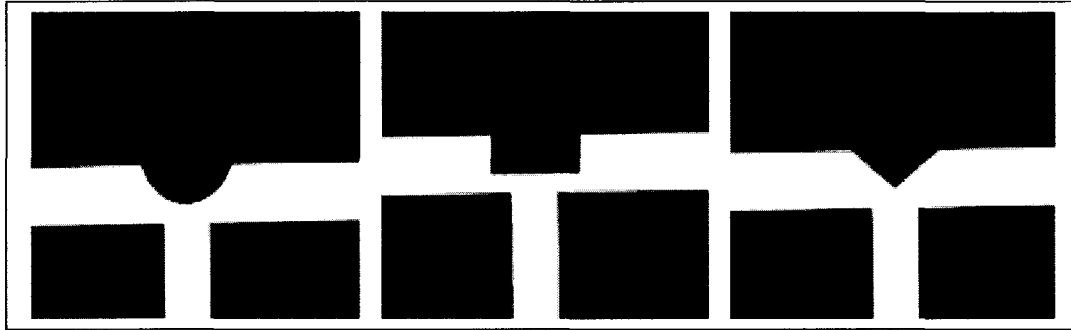


Figure 6.34 Mask used for the manufacturing of different shapes of flow focusing structures with base length  $300\mu\text{m}$ . (base channel  $150\mu\text{m}$ , flow focusing structure height  $100\mu\text{m}$ )

Figure 6.35 gives the comparison plot of bubble diameter obtained by using a semi-circle flow focusing structure of two different base lengths inside the base channel. The semi-circle flow focusing structures used in the study have a base length of  $150\mu\text{m}$  and  $300\mu\text{m}$  and have a constant height of  $100\mu\text{m}$ . It can be observed from the figure that the diameter of the bubbles formed in the base channels with semi-circle flow focusing structures of base length  $300\mu\text{m}$  is higher than the ones with base length  $150\mu\text{m}$ . But at small magnitudes of Reynolds numbers below 20, the scenario is different. The semi-circle structure with  $300\mu\text{m}$  base length produces the smaller bubble. To explain this scenario, the flow pattern in front of the orifice while using both the structures has to be studied carefully.

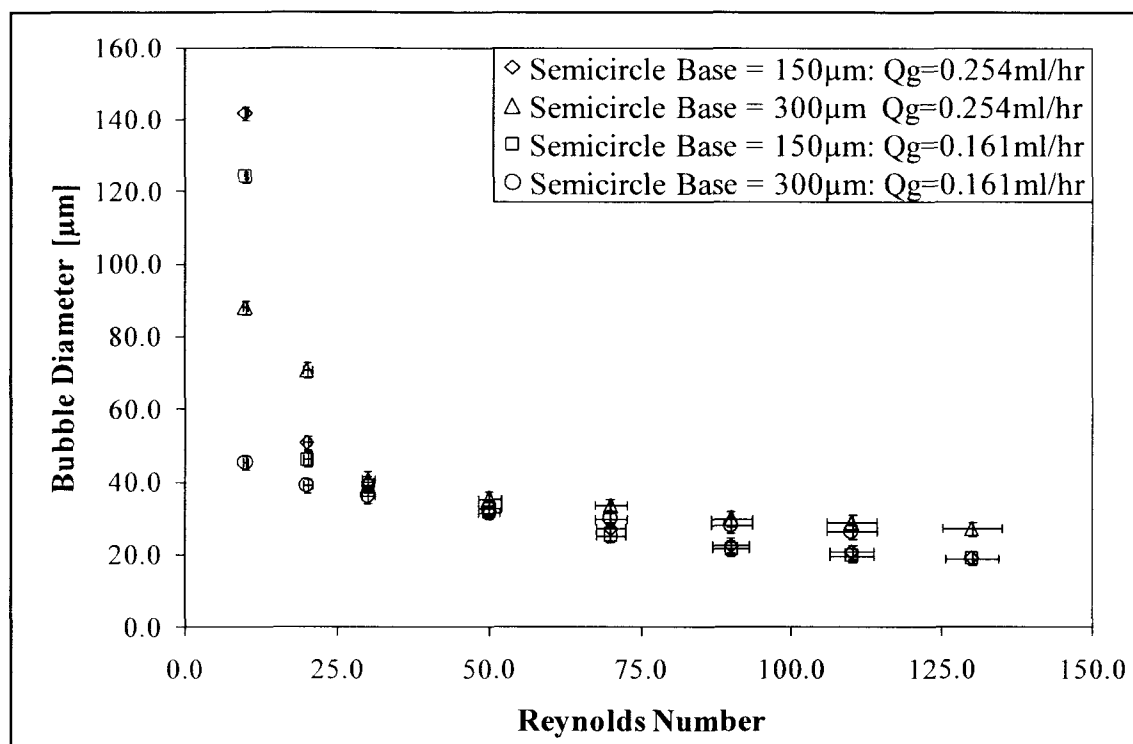


Figure 6.35 Plot represents the comparison between the bubble diameter formed in cross-flow device with flow focusing using semi-circle structures of two different base length (base channel  $160\mu\text{m}$ , secondary channel  $10\mu\text{m}$ , flow focusing structure height  $100\mu\text{m}$ )

Figure 6.36 gives the contour plot of velocity pattern for flow focusing structures of different base lengths. From Figure 6.36 it can be observed that as the base length of the flow focusing structures increases, the velocity profile in the region in front of the orifice tends to become parallel to the side wall of the base channel. It was stated earlier that the diameter of bubbles formed in the base channel with flow focusing depends on the focusing of base liquid velocity into the orifice of bubble formation. So while using the semi-circle with a longer base length, the velocity profile in front of the orifice becomes parallel to the side wall as it approaches the beginning of the orifice in the flow direction, causing the formation of bigger bubbles.

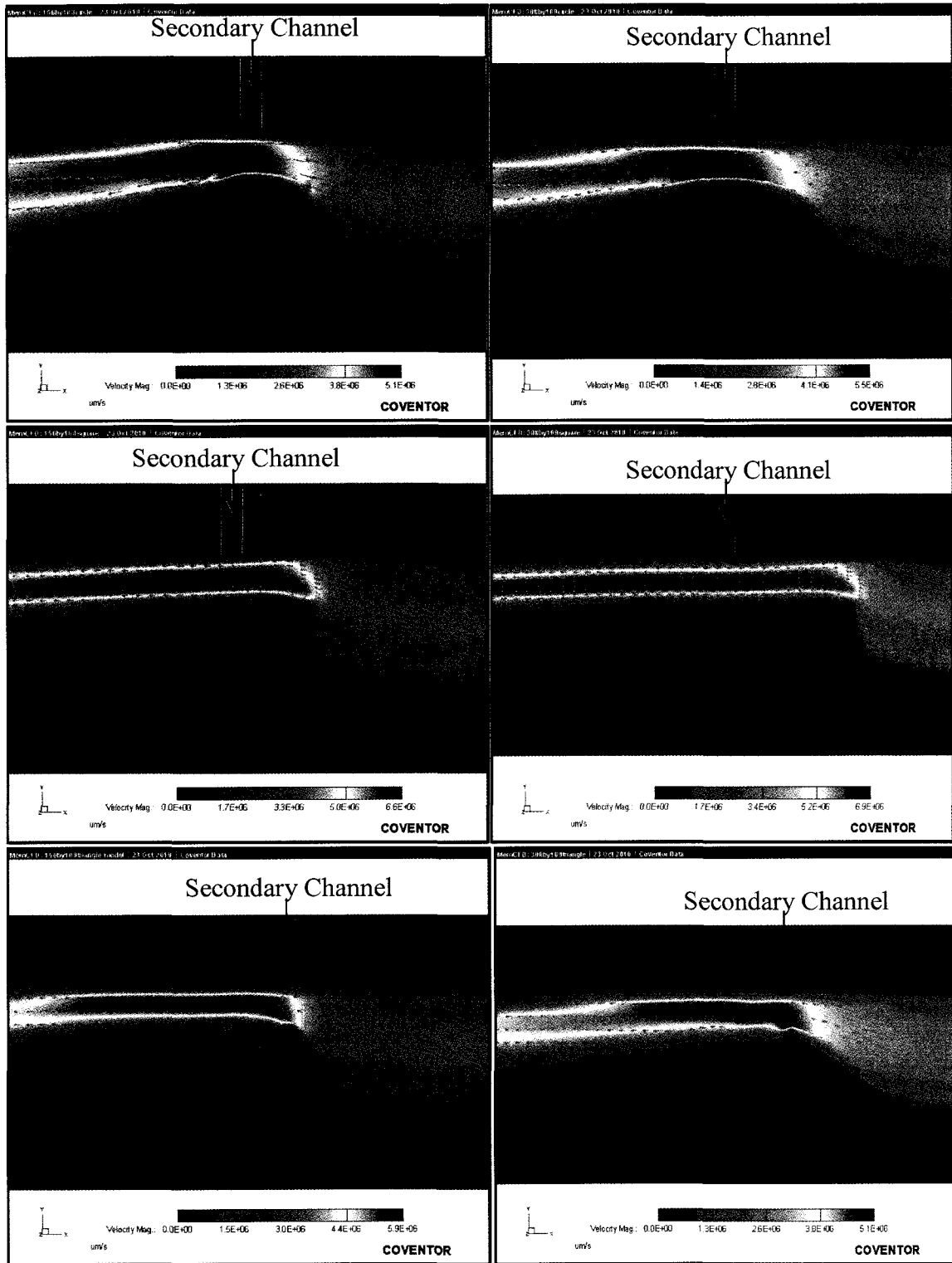


Figure 6.36 Contour plot of velocity profile in a base channel with flow focusing structures of different base length (hydraulic diameter =  $150\mu\text{m}$ , flow focusing structure =  $100\mu\text{m}$ )

The opposite happening at very low Reynolds number is due to the bubbles getting stuck to the semi-circle structure with a smaller base length. In all the contour plots shown in Figure 6.36, the orifice of bubble formation is placed on the opposite side wall of the base channel towards the center of the flow focusing structure. Figure 6.37 represents the comparison between bubble diameters formed by using rectangular channels of two different base lengths.

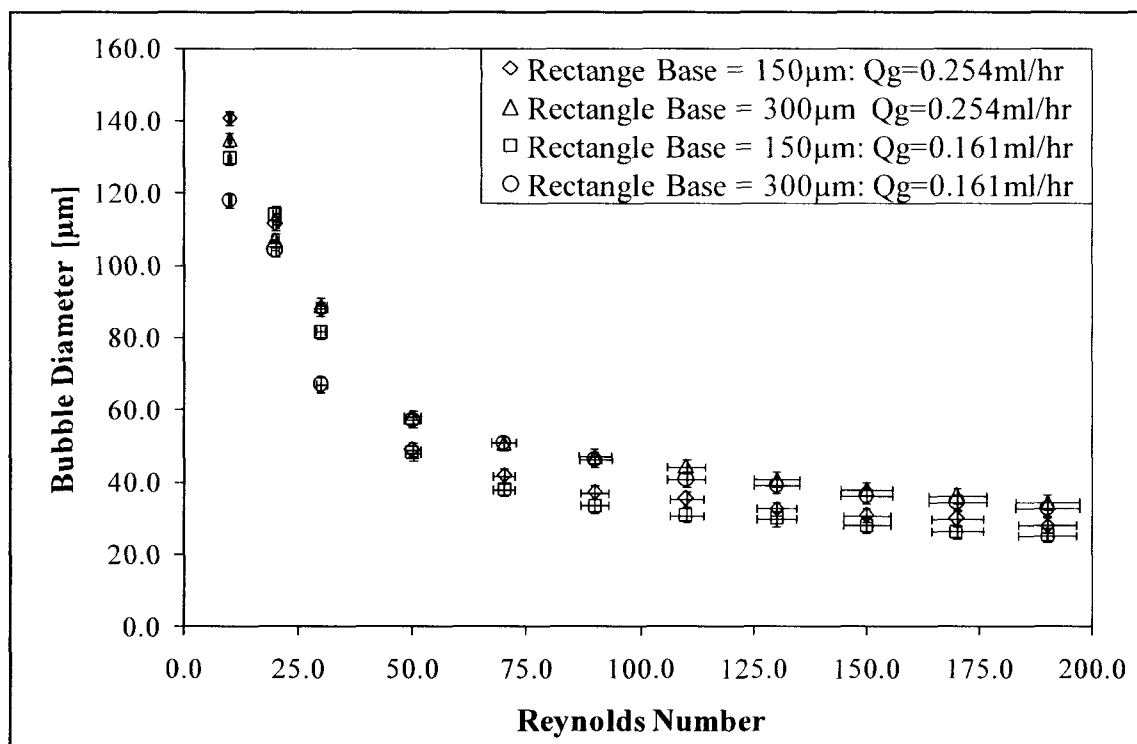


Figure 6.37 Plot gives the comparison between the bubble diameter formed in cross-flow device with flow focusing using rectangular structures of two different base length (base channel 160 μm, secondary channel 10 μm, flow focusing structure height 100 μm)

As in the case of using a semi-circular structure, the bubble diameter increases as the base length of the rectangular structure increases. The rectangular flow focusing structures have a poor performance compared to the other two structures due to the

velocity profile parallel to the side wall of the base channel in front of the orifice. This effect increases as the length of the rectangular structure increases and results in an even worse performance. Figure 6.38 gives the comparison of the bubble diameter while using two triangular structures of two different base lengths.

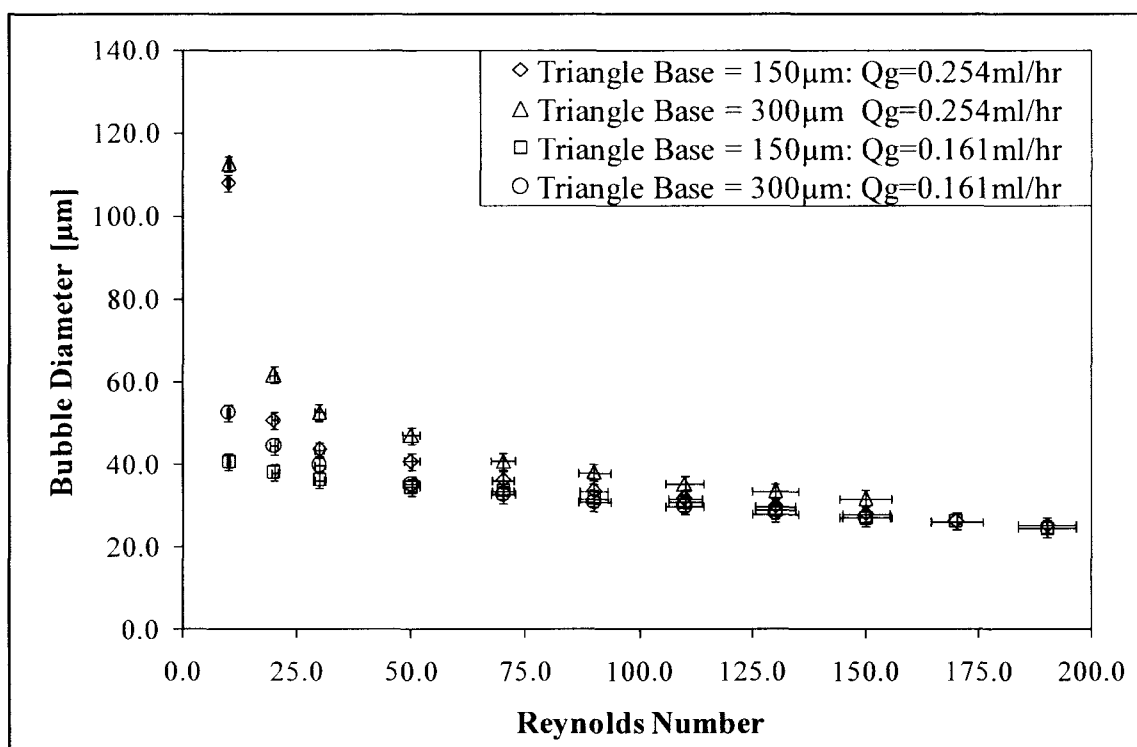


Figure 6.38 Plot gives the comparison between the bubble diameter formed in cross-flow device with flow focusing using triangular structures of two different base length (base channel  $160\mu\text{m}$ , secondary channel  $10\mu\text{m}$ , flow focusing structure height  $100\mu\text{m}$ )

It can be observed from Figure 6.38 that bubble diameter does not increase much with the increase in the base length of the flow focusing structures as in the previous two cases (while using circular and the rectangular structures). This phenomenon can be explained using the statement made about the focusing of liquid velocity onto the rear end of the orifice in the flow direction due to the tip of the triangle placed towards the

center of the orifice. It can be inferred from these observations that if the tip of the triangular flow focusing structure is positioned to the front end of the orifice in the liquid flow direction, bubbles of a smaller diameter can be obtained by using a triangular flow focusing structure.

As discussed at the end of Section 6.1, the objective of this project was to generate bubbles of a diameter less than  $15\mu\text{m}$ . The objective was achieved by generating bubbles of a size around  $11\mu\text{m}$  using a secondary channel of size  $2\mu\text{m}$  in a base channel of hydraulic diameter  $160\mu\text{m}$ . The objective to using the flow focusing technique inside the cross-flow bubble generators was to produce bubbles of a smaller size by using flow focusing techniques. The study was able to produce bubbles of a size around  $16\mu\text{m}$  and  $19\mu\text{m}$  with a secondary channel of size  $5\mu\text{m}$  and  $10\mu\text{m}$ , respectively in a base channel of  $160\mu\text{m}$  hydraulic diameters with semi-circle flow focusing structure of height  $100\mu\text{m}$ . The study was further extended to produce smaller bubbles and was successful in producing bubbles of a size around  $5\mu\text{m}$  with a secondary channel of  $2\mu\text{m}$  diameters in base channel of hydraulic diameter  $160\mu\text{m}$  with semi-circle flow focusing structure of height  $100\mu\text{m}$ . The smallest bubble produced ( $5\mu\text{m}$ ) is smaller than a red blood cell, and has a volume of  $6.58\text{e-}17\text{ m}^3$ . These bubbles can pass through the filtration system of the human body without any trouble and can be used for the oxygenation of blood directly using microbubbles.

### **6.3 Co-Flow Bubble Generators**

The second type of bubble generators considered in this study is the co-flow bubble generators. The schematic representation of a co-flow generator is given in Figure 6.38. The manifolds on both sides of the main channel provide the inlets for the liquid,

and the direction of the liquid flow is represented using the arrows. Gas flows into the junction through the secondary channel aligned in the central channel. The tip of the fused silica tube is aligned to the intersection of the liquids (the cross junction shown in Figure 6.39).

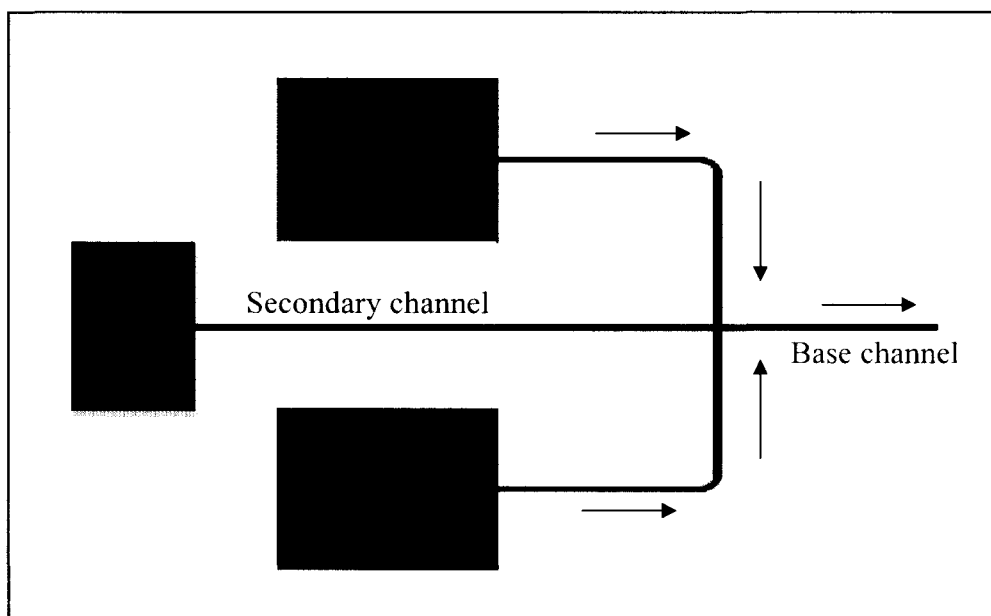


Figure 6.39 Schematic representation of the co-flow bubble generator

The liquids flow through the base channels, leaving the manifold and will merge into the main base channel. The gas flowing through the secondary channel will form bubbles in the junction, and the drag force exerted by the merging liquid will force the bubble to get detached from the orifice. Since the secondary channel diameter used in this device also falls under the slip flow region of gas flow, the same equations used in the cross-flow device to calculate the gas flow are used in this case also. Figure 6.40 represents the bubble formation in a co-flow device at various time steps.



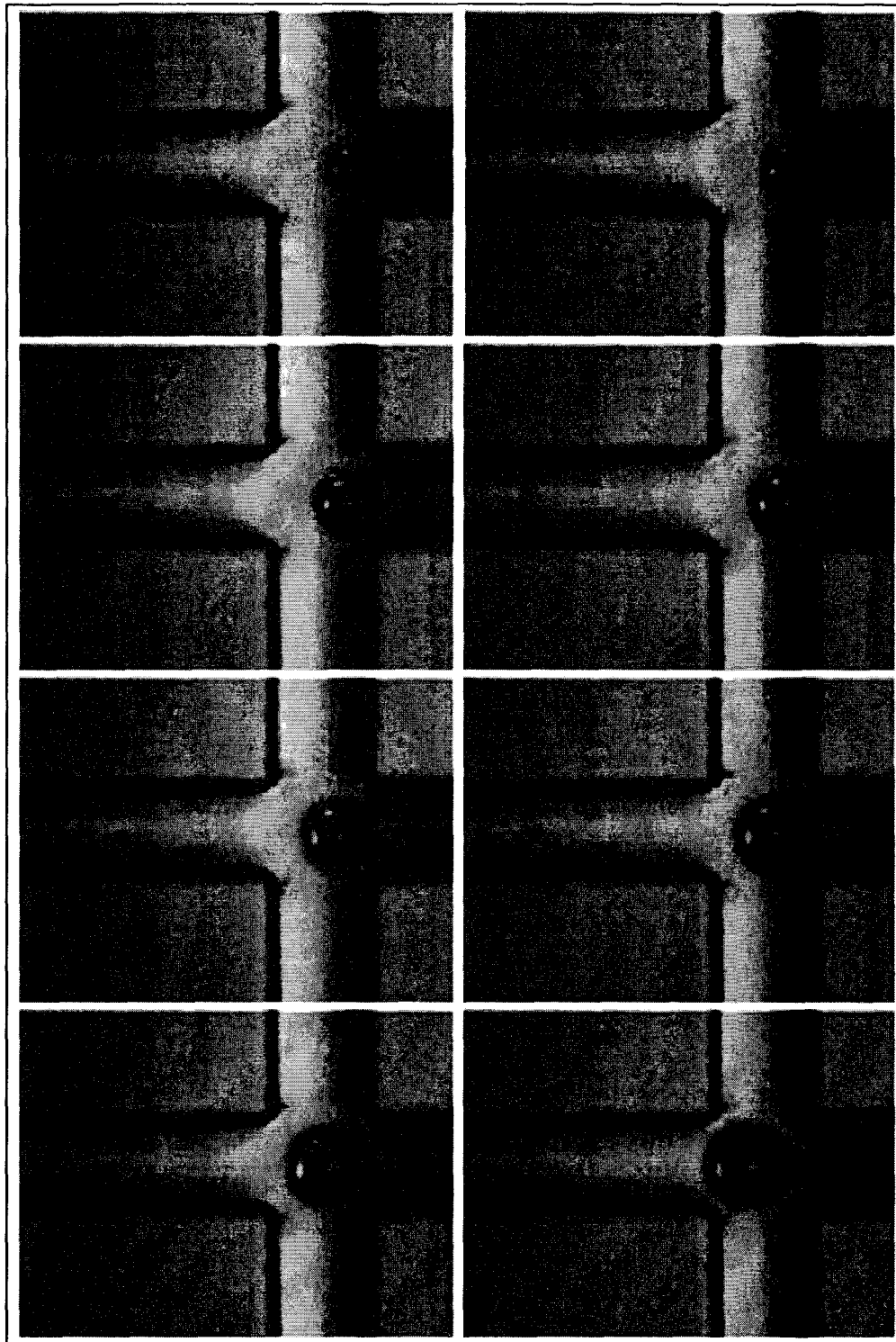


Figure 6.40 Represents the bubble formation inside a co-flow device with base liquid coming from both sides of the bubble and forcing the bubble to detach from the orifice ((base channel  $150\mu\text{m}$ , secondary channel  $10\mu\text{m}$ )

The force balance equation used in the cross-flow device cannot be used to model the bubble formation in a co-flow device due to the formation of flow separation region in front of the orifice. The details of the formation of flow separation region are discussed in the Section 6.3.1. Figure 6.41 gives the comparison of the bubble diameter formed from a co-flow bubble generation device with the base channel of hydraulic diameter  $162\mu\text{m}$  and secondary channel of diameter  $10\mu\text{m}$  at six different flow rates of gas through the secondary channel.

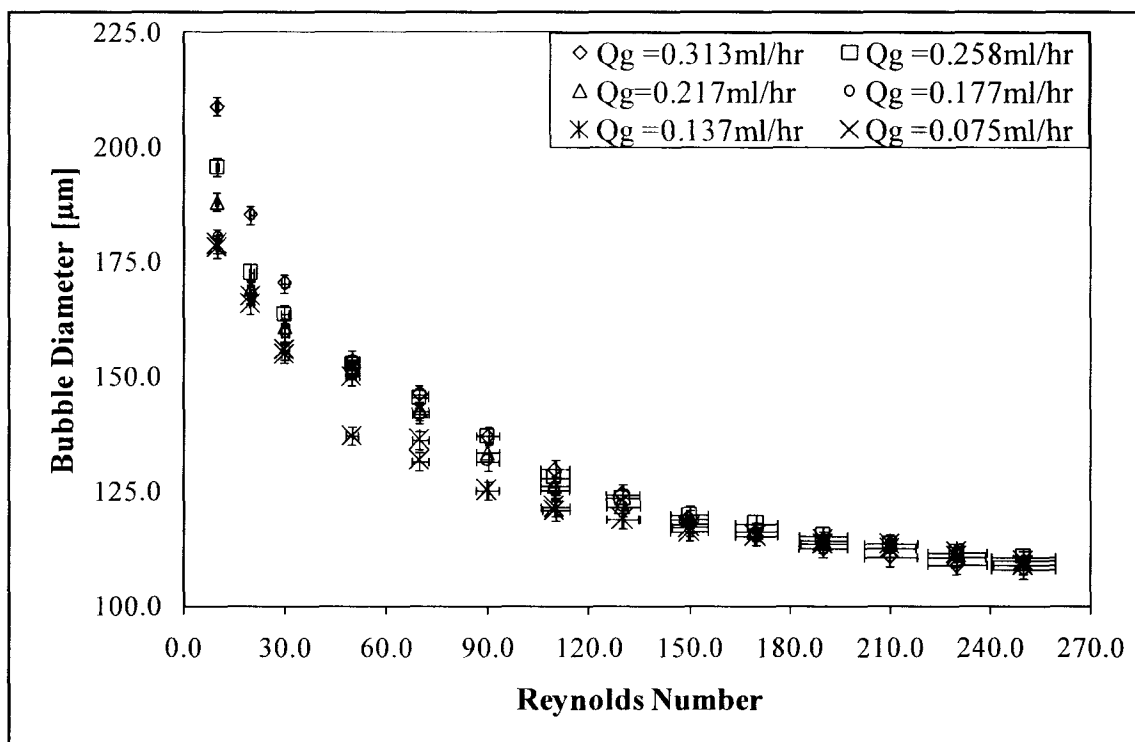


Figure 6.41 Plot gives the variation in bubble diameter generated in a co-flow device for six different values of gas momentum at various magnitudes of base liquid Reynolds numbers (base channel  $162\mu\text{m}$ , secondary channel  $10\mu\text{m}$ )

The base channels connecting the manifolds to the bubble formation junction has the same hydraulic diameter as the main base channel, so the flow rate corresponding to

each Reynolds number of liquid flow though the main base channel is divided into two parts. Each portion is fed into a manifold on either side of the secondary channel. It can be noted from Figure 6.41 that the bubble diameter corresponding to high Reynolds number such as 250 is much larger compared to the bubble diameter in cross-flow device with same dimensions of base and secondary channel. And even while using a secondary channel of a diameter as small as  $10\mu\text{m}$ , a major portion of the bubbles formed in the co-flow device is confined to the base channel walls. This happens due to the formation of a flow separation region in front of the orifice where the flow of the base liquid forms a flow separation region. This scenario can be explained better by using a flow pattern study done using CFD software CoventorWare. Figure 6.42 gives the contour plot and vector plot of velocity profile in front of the orifice inside a co-flow bubble generation device.

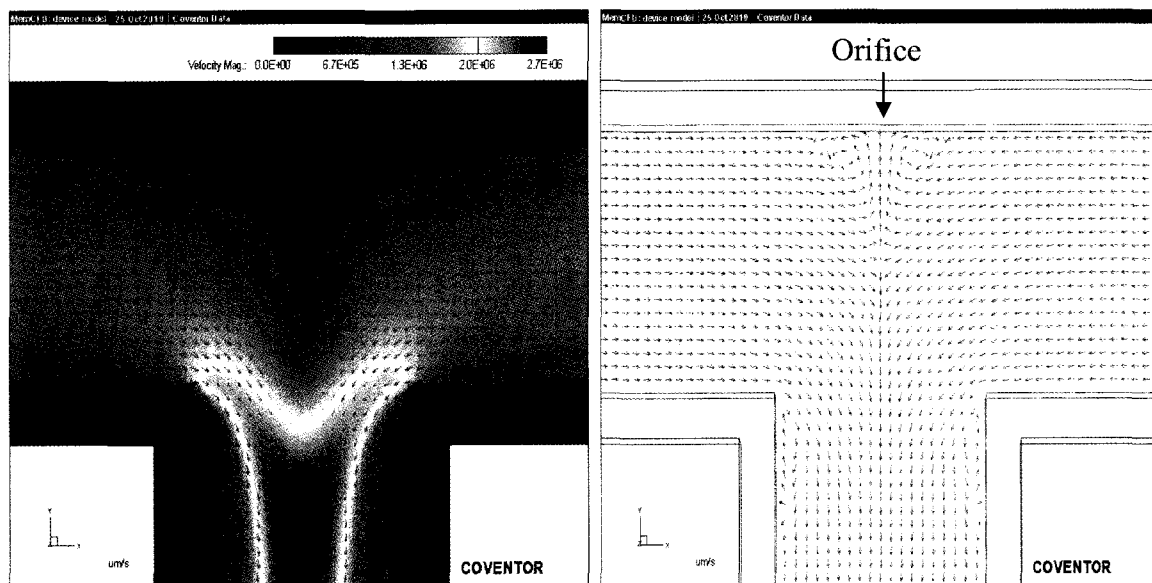


Figure 6.42 Contour plot and vector plot of velocity profile in front of the orifice in a co-flow device (bases channel  $150\mu\text{m}$ , Reynolds number 250)

It can be observed from the contour plot of velocity profile represented in Figure 6.42 that in the region around the orifice (that occurs to be on the center of the wall opposite to the main channel) the flow of the base liquid is almost zero. The vector plot of the same velocity profile shows a flow separation in the region. This phenomenon is the reason behind the formation of a bigger bubble inside the co-flow device compared to the cross-flow device. The formation of this flow separation region prevents the use of force balancing equation for predicting the diameter of the bubble formed from a co-flow bubble generation device. The size of the flow separation region changes with the Reynolds number of the liquid flow through the base channel. Mathematical equations of higher complexities have to be employed for the determination of the size of the flow separation region. CoventorWare<sup>®</sup> CFD module uses the solution obtained from solving the three dimensional momentum and continuity equations in determining the flow separation region at a different flow rate of liquid flow.

In the case of the co-flow devices, the transition of bubble formation from the active region to the saturation region depends on the size of the flow separation region in front of the orifice. Different from the case of the cross-flow device, the determination of a general equation for determining the saturation region for each device is not possible for the co-flow device, as the size of the flow separation region depends on the Reynolds number of base fluid flow. As the Reynolds number of liquid flow through the base channel increases, the size of the flow separation region also increases but at the same time an increase in Reynolds number will result in a decrease in the bubble diameter at which it detaches from the orifice. This happens because of the increase in drag force of the base liquid with the increase in Reynolds number. So as the Reynolds number

increases a balance situation will occur where the diameter of the bubble detachment equals the size of the flow separation region, and the transition from the active region to the saturation region happens around that particular Reynolds number. Any further increase in the Reynolds number of liquid flow will not have much effect on the bubbles being detached from the orifice. Since in this study the determination of the size of the flow separation region is not possible for each of devices considered in this study, the void fraction of bubble formation is classified only as the confined region and active region. The new generation of co-flow devices presented in this study has a far better performance than the conventional co-flow devices using both a base and secondary channel of same depth. From Figure 6.40 it can be noted that the bubble formed from a co-flow device, having a secondary channel of  $10\mu\text{m}$  in diameter, is having a perfect spherical shape throughout its formation, and has the base fluid flowing all around it once the bubble becomes bigger than the flow separation region in front of the orifice. Figure 6.43 gives the plot of superficial velocity of the bubble corresponding to each value of superficial velocity of base liquid. The graph is plotted for three different flow rates of gas through the secondary channel and it can be seen that the superficial velocity of gas is much less in magnitude than the corresponding superficial velocity of the liquid. Even at a high magnitude of pressure drop across the secondary channel, the bubble formation from the new generation co-flow device falls under the bubbly region. The parametric study of the co-flow bubble generation device is limited to three different cases. The first case studies the variation in the void fraction of bubble formation for different Reynolds number of base liquid flow at six different gas flow rates through the secondary channel. The second case studies the variation in the void fraction of bubble formation while using

secondary channels of different hydraulic diameters. The third case studies the effect of void fraction of bubble formation while using different base liquids.

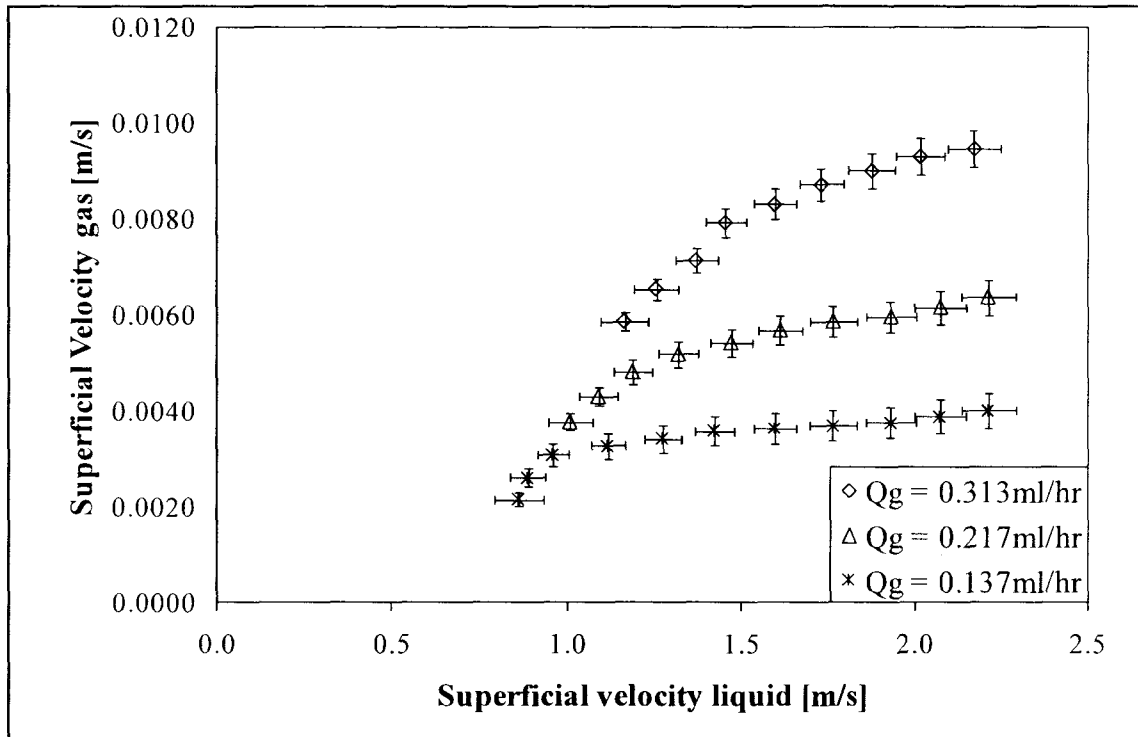


Figure 6.43 Plot gives the variation in superficial velocity of gas with respect to the change in superficial velocity of the base liquid in a co-flow device (base channel 160 $\mu$ m, secondary channel 10 $\mu$ m)

### 6.3.1 Case 1: Variable parameter: Reynolds number of base liquid flow and gas flow rate

Figure 6.44 represents the variation in the void fraction of bubble formation in a co-flow bubble generation device for various Reynolds numbers of liquid flow rates at six different gas flow rates. It can be observed from the figure that as the Reynolds number of liquid flow rate increases, the void fraction of bubble formation decreases. The variation in the void fraction of bubble formation with the increase in the gas flow rate occurs at low Reynolds numbers of liquid flow rate, but as the Reynolds number

increases, the void fraction for various gas flow rates tends to come closer. As explained in the Sections 6.1 of cross-flow devices, the pressure drop inside the base channel is low at low Reynolds numbers of liquid flow, so the variation in the absolute pressure in front of the orifice will have an effect on the bubble formation. However as the pressure drop across the base channel increases with the increase in liquid flow Reynolds number, this effect will become negligible, and the void fraction of bubble formation comes close to one another. The transition from the confined region to the saturation region occurs around a Reynolds number of 50. As discussed in the Section 6.3, determination of the saturation region is difficult to attain and so is not defined in Figure 6.44.

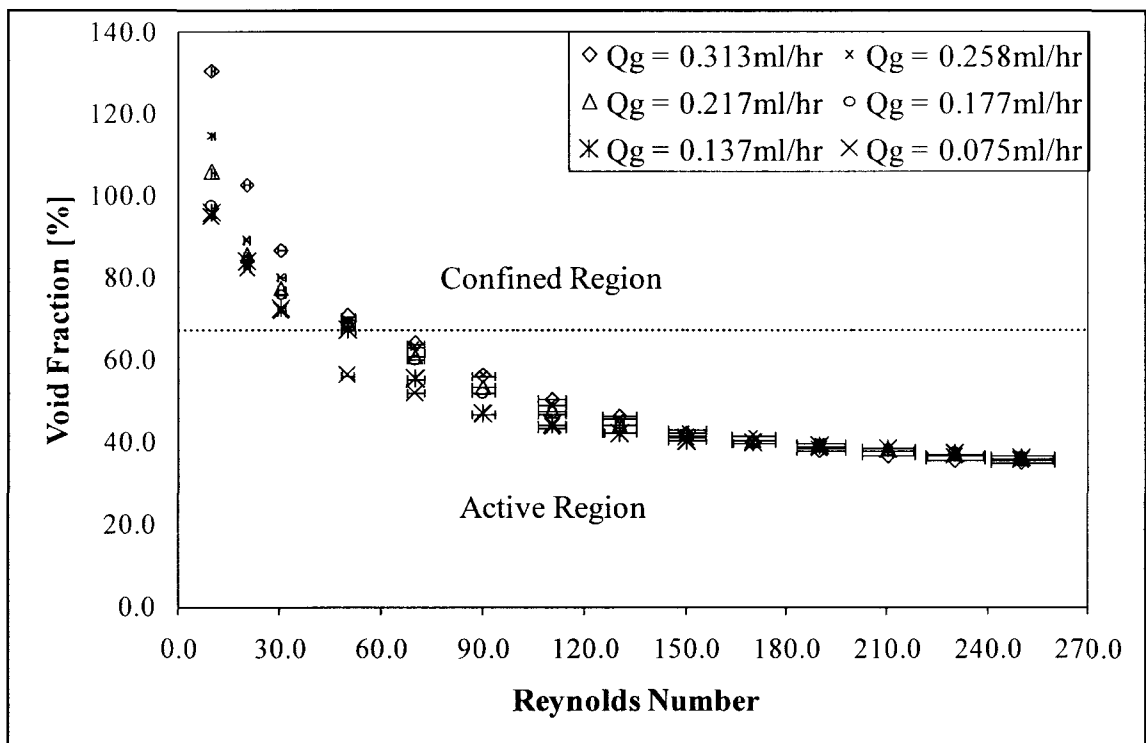


Figure 6.44 Plot gives the variation in void fraction inside a co-flow device for five different values of gas flow rate at various magnitudes of Reynolds numbers of base liquid flow (base channel  $162\mu\text{m}$ , secondary channel  $10\mu\text{m}$ )

### 6.3.2 Case 2: Variable parameter: Hydraulic diameter of secondary channel

This section deals with the change in void fraction of the bubble diameter with the change in the hydraulic diameter of the secondary channel. Figure 6.45 represents the void fraction of bubble formation in a co-flow device for five different gas flow rates through a secondary channel of hydraulic diameter  $5\mu\text{m}$ . It can be observed from the figure that most of the bubble formation falls under the active region, even at a very small Reynolds number of liquid flow through the base channel. The transition from the confined to the active region occurs at a Reynolds number of around 20. The variation of void fraction with the change in the gas flow rate is very minimal in the active region.

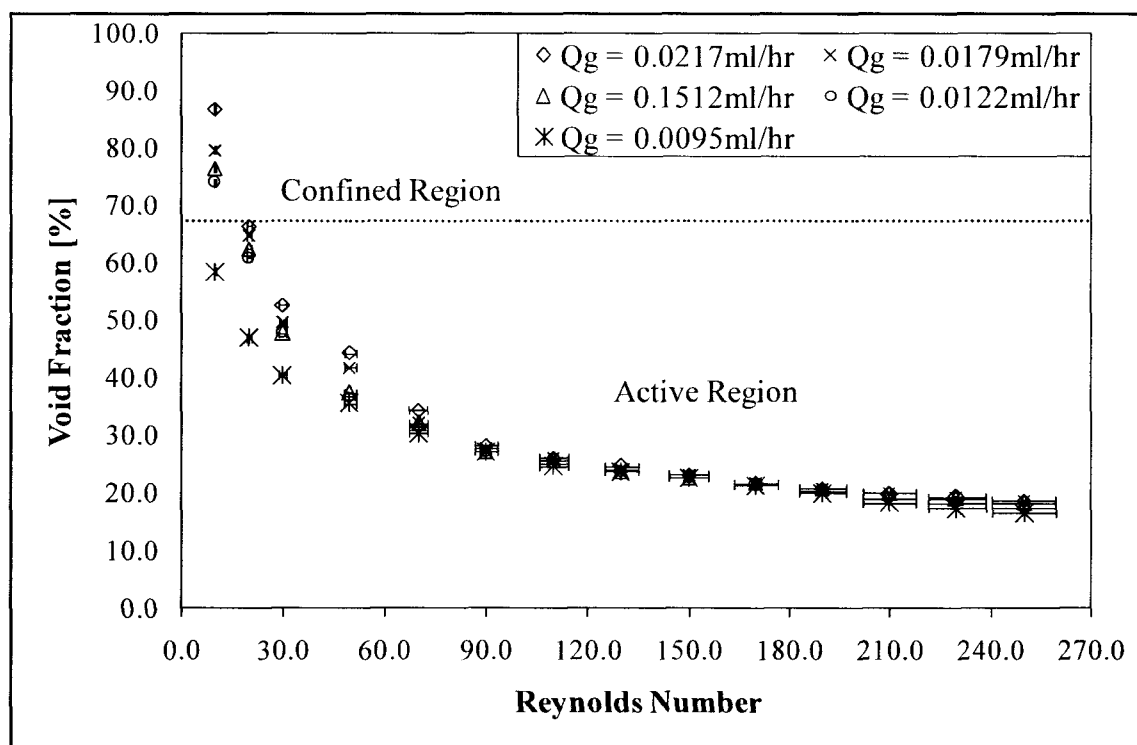


Figure 6.45 Plot gives the variation in void fraction inside a co-flow device for five different values of gas flow rate at various magnitudes of Reynolds numbers of base liquid flow (base channel  $162\mu\text{m}$ , secondary channel  $5\mu\text{m}$ )



As discussed previously in Chapter 6, the void fraction of bubble diameter varies a little at very low magnitudes of Reynolds number. The gas flow rate through the secondary channel is very low even at a very high pressure drop of gas flow across the channel because of its very small hydraulic diameter. This enables the generation of unconfined bubbles in the base channel under all conditions of gas flow rate through the secondary channel.

The void fraction of bubble formation in a cross-flow device while using a secondary channel of hydraulic diameter  $10\mu\text{m}$  is given in Figure 6.44. The trend shown by the void fraction of bubble formation by using a secondary channel of  $10\mu\text{m}$  while using six different gas flow rates is the same as that of using the secondary channel of hydraulic diameter  $5\mu\text{m}$ . The number of bubbles formed in the confined region at same pressure drop across the secondary channel increases as the size of secondary channel increases. The transition from the confined region to the active region happens at a Reynolds number of around 40. The variation in the void fraction of bubble formation with different flow rates of gas through the secondary channel is negligible at higher Reynolds numbers, but is noticeable at lower magnitudes of Reynolds numbers.

Figure 6.46 gives the variation in the void fraction of bubble diameter with four different gas flow rates through the secondary channel of hydraulic diameter  $25\mu\text{m}$ . It is interesting to note the variation in the void fraction of bubble diameter with the change in the gas flow rate at higher Reynolds number of liquid flow. As the hydraulic diameter of the secondary channel increases, the variation in the void fraction of bubble diameter also increases with the change in pressure drop of gas flow across the channel. The gas momentum force acting through the secondary channel becomes an influential force at

the large hydraulic diameter of secondary channels. The bubbles being formed from the secondary channel are large enough to be larger than the flow separation region right from the moment of its formation. The bubbles will reach a saturation region only at very high Reynolds number of liquid flow through the base channel. The same trend in the variation of void fraction of bubble diameter while using secondary channels of diameter  $25\mu\text{m}$  was observed in the previous case of the cross-flow device discussed in Section 6.1.3.

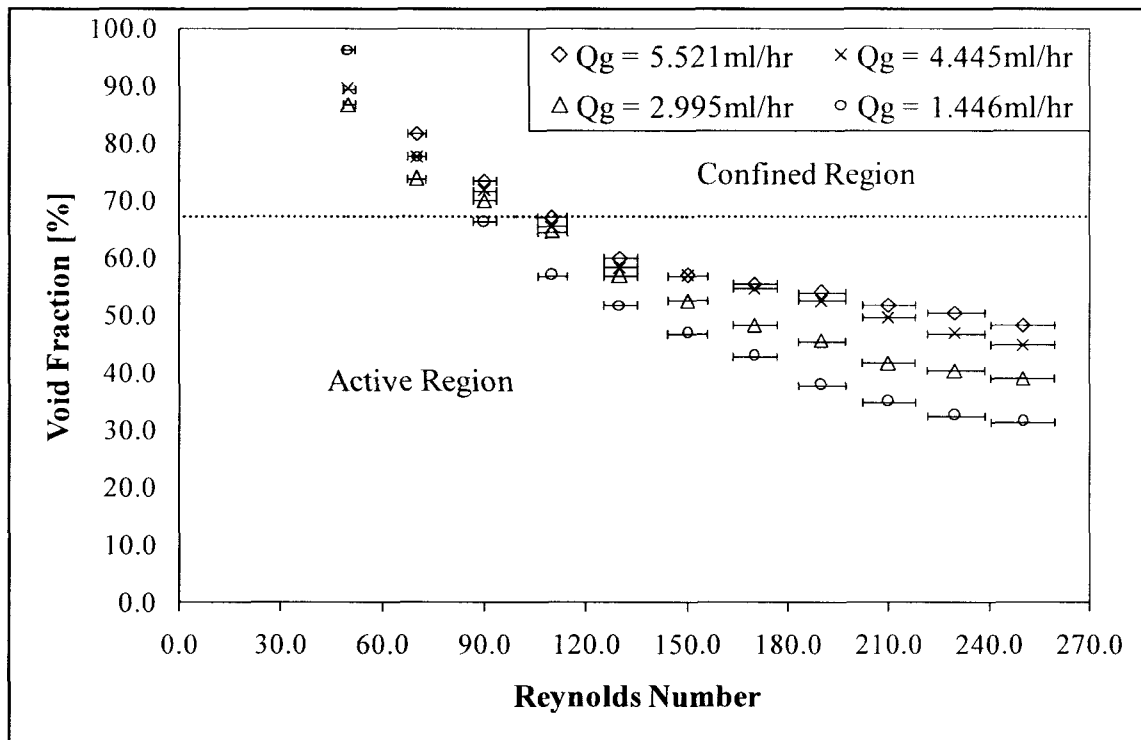


Figure 6.46 Plot gives the variation in void fraction inside a co-flow device for five different values of gas flow rate at various magnitudes of Reynolds numbers of base liquid flow (base channel  $162\mu\text{m}$ , secondary channel  $25\mu\text{m}$ )

Figure 6.47 represents the variation in the void fraction of bubble diameter with the variation in the gas flow rate through the secondary channel of hydraulic diameter  $50\mu\text{m}$  for three different gas flow rates.

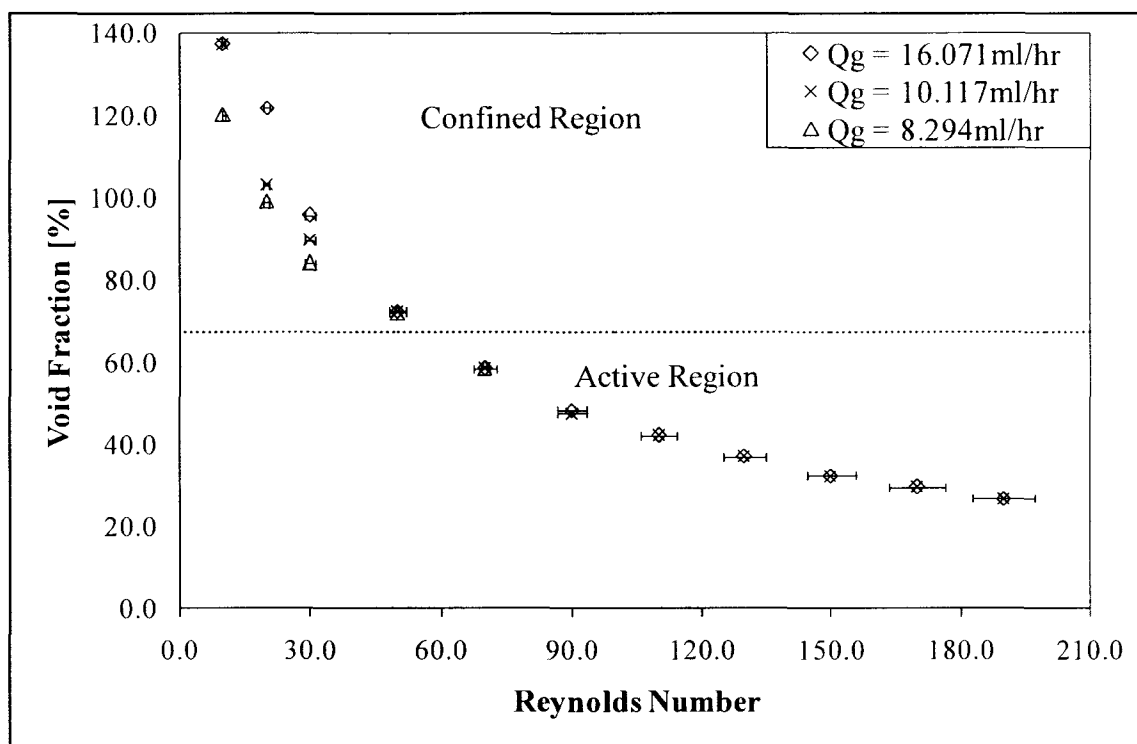


Figure 6.47 Plot gives the variation in void fraction inside a co-flow device for three different values of gas momentum at various magnitudes of base liquid flow Reynolds numbers (base channel  $162\mu\text{m}$ , secondary channel  $50\mu\text{m}$ )

The interesting thing that can be noted from Figure 6.47 is that even with a secondary channel of hydraulic diameter of  $50\mu\text{m}$ , the void fraction of the bubbles generated in the device at three different gas flow rates remains the same at high Reynolds number of liquid flow. This behavior was observed in the cross-flow device also while using a secondary channel of hydraulic diameter  $50\mu\text{m}$ . The reasoning behind this phenomenon can be explained using the pressure drop across the secondary channel.

Even though the gas flow rate through the secondary channel varies, the pressure drop across the secondary channel remains very close to each other during the bubble formation in the base channel (between 1.8 and 0.9 PSI). This causes the diameter of bubble formation to stay close to each other at high Reynolds numbers of liquid flow through the base channel (the change in the absolute pressure in front of the orifice is low compared to the pressure drop across the base channel at high Reynolds number of liquid flow).

### **6.3.3 Case 3: Variable parameter: Different base liquids**

The dependency of the void fraction of bubble diameter on the properties of the base liquid is studied in this section with the help of three different liquids of different physical properties that affect the Reynolds number of its flow through the base channel. As in the case of the cross-flow device, the combined effect of the density and dynamic viscosity of the base liquid on the bubble formation is studied using the kinematic viscosity of the base liquid. The variation of the void fraction of bubble diameter with change in the kinematic viscosity of three different base liquids is represented in Figure 6.48. It can be noticed from the figure that as the kinematic viscosity of the base liquid increases, the void fraction of bubble diameter decreases. Two liquids, Isopropanol and Ethylene glycol, have the same void fraction of bubble diameter at very low base liquid flow rate but show a clear variation at higher flow rates. Water, which is the third working liquid used in the study, shows a much higher void fraction of bubble formation compared to the void fraction obtained while using other two liquids. The liquid velocity is kept constant for all the liquids flowing through the base channel for the purpose of comparison in Figure 6.48. The drag force, which is a function of liquid viscosity, acts

much more effectively on the bubbles being formed from the orifice when the viscosity of the base liquid is higher. This causes the bubbles to get detached from the orifice at a smaller diameter while using a liquid of high viscosity as the base liquid.

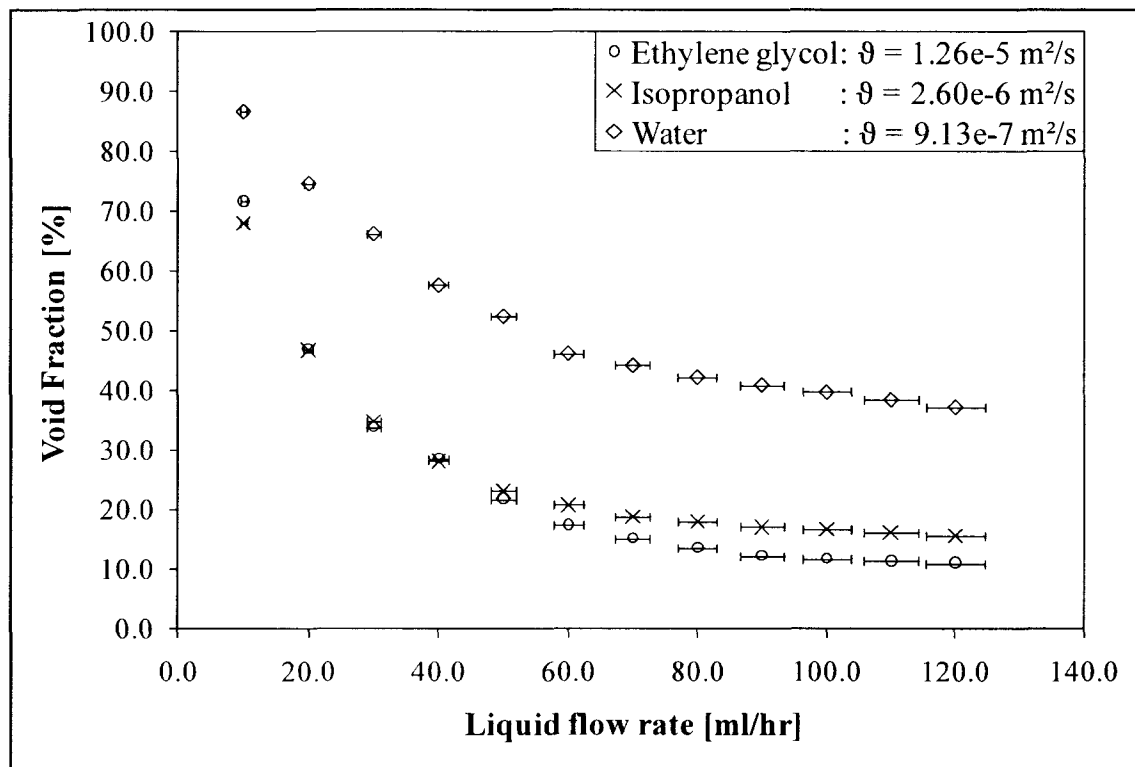


Figure 6.48 Plot gives the void fraction of bubble formation in co-flow device for base liquids with different kinematic viscosities (base channel  $162\mu\text{m}$ , secondary channel  $10\mu\text{m}$ , Gas flow rate  $0.187\text{ml/hr}$ )

In order to validate the trend shown by the void fraction of bubble formation in Figure 6.48 a second graph is plotted in Figure 6.49 with all the parameters in Figure 6.48, constant while varying the gas flow rates through the secondary channel. Figure 6.49 shows the same characteristics of Figure 6.48, except the fact that the void fraction of bubble diameter at low liquid flow rates shifted down slightly. The graph representing the void fraction of the bubble diameter with the change in Reynolds number of liquid

flow in base channel is not included in this study because it has the same trend as the graph with constant liquid flow rate. This was proven in Section 6.16 while considering the cross-flow device.

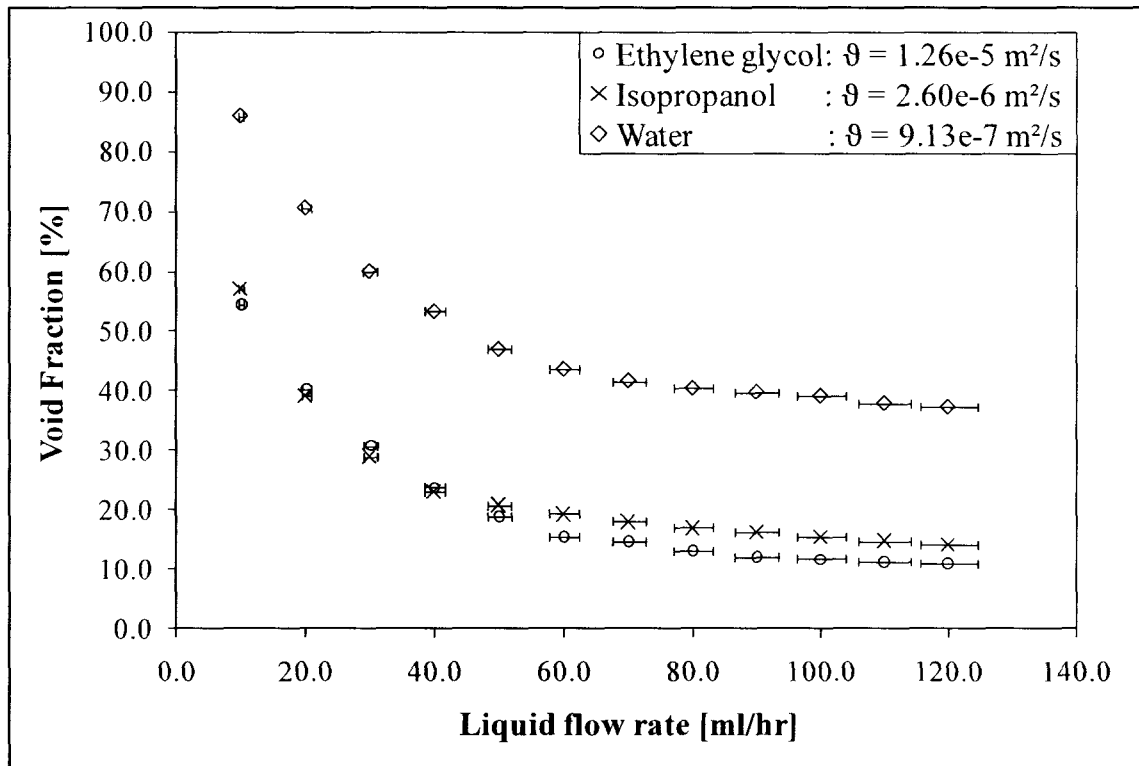


Figure 6.49 Plot gives the void fraction of bubble formation in base channel for base liquids with different kinematic viscosities (base channel  $162\mu\text{m}$ , secondary channel  $10\mu\text{m}$ , Gas flow rate  $0.145\text{ml/hr}$ )

#### 6.4 Co-Flow Bubble Generators with Flow Focusing

The effect of introducing flow focusing in the new generation of co-flow devices is studied in this section. The performance of the co-flow devices while using different shapes of flow focusing structures is compared to get an optimized shape for the flow focusing technique introduced here in this study. As discussed in the Section 6.2 of cross-flow devices with flow focusing technique, flow focusing ensures the flow to be more

focused to the orifice of bubble formation, helping the bubbles to get detached from the orifice at a smaller diameter compared to the bubbles generated from the device with ordinary base channels. In the case of co-flow devices, the use of flow focusing structures also helps to reduce the size of the flow separation region in front of the orifice, helping the bubbles to detach from the orifice at smaller bubble diameters. The reduction in the flow separation region in front of the orifice is studied with the help of CFD software. The contour plot giving the velocity profile of the liquid flow through the base channel with and without flow focusing is represented in Figure 6.50.

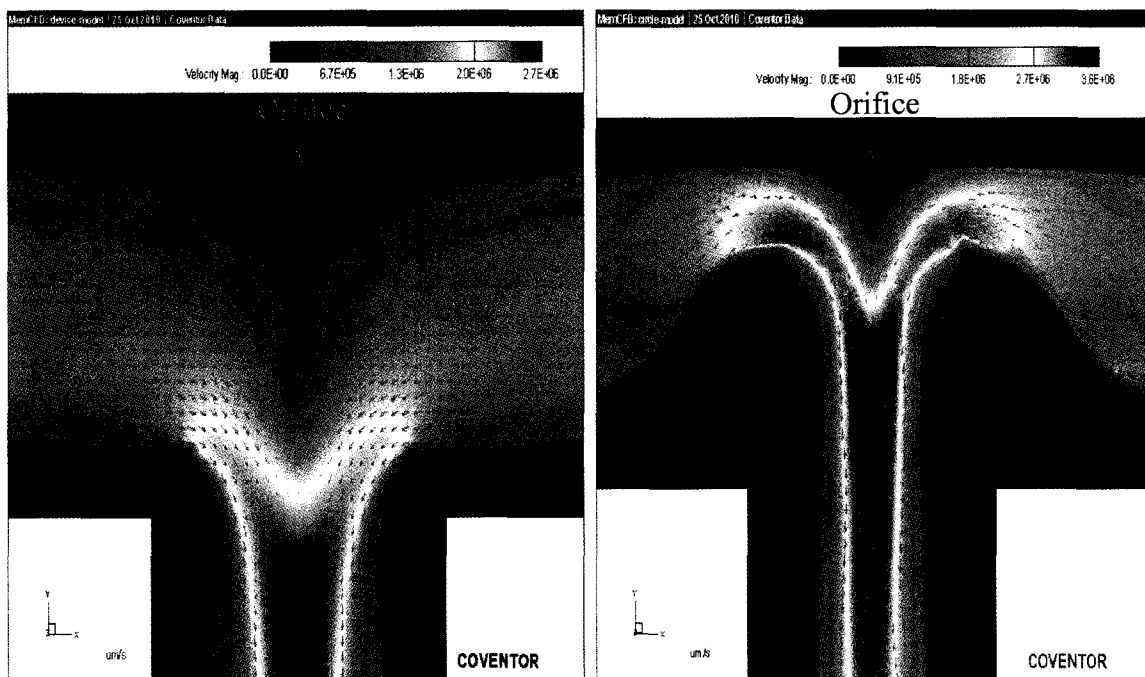


Figure 6.50 Contour plot of velocity profile for base liquid flow inside base channel with and without flow focusing device (base channel  $150\mu\text{m}$ , Reynolds number of liquid flow 250)

It can be noted from the figure that as a flow focusing structure is introduced in the base channel, the flow in front of the orifice is focused to the orifice, and the flow separation region is reduced considerably. The flow focusing structures demonstrated in Figure 6.50 are circular in shape and have a radius of  $100\mu\text{m}$ . The base channels used in both cases (with and without flow focusing structures) are of  $150\mu\text{m}$  in hydraulic diameter, and the Reynolds number of liquid flow at which the contour plots are generated is 250. The velocity vectors included in the contour plot give a picture of the flow direction in each region of base liquid flow inside the channel. Other than decreasing the size of the flow separation region, the flow focusing structures serves the purpose of increasing the velocity of the liquid flow around the orifice, helping the detachment of the bubbles the orifice at a smaller diameter.

#### **6.4.1 Case 1: Comparison of co-flow device performance with and without flow focusing technique**

Figure 6.51 gives the comparison of the bubble diameter formed in co-flow devices with and without flow focusing structures. The graph is plotted for two different gas flow rates through the secondary channel. It can be noticed from the figure that the size of the bubbles decreases considerably while using flow focusing structures in the base channel. The reduction occurs for both the gas flow rates and reduction of bubble diameter while introducing flow focusing technique at higher Reynolds numbers of base liquid flow. The reduction in bubble diameter by introducing flow focusing structures at same Reynolds number of liquid flow through the base channel proves the purpose and advantage of using the flow focusing technique in the co-flow devices.



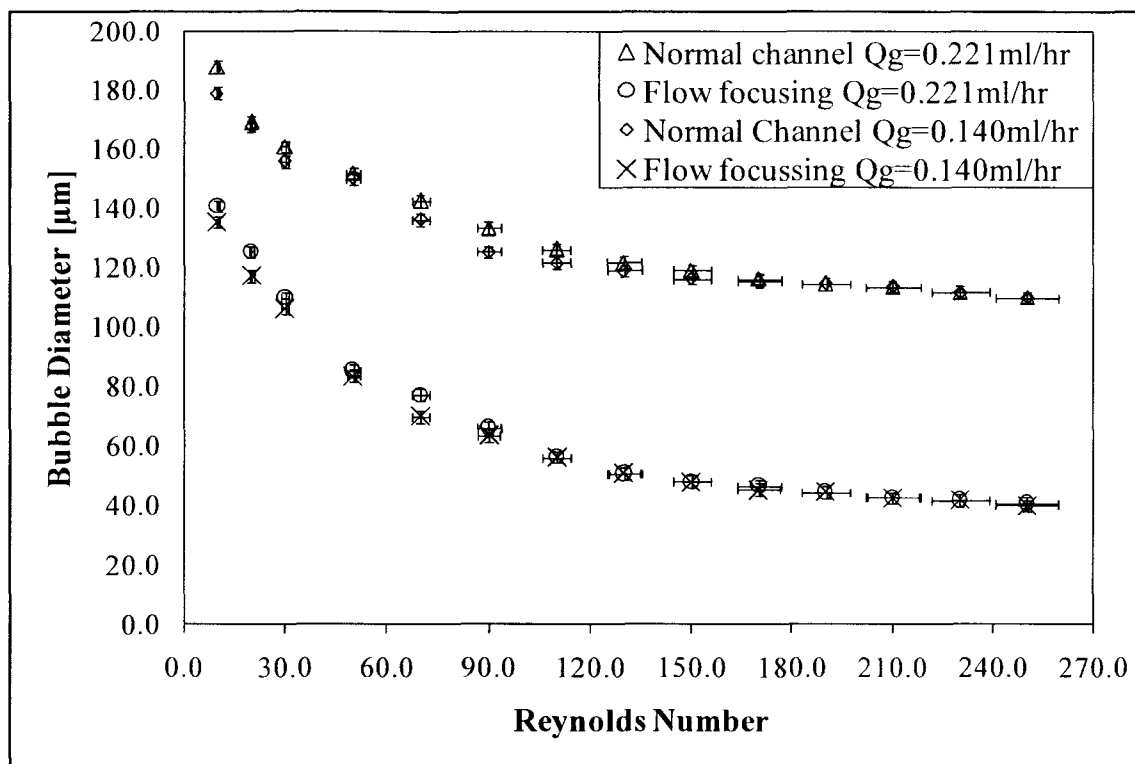


Figure 6.51 Plot gives the comparison between bubble diameters formed in co-flow devices with and without flow focusing (base channel  $162\mu\text{m}$ , secondary channel  $10\mu\text{m}$ , flow focusing structure height  $100\mu\text{m}$ )

#### 6.4.2 Case 2: Comparison of the performance of co-flow devices with different shapes of flow focusing structures

For the purpose of optimizing the shape of flow focusing structures introduced in the base channel, the performance of the co-flow device with three different shapes of flow focusing structures is compared in this section. The three structures have the shapes circle, triangle, and square. Figure 6.52 gives the layout of the masks used in the manufacturing of co-flow devices with three different shapes of flow focusing structures. The circular structure has a radius of  $100\mu\text{m}$ ; the square has  $100\mu\text{m}$  sides, and triangle has a height of  $100\mu\text{m}$ . The performance and contour plots of the co-flow devices having these three different structures is represented in Figure 6.53 and 6.54.

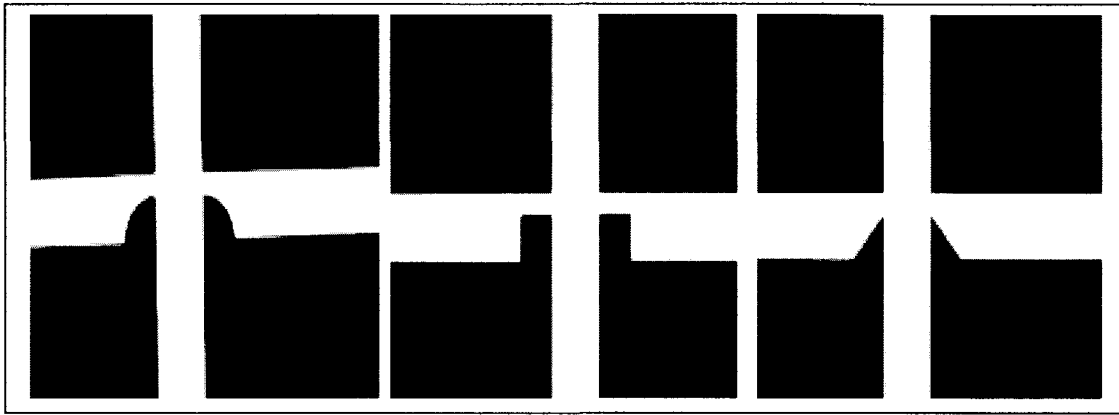


Figure 6.52 Mask layouts for manufacturing different shapes of flow focusing structures inside the base channel of co-flow device.

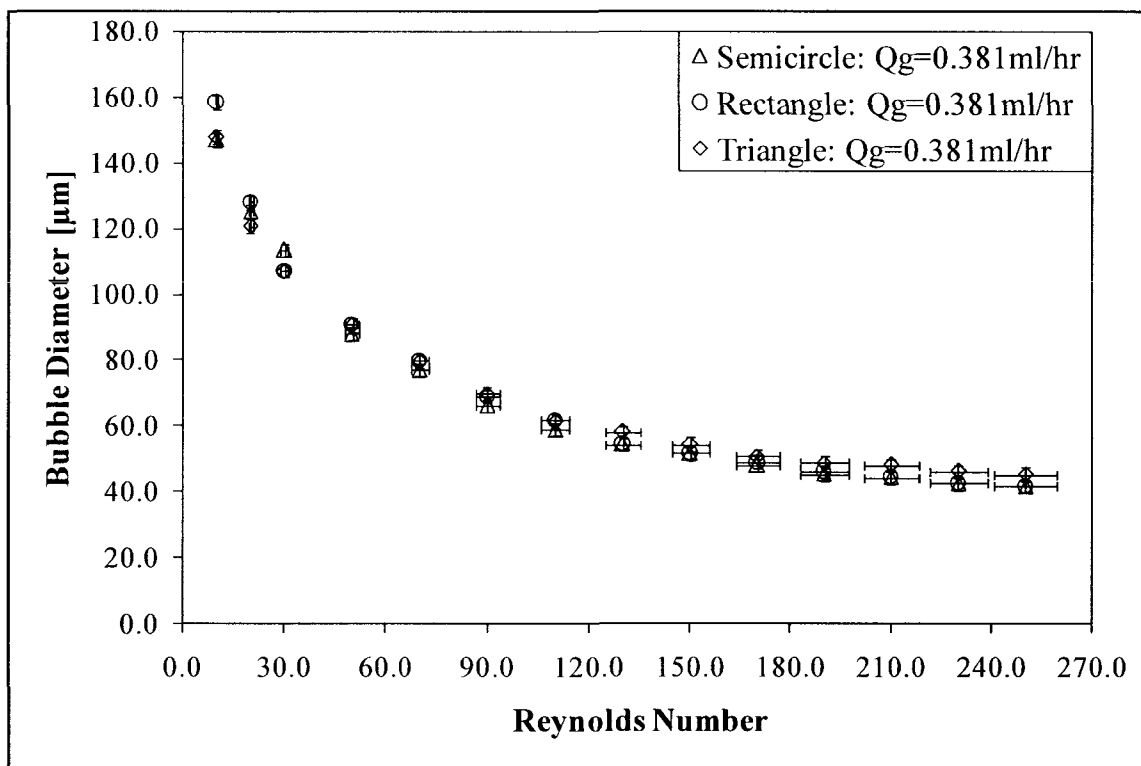


Figure 6.53 Plot gives the comparison between bubble diameters formed in co-flow devices with three different shapes of flow focusing structures (base channel  $162\mu\text{m}$ , secondary channel  $10\mu\text{m}$ , flow focusing structure height  $100\mu\text{m}$ )

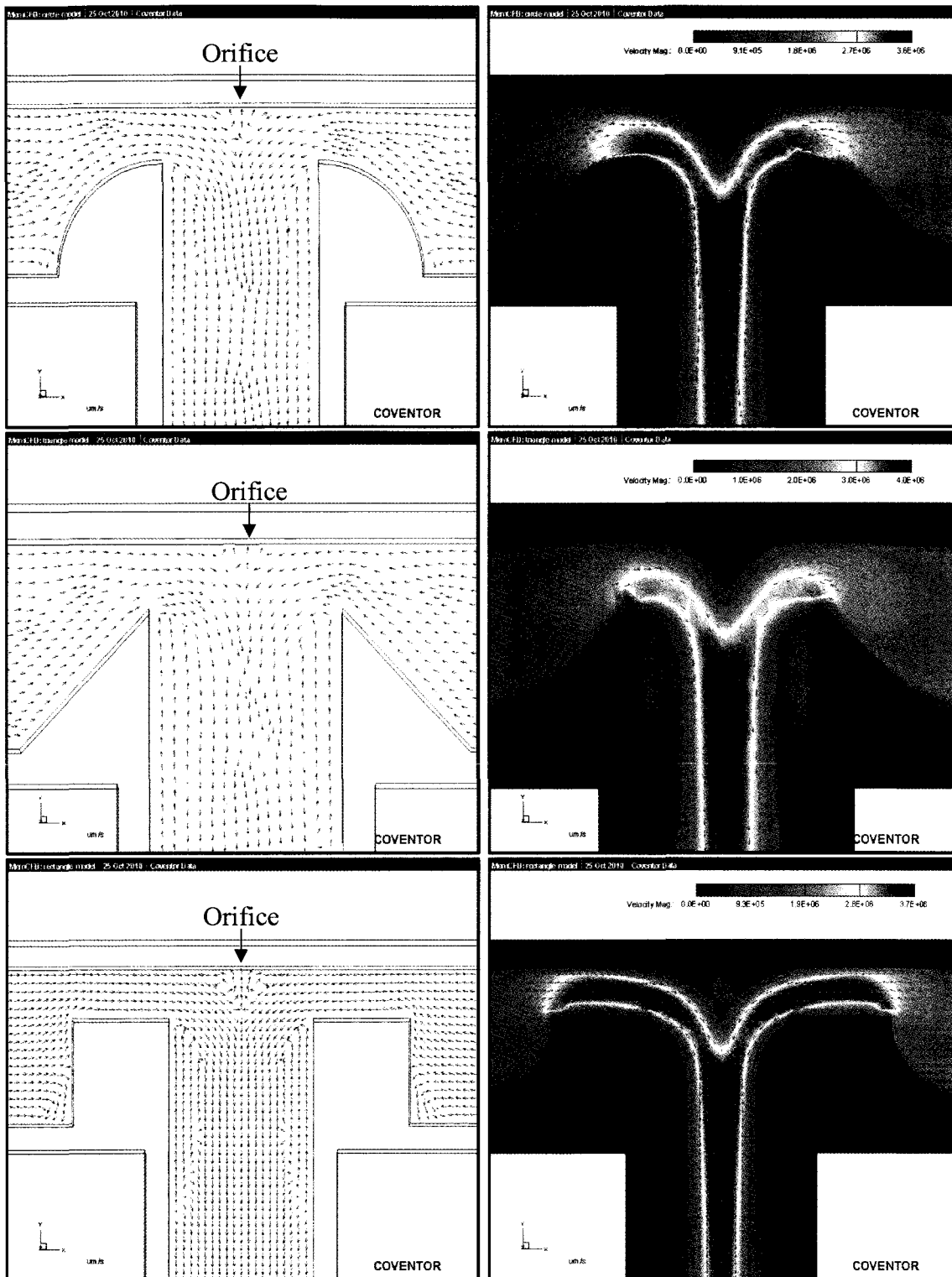


Figure 6.54 Contour plot of velocity profile for base liquid flow inside base channel with different shapes of flow focusing device (base channel  $150\mu\text{m}$ , Reynolds number of liquid flow 250)

Figure 6.54 gives the contour plot of velocity profile in co-flow devices with flow focusing. From Figure 6.53 it can be noted that the diameters of the bubbles co-flow devices with three different shapes of flow focusing structures have the same magnitude. From Figure 6.54 it can be observed that the reduction in the flow separation region in front of the orifice while using different shapes of flow focusing structures is uniform and accounts for the formation of the same size bubbles from all the devices. The vector plot of the velocity profile represented in Figure 6.54 represents the flow separation regions in the liquid junction in front of the orifice.

#### **6.4.3 Case 3: Comparison of void fraction of bubble formation in co-flow device with flow focusing**

This section compares the void fraction of bubble formation in the co-flow devices with different shapes of flow focusing structures at different gas flow rates through the secondary channel. Figure 6.55 gives the void fraction of bubble formation in the base channels while using circular flow focusing structures at three different gas flow rates. It can be observed from the figure that the change in the gas flow rate through the secondary channel does not have much effect on the void fraction of bubble formation in the base channel. The reduction in the flow separation region, and the increase in the base liquid velocity in the region of bubble formation, dominate the effect created by the change in the gas flow rate through the secondary channel. The vector plot given in Figure 6.54 shows the uniform distribution of the liquid flow in the base channel while using circular flow focusing structures. Another interesting observation that can be made from Figure 6.55 is that all the bubble formation corresponding to all values of gas flow rate is limited to the active region even at a very low value of Reynolds number of liquid

flow through the base channel. This again proves the superiority of using the flow focusing technique inside the co-flow bubble generation device.

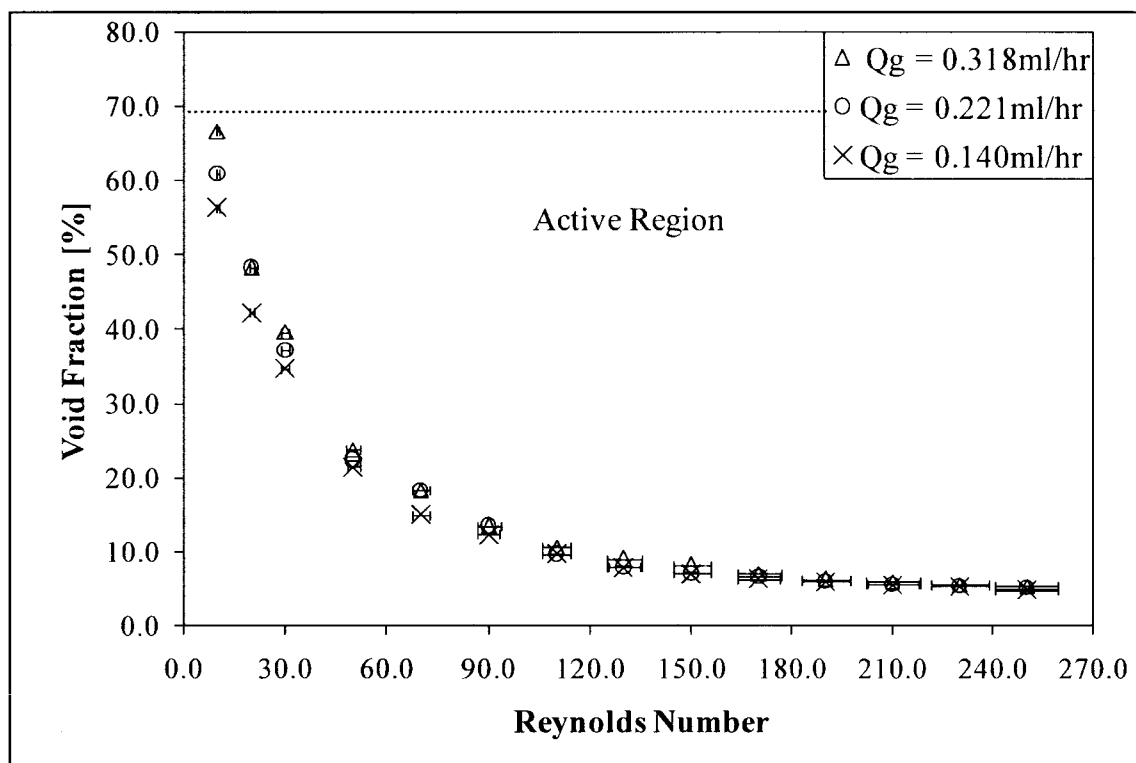


Figure 6.55 Plot gives the variation in void fraction of bubbles formed in co-flow devices with semi-circle flow focusing structure (base channel  $162\mu\text{m}$ , secondary channel  $10\mu\text{m}$ , flow focusing structure height  $100\mu\text{m}$ )

Figure 6.56 represents the void fraction of bubble formation in co-flow device with triangular flow focusing structures in the base channel. Again, the graph is plotted for three different values of gas flow rates through the secondary channel. It can be noted that for the higher values of gas flow rates, the void fraction of bubble formation is close to one another. But for the lowest value of gas flow rate through the secondary channel, the void fraction of bubble formation is lower compared to the other gas flow rates. This change in the void fraction of bubble formation in the base channel can be accounted for

by the flow maldistribution in front of the orifice while using a triangular flow focusing structure.

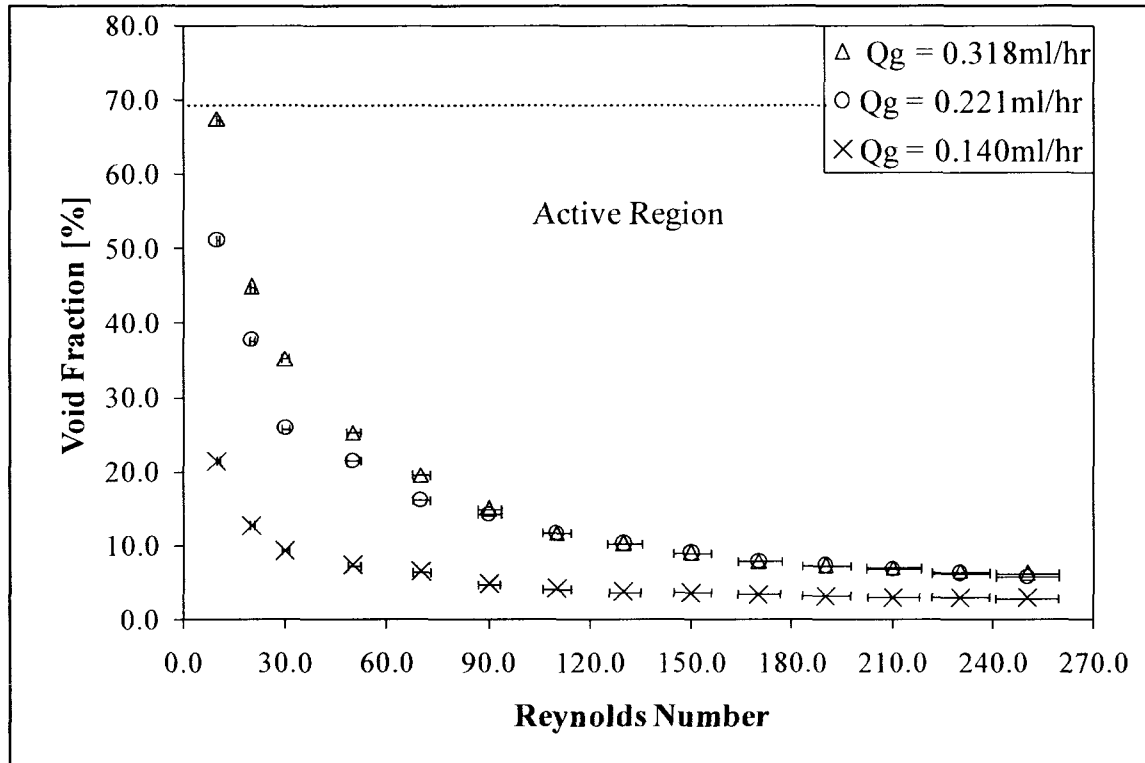


Figure 6.56 Plot gives the variation in void fraction of bubbles formed in co-flow devices with triangle flow focusing structure (base channel  $162\mu\text{m}$ , secondary channel  $10\mu\text{m}$ , flow focusing structure height  $100\mu\text{m}$ )

Figure 6.57 shows the enlarged view of the vector plot of velocity profile of liquid flow in front of the orifice. The same observation was made for the cross-flow device while using triangular flow focusing structures. It can be noted from the figure that the flow in the region of liquid merging from the two base channels is not uniform in nature compared to the flow in base channel with circular structure. The regions of flow separation in front of the orifice causes the change in the void fraction of bubble formation at low values of gas flow rate while using triangular structures.

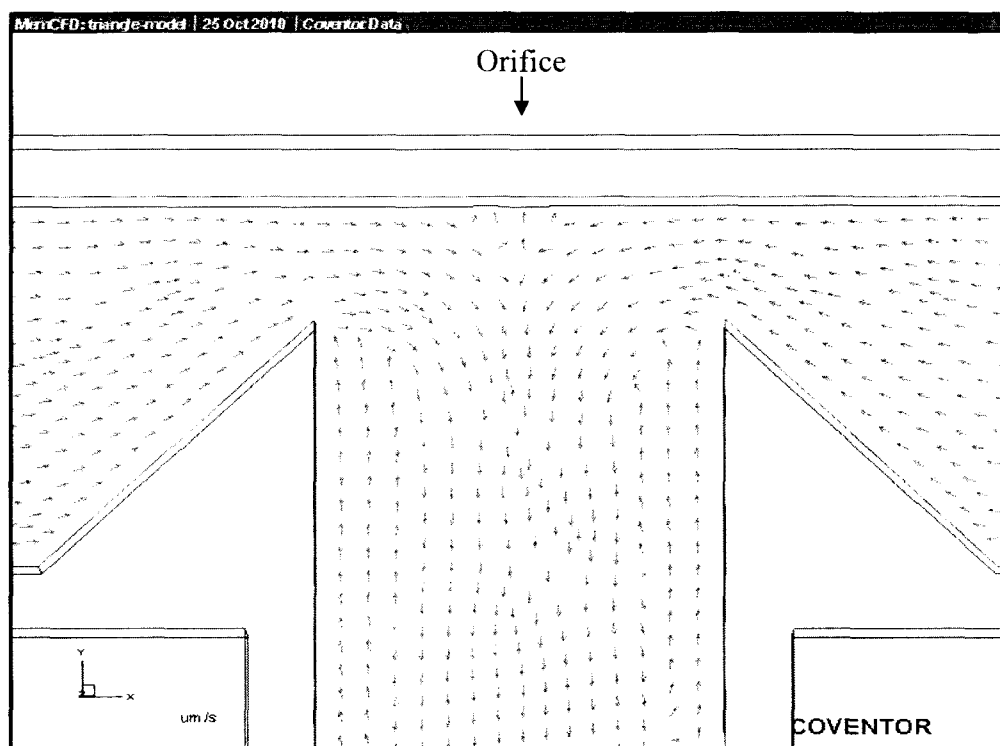


Figure 6.57 Vector plot of velocity profile for base liquid flow inside base channel with triangular flow focusing structure (base channel  $150\mu\text{m}$ , Reynolds number of liquid flow 250)

## 6.5 Droplet Generators

This section discusses the generation of droplets using the new generation of droplet generators introduced in this study. The feasibility of using the new technique for the generation of the droplets in the micro channels by using fused silica tube as the secondary channel was studied in the cross-flow device with base channel of hydraulic diameter  $160\mu\text{m}$  and secondary channel of diameter  $75\mu\text{m}$ . Water was used as the base liquid and ultra pure Paraffin wax oil was used as the secondary liquid. The results obtained from the feasibility study are represented in Figure 6.58.

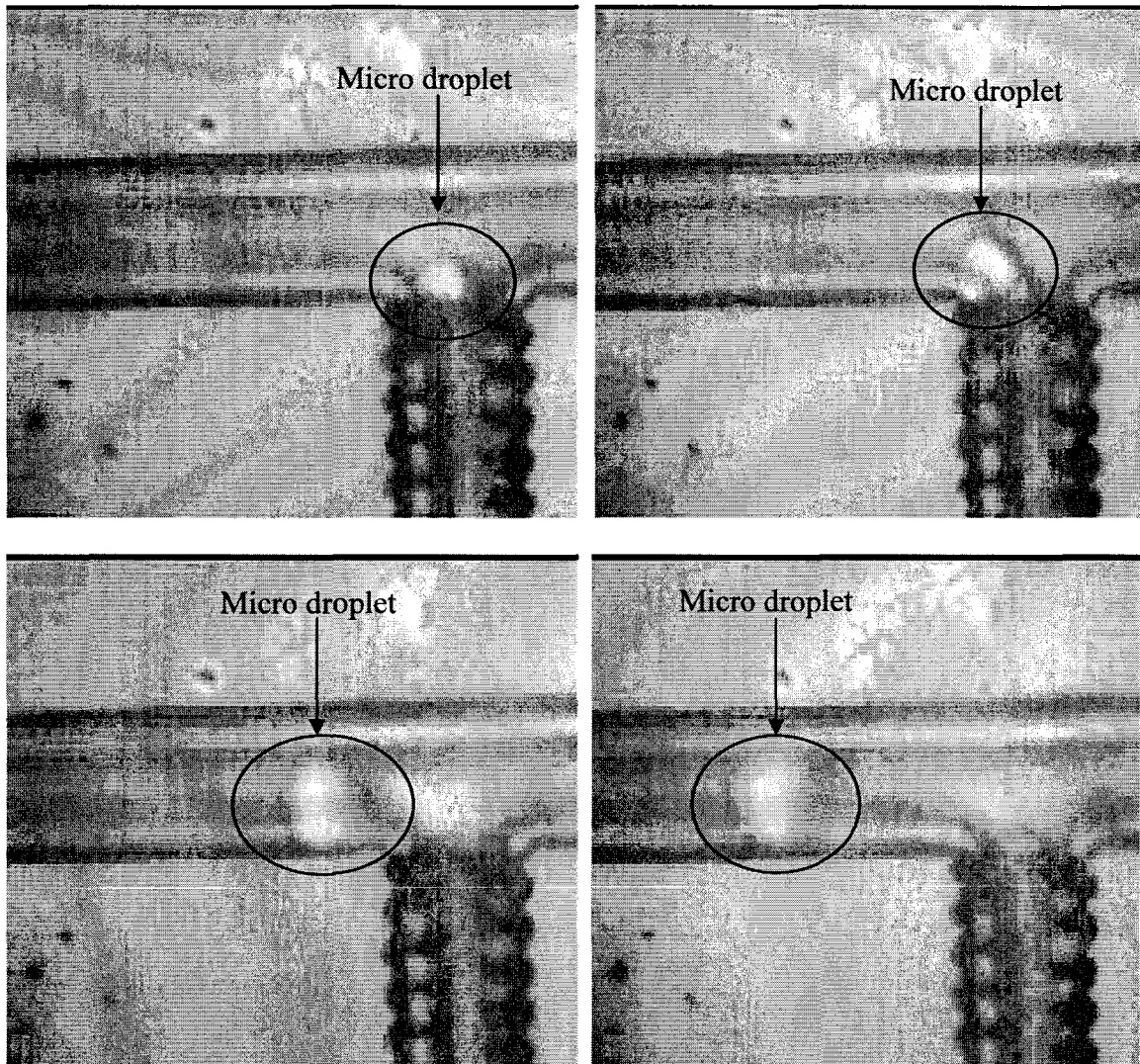


Figure 6.58 Droplet formations in cross-flow device (base channel  $162\mu\text{m}$ , secondary channel  $75\mu\text{m}$ )

Figure 6.58 represents the picture of droplet formation in a cross-flow device at various phases of droplet formation and detachment from the orifice. Unlike the bubble formation from a cross-flow device, the droplets which are being formed from the orifice of a cross-flow device tends to lean towards the edge of the base channel in the flow direction even before it detaches from the orifice. Yet, the major advantage of the droplet generation, by using a fused silica channel of a hydraulic diameter less than the hydraulic



diameter of the base channel at least by a factor of two, is the formation of unconfined bubbles and the elimination of satellite droplets. The variation in the droplet generation and detachment with the change in the Reynolds number of the base liquid and secondary liquid is studied in the case studies considered below.

### 6.5.1 Case 1: Cross-flow droplet generators

The variation in the bubble diameter with change in the Reynolds number of the base liquid at three different flow rates of secondary liquids through the secondary channel, and is plotted in Figure 6.59.

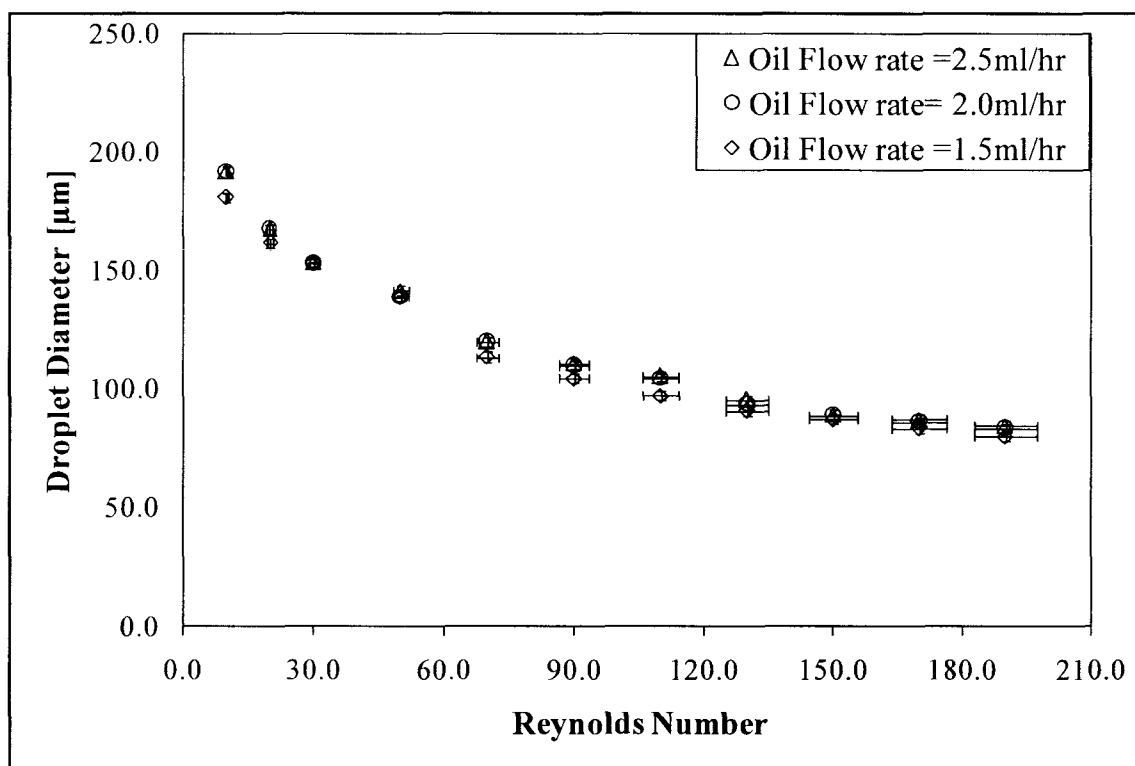


Figure 6.59 Plot gives the variation in the droplet diameter formed in cross-flow devices with water as base fluid and Paraffin oil as secondary fluid (base channel 160 $\mu$ m, secondary channel 75 $\mu$ m)

It can be observed that as the Reynolds number of the base liquid increases, the diameter of the droplet decreases (the same behavior was observed in the study of the bubble generation also). But the rate of change in the droplet diameter with Reynolds number of the base liquid flow is less compared to the rate of change in the bubble diameter with Reynolds number of liquid flow. At very low Reynolds number of base liquid flow, the droplets are confined to the base channel walls, but the transition from the confined region to the active region happens at very low value of Reynolds number of base liquid flow around 30. The change in the size of droplet diameter with the change in the secondary liquid flow rate is also studied in Figure 6.59. It can be observed that the change in the secondary liquid flow rate, from 1.5ml/hr to 2.5ml/hr, does not make much difference in the diameter of the droplets being formed from the orifice.

### **6.5.2 Case 2: Co-flow droplet generators**

The droplet formation inside a co-flow device at various time intervals is given in Figure 6.60. The base channel has a hydraulic diameter of  $165\mu\text{m}$  and the secondary channel has a diameter of  $75\mu\text{m}$ . It can be observed from the figure that as the diameter of the droplet increases, it gets extended into the base channel, and the neck of the droplet gets pinched off at a certain diameter. As the diameter of the secondary channel decreases, the droplet extension into the base channel decreases and avoids the chance of satellite droplet formation in the device. Figure 6.61 represents the variation in the droplet diameter with the variation in the Reynolds number for two different secondary fluid flow rates. As in the previous case, the droplet diameter decreases with an increase in Reynolds number of base liquid flow, but the rate of decrease in droplet diameter is

less compared to the rate of decrease of droplet diameter in a cross-flow device. The same trend was observed while studying the bubble formation in a co-flow device.

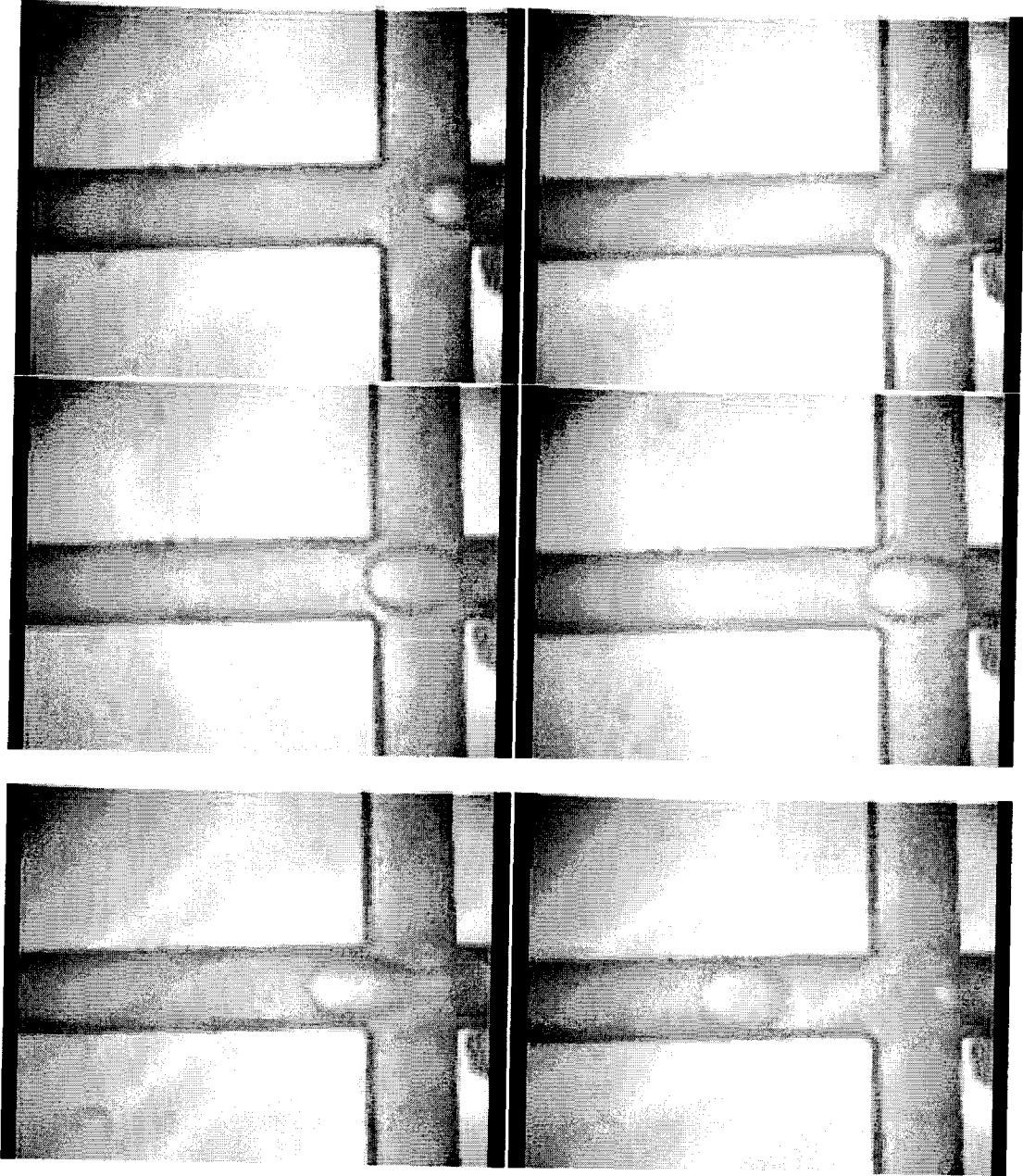


Figure 6.60 Droplet formation in a co-flow device at various time intervals (base channel 165 $\mu\text{m}$ , secondary channel 75 $\mu\text{m}$ )

The fluid flow rate through the secondary channel is too varied to study its effect on the droplet diameter. It was observed Figure 6.61 that with a change in the secondary fluid flow rate from 2ml/hr to 3ml/hr the droplet diameter varies a little.

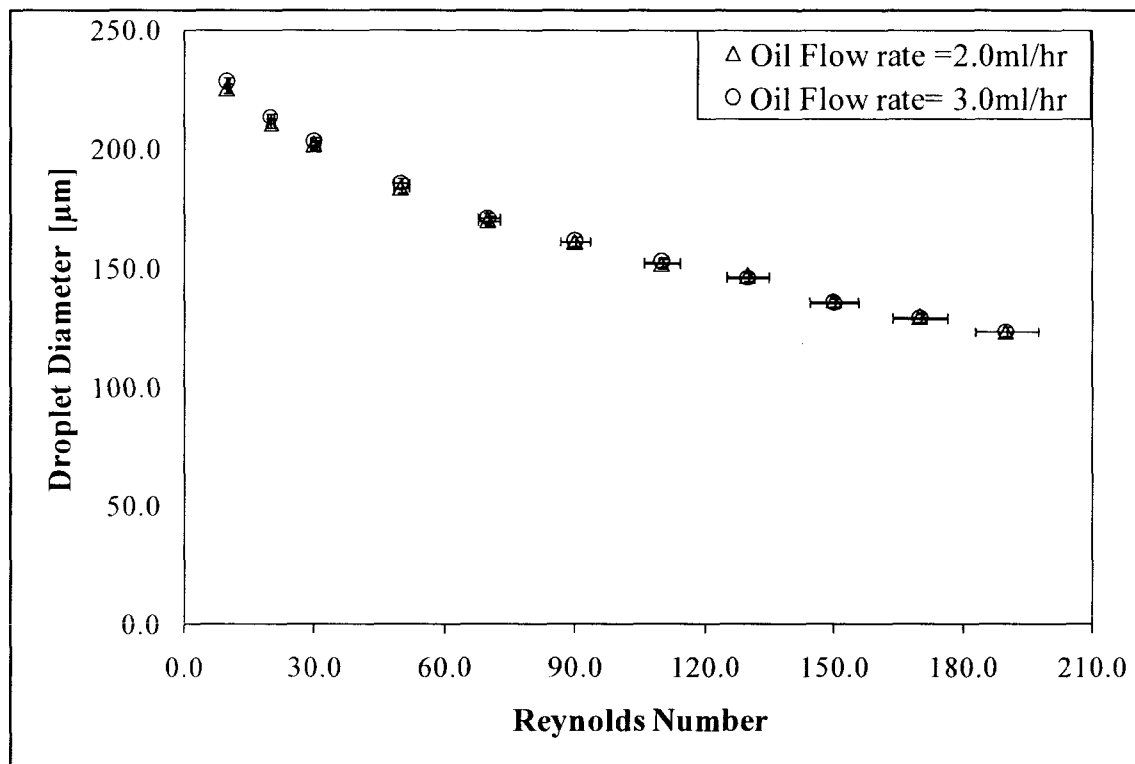


Figure 6.61 Plot gives the variation in the droplet diameter formed in co-flow devices with water as base fluid and Paraffin oil as secondary fluid (base channel 165 $\mu$ m, secondary channel 75 $\mu$ m)

### 6.6 Cross-flow Bubble Generator with Round Base Channel

The heat transfer characteristics of a zig-zag micro channel were studied by B. Mathew et al. in 2010 [54]. The study showed the flow pattern inside a zig-zag micro channel, and this led to the investigation of bubble generation in a cross-flow device with a round micro channel as the base channel. The schematic of the cross-flow bubble generator with a round base channel and the contour plot of the velocity profile in a round

channel are given in Figure 6.62. The main factor behind the generation of smaller bubbles in a base channel is the focusing of the base liquid flow onto the side of the base channel with bubble generation orifice. Previously in this study, this result was obtained by using the flow focusing technique, and now in this section the flow focusing is obtained by using a base channel of round geometry.

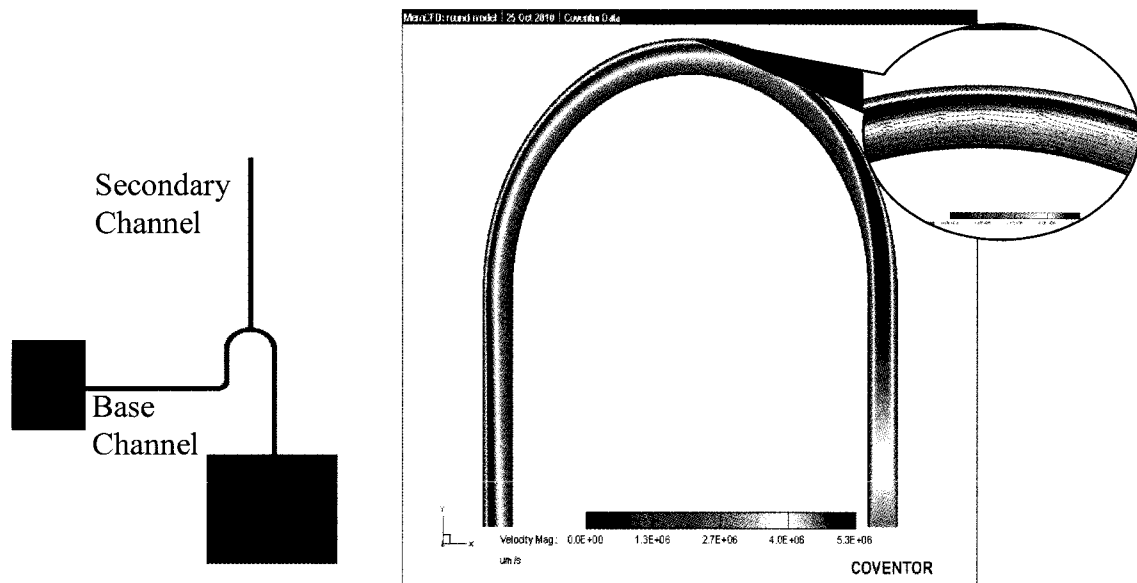


Figure 6.62 Schematic of cross-flow generator with round channel and contour plot of velocity profile inside the round channel

In Figure 6.62, the contour plot of the velocity profile in a round micro channel shows that the flow inside a round channel will be focused onto the outer side of the channel. So by positioning the orifice of the bubble formation onto the outer side of the base channel bubble of lesser diameter can be obtained in the base channel. The bubble formation in a base channel of round geometry is shown in Figure 6.63. Figure 6.64 gives the comparison of bubble diameter obtained using different cross-flow techniques.

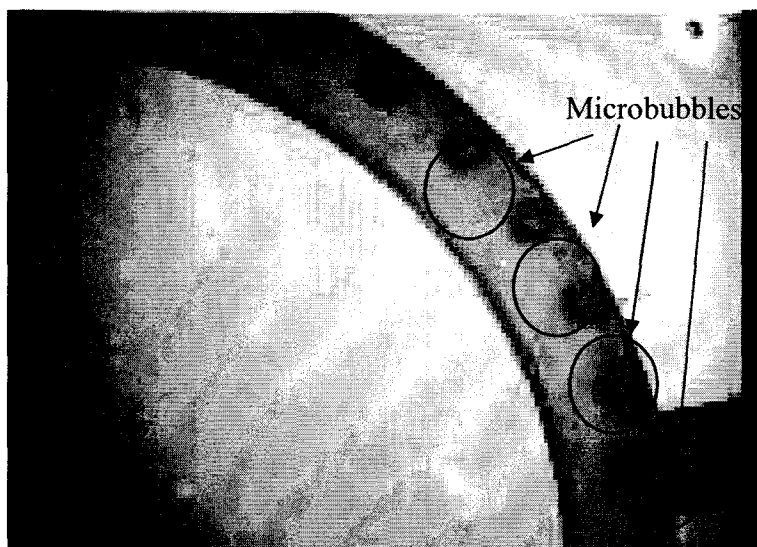


Figure 6.63 Bubble formation in cross-flow device with round base channel. (base channel  $160\mu\text{m}$ , secondary channel  $10\mu\text{m}$ )

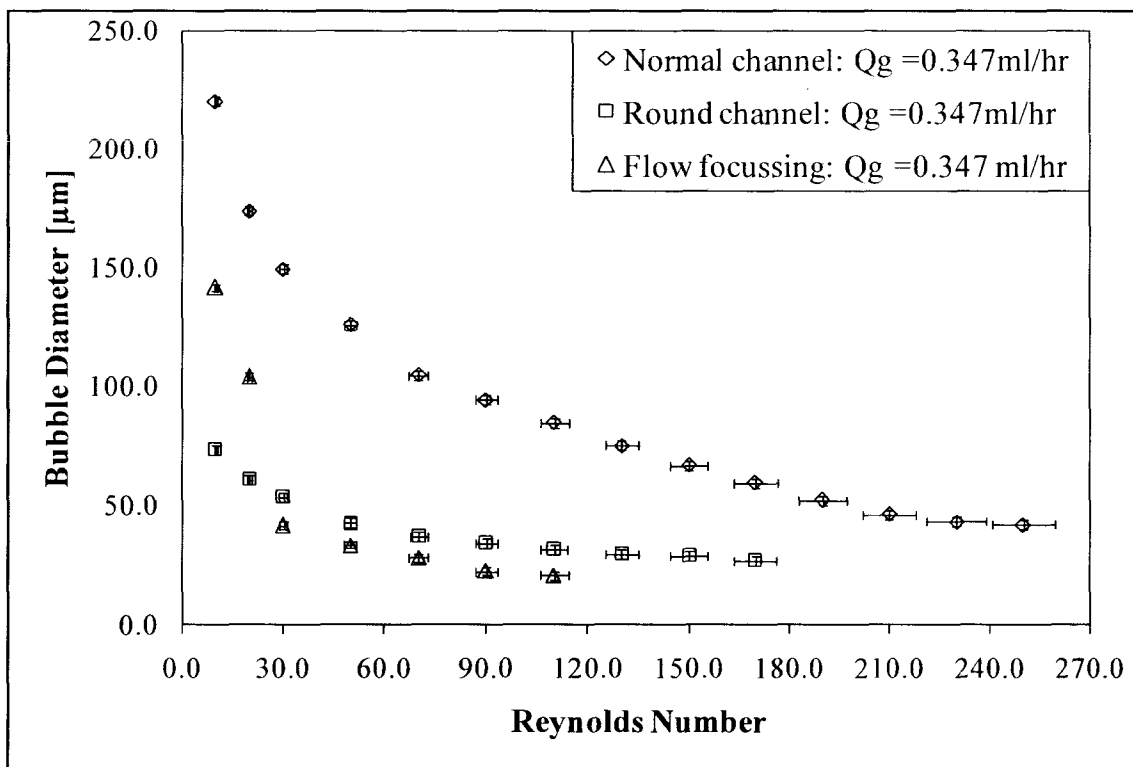


Figure 6.64 Comparison of bubble diameter obtained from a straight base channel (with and without flow focussing) and round base channel. (base channel  $160\mu\text{m}$ , secondary channel  $10\mu\text{m}$ , flow focussing structure (semi-circle) height  $100\mu\text{m}$ )

From Figure 6.63 it can be noticed that the bubbles generated in the cross-flow device with a round base channel is moving through the outer side of the base channel where the velocity of the base liquid is maximum. The comparison between the bubble diameter obtained from an ordinary base channel, a round base channel, and a base channel with flow focusing structure of radius  $100\mu\text{m}$  is represented in Figure 6.64.

It can be observed from the Figure 6.64 that while using a round base channel the bubbles that are formed inside the channel are much smaller than those were formed in the straight base channel. At lower Reynolds number of liquid flow rate, the cross-flow devices with a round base channel can produce bubbles which are smaller than the ones produced by the base channels with flow focusing structures. But as base liquid Reynolds number increases, the cross-flow devices with flow focusing structures show the better performance.

## CHAPTER 7

### FUTURE WORK AND CONCLUSIONS

One of the major objectives of the current study was to generate microbubbles of diameter less than  $15\mu\text{m}$  in a micro channel. This objective is achieved in the current study, and this enables the microbubbles to be used for the direct oxygenation of blood. The amount of oxygen needed to be transferred into the blood of an adult person in order to replace the mechanical ventilator fully is very large compared to the volume of individual microbubbles which have a diameter of  $15\mu\text{m}$ . So multiple arrays of micro channels with more than one orifice in a channel have to be stacked together to achieve the objective of oxygenation of the blood. The future work towards the blood oxygenation project should focus on stacking the micro channels into a device that can produce enough microbubbles and is capable of replacing the mechanical ventilators

A major factor that is affecting the bubble diameter while the gas flow rate through the secondary channel is modified is the absolute pressure change in front of the orifice. A study of the flow pattern and absolute pressure in the region in front of the orifice during the bubble formation can reconfirm this hypothesis. For the purpose of studying the absolute pressure, some kind of pressure sensor has to be integrated in front of the orifice which can accurately monitor the pressure variation in the region. The flow pattern can be studied with the help of particle image velocimetry technique. The



determination of these two factors will help to define the bubble formation from both the cross-flow and co-flow device with greater accuracy. Determining the flow separation region in front of the orifice in a co-flow microbubble generator, and determining the saturation region of the bubble formation in the device is another area where future work has to be concentrated on. The mathematical model can be generated for this purpose, and the validation of the mathematical model can be done using the experimental analysis of the flow separation region using facilities like particle image velocimetry technique. The merging of the bubble which is explained in the Section 6.1 needs to be addressed more broadly with more resources, to study how it affects the bubble formation in the confined region. None of the conventional bubble generators have addressed this problem experimentally or mathematically, and these areas that need to be studied carefully.

The bubble generating devices manufactured using the new technique, of using fused silica tube as the secondary channel, can be used to generate both the bubbles and droplets. But in the current study the droplet generation is studied only to a limited extent in order to prove the advantages of using the new generation devices over the conventional devices. A detailed study of the droplet generation in both cross-flow and co-flow devices which includes the parametric study has to be done as a part of the future work of this project. The current model developed for the prediction of the bubble diameter in a cross-flow device has to be experimentally validated for the droplet formation, and needs to be updated if necessary for the prediction of droplet diameter at detachment in the cross-flow droplet generators. The existing models already developed can predict the bubble formation in co-flow devices, but lack experimental validation which can not be validated from the unconfined droplets obtained from the device.

A conclusion of this study needs to review the objectives of the study and explain how this study has addressed each of the initial objectives. The major objectives of this study at the beginning are as follows.

- 1) The main objective of this study throughout its phases is to generate microbubbles of a size less than  $15\mu\text{m}$  in diameter for the purpose of direct oxygenation of blood without using mechanical ventilators (Objective achieved).
- 2) The secondary objective of this work is to understand the mechanism behind the formation of unconfined bubble inside micro channels for a wide range of fluid flow rate through both the base and secondary channels and thereby overcome the limitations of the conventional bubble generators (Objective achieved).
- 3) The third objective of this work is to validate the mathematical model generated to predict the bubble diameter at its detachment experimentally in a cross-flow device. The model can be modified to predict the bubble diameter inside a co-flow device (Objective partially achieved).
- 4) The fourth objective of this work is to introduce flow focusing inside the cross-flow droplet/bubble generators and obtain smaller droplet/bubbles at lower Reynolds number of the base fluid compared to the models which do not use the flow focusing techniques (Objective achieved).

The study satisfied all of its objectives, and the major conclusions of the study are listed below.

- 1) The new generation of microbubble/droplet generators utilizing both cross-flow and co-flow techniques were designed, manufactured and tested during the work.

- 2) Microbubbles of a diameter  $11\mu\text{m}$  were generated in the base micro channel of hydraulic diameter  $160\mu\text{m}$  using a secondary channel of diameter  $2\mu\text{m}$  (Objective 1).
- 3) Microbubbles of a diameter approximately  $5\mu\text{m}$  were generated in a base channel of hydraulic diameter  $160\mu\text{m}$ , having a semi-circular flow focusing structure of radius  $100\mu\text{m}$  using a secondary channel of  $2\mu\text{m}$  (Objective 1).
- 4) The important forces acting on the bubble during its formation and detachment inside the base channel were determined to be surface tension and drag force (Objective 2).
- 5) A parametric study based on the physical properties of base liquid and secondary fluid was done and analyzed during the study for both cross-flow and co-flow devices to understand their effect on the bubble diameter at detachment and formation (Objective 2).
  - Kinematic viscosity and Reynolds number of the base liquid are the major factors in determining the bubble diameter at the detachment from the orifice.
  - The pressure drop of the gas flow across the secondary channel will affect the bubble diameter at low Reynolds numbers of base liquid flow rates.
- 6) A parametric study based on the geometry of the base channel and secondary channel was conducted to study the effect of the geometric parameters on the bubble diameter at detachment and during formation (Objective 2).
  - Hydraulic diameter of the secondary channel affects the bubble diameter at its detachment from the orifice considerably

- Hydraulic diameter of the base channel does not have much effect on the bubble diameter at its detachment as long as the shorter side of the base channel is kept constant.
- 7) Unconfined bubbles/droplets were generated inside the cross-flow and co-flow devices over a wide range of Reynolds number of fluid flow rates through both the base and secondary channel (Objective 2).
  - 8) Three regions of bubble formation, confined, active and saturation regions, were defined for a better understanding of the microbubble formation inside cross-flow devices.
    - The equations for the transition point of each region to the next region are derived in the study and are validated using the experimental data from different devices.
    - The study was unable to develop an equation for determining the transition point from active region to the saturation region inside co-flow devices due to the formation of flow the separation region.
  - 9) The mathematical model developed to predict the bubble diameter at its detachment from a cross-flow device is validated using the experimental data (Objective 3).
    - The detachment of the microbubbles of a diameter less than the  $2/3^{\text{rd}}$  of the hydraulic diameter of the base channel is predicted accurately by the mathematical model.
    - The modification of the mathematical model to predict the bubble generated from a co-flow device was unable to be attained due to the formation of flow separation region in the co-flow devices.

- 10) A feasibility study was conducted on the introduction of flow focusing technique inside the cross-flow devices using the CFD package COMSOL (Objective 4).
- 11) A flow focusing technique was introduced in the cross-flow devices for the first time and the technique was able to produce bubbles of smaller diameter (Objective 4).
- 12) The effect of introducing the flow focusing technique in the new generation of co-flow devices was also studied and the technique was proven to have advantages like reduction in flow separation region and formation of smaller bubbles (Objective 4).
- 13) An optimization study based on both the geometry and shape of the flow focusing structures was done, and semi-circular structures were proved to have the best performance (Objective 4).
- 14) A new technique for generating smaller unconfined bubbles in a base channel is introduced by the usage of round base channel. The method proved to be very effective.

The study of microbubble/droplet generation in both cross-flow and co-flow devices was conducted in this investigation, and the study achieved 95% of its initial objectives.

## **APPENDIX A**

### **NOMENCLATURE**

$\rho_l$	: density of liquid
$\rho_g$	: density of gas
$\sigma$	: surface tension
$\mu_l$	: viscosity of base liquid
$\mu_g$	: viscosity of the gas
$\alpha_{sat}$	: transition point of transition from active to saturation region
$A_l, A_c$	: cross-sectional area of the liquid channel
$A_{lm}$	: modified cross-sectional area at orifice
$A_{eff}$	: effective diameter of the microbubble
$C_D$	: drag coefficient
$C_{MD}$	: modified drag coefficient
$D$	: depth of the base channel
$D_b$	: diameter of the microbubble
$D_o$	: diameter of the orifice
$D_h, D_H$	: hydraulic diameter of the base channel
$g$	: gravity
$L$	: length of the secondary channel
$P$	: perimeter of the base channel
$\Delta P$	: pressure drop
$Q$	: base liquid flow rate
$Q_g$	: gas flow rate
$R$	: radius of the microbubble
$\dot{R}$	: rate of change of microbubble diameter

$R_e$	: Reynolds number
$U_l$	: average velocity of the liquid
$U_{lm}$	: modified velocity around the obstacle
$U_l^*$	: effective liquid velocity during microbubble growth
$V_B$	: volume of the microbubble
$V_{max}$	: volume of the maximum unconfined bubble
$v$	: velocity of Base liquid
$W$	: width of the base channel



## **APPENDIX B**

### **MATLAB PROGRAM TO CALCULATE BUBBLE DIAMETER**

```

% Author: Tom J John

% Date: 09/27/2008

clc;

clear;

% Defining the constants

sigma = 72.8e-2;           % surface tension [N/m]

rhog = 1.123;             % Density of gas [kg.m3]

rhol = 997;               % Density of liquid [kg/m3]

visco = 0.000911;        % Viscosity of water

g=9.81;

% Defining input variables

Do =15e-6;                % Diameter orifice [m]

Qo = 2.31e-11;           % Flow rate of gas [m3/s]

Ul = 1.32;               % Velocity of liquid [m/s]

w = 170e-6;              % Width of the channel [m]

d = 150e-6;              % Depth of the channel [m]

% Initial calculations

Ro = Do/2;               % Radius of the nozzle [m]

Al = w*d;                % Cross-sectional area [m2]

Dh = 4*(w*d)/(2*(w+d)); % Hydraulic diameter [m]

Re = rhol*Ul*Dh/visco ; % Reynolds number

Cd = (24/Re)+ (6/(1+sqrt(Re)))+0.4; % Drag coefficient

% Calculations

```

```

n=1; % Setting up a counter
Db=0; % initial bubble diameter
lhs=1; % Initial value of LHS
rhs=0; % Initial value of RHS
t=0; % Setting up a timer

while lhs >=rhs

    t=t+0.0001;
    V=Qo*t;
    V1=Qo*(t+0.0001);
    Db=(3*V/(4*pi))^(1/3);
    D1 =(3*V1/(4*pi))^(1/3);
    vb=(D1-Db)/0.0001;
    Uls=2*U1*(1-((Dh-Db)/Dh)^2);
    Reb=rhol*(Uls-vb)*Db/visco; % Bubble Reynolds number
    Cd = (24/Reb)+ (6/(1+sqrt(Reb)))+0.4;
    CD=18.5/Reb; % Drag coefficient
    Ab = pi*(Db/2)^2; % Area of the bubble [m2]
    Ueff=U1*Al/(Al-Ab);
    Fsig= pi*Do*sigma; % Surface tension
    Fi=11/16*rhog*4/3*pi*(Db/2)^3*vb; % Inertia force
    FDx=0.5*rhol*Ueff^2*(pi*Db^2/4)*Cd/(1-(Db/Dh)); % Drag force
    FB = (4/3)*pi*g*(rhol-rhog)*(Db/2)^3; % Buoyancy force
    Fm= rhog*Qo^2/(pi*Ro^2); % Momentum force

```

```
lhs=Fsig; % Balancing forces
rhs = sqrt((Fm+FDy+FB-Fi)^2+FDx^2);
n=n+1; % Incrementing the counter
end
```

**APPENDIX C**

**LIST OF PUBLICATIONS**

- [1] John, T. J., Mathew, B., Hegab, H., 2010, "Parametric Study on the Combined Thermal and Hydraulic Performance of Single Phase Micro Pin-Fin Heat Sinks Part I: Square and Circle Geometries," *International Journal of Thermal Sciences*, 49(11), pp. 2177-2190.
- [2] Bellamkonda, R., John, T. J., Mathew, B., DeCoster, M., Hegab, H., Davis, D., 2010, "Nanowire GMR Based Microfluidic Biosensor," *Journal of Micromechanics and Microengineering*, 20, Paper No. 025012.
- [3] John, T. J., Hegab, H., 2010, "Experimental Study of Microbubble Formation in Microchannels," ASME 8th International Conference on Nanochannels, Microchannels, and Minichannels, Montreal, Canada, FEDSM2010-ICNMM-2010-31155.
- [4] John, T. J., Mathew, B., Hegab, H., 2010, "S-Shaped Pin-Fins for Enhancement of Overall Performance of the Pin-Fin Heat Sink," ASME 3rd Joint US-European Fluids Engineering Summer Meeting, Montreal, Canada, FEDSM2010-ICNMM-2010-31164.
- [5] John, T. J., Mathew, B., Hegab, H., 2010, "Multi Layer Micro Pin-Fins Heat Sinks for Better Performance," ASME 8th International Conference on Nanochannels, Microchannels, and Minichannels, Montreal, Canada, FEDSM2010-ICNMM-2010-31167.
- [6] Mathew, B., John, T. J., Hegab, H., 2010, "Thermohydraulic Characteristics of Fluid Flow in a Zig-Zag Square Microchannel," ASME 8th International Conference on Nanochannels, Microchannels, and Minichannels, Montreal, Canada, FEDSM2010-ICNMM-2010-31160.
- [7] Mathew, B., John, T. J., Hegab, H., 2010 "Performance of Cross-flow Microchannel Heat Exchangers Subjected to Viscous Dissipation," ASME 3rd Joint US-European Fluids Engineering Summer Meeting, Montreal, Canada, FEDSM2010-ICNMM-2010-31159.
- [8] Kupwade-Patil, K., John, T. J., Mathew, B., Hegab, H., Cardenas, H., 2010 "Diffusion Analysis of Chloride in Concrete Following Electrokinetic Nanoparticle Treatment," ASME 8th International Conference on Nanochannels, Microchannels, and Minichannels, Montreal, Canada, FEDSM2010-ICNMM-2010-31153.
- [9] John, T. J., Mathew, B., Hegab, H., 2010, "Microchannel Heat Sinks with Embedded Pin Fin Structures," 10th AIAA/ASME Joint Thermophysics and Heat Transfer Conference, Chicago, USA, AIAA-4780.
- [10] John, T. J., Mathew, B., Hegab, H., 2010, "Characteristic Study on the Optimization of Micro Pin-Fin Heat Sink with Staggered Arrangement," 10th AIAA/ASME Joint Thermophysics and Heat Transfer Conference, Chicago, IL, USA, AIAA-4781.

- [11] Mathew, B., John, T. J., Hegab, H., 2010, "Dynamics of Fluid Flow in a Heated Zig-Zag Microchannel," 10th AIAA/ASME Joint Thermophysics and Heat Transfer Conference, Chicago, IL, USA, AIAA-5056.
- [12] John, T. J., Mathew, B., Hegab, H., 2009, "Characteristic Study on the Optimization of Pin Fin Micro Heat Sinks," ASME International Mechanical Engineering Congress and Exposition, Lake Buena Vista, FL, USA, IMEC2009-11816.
- [13] John, T. J., Mathew, B., Hegab, H., 2009, "Experimental Analysis of Poiseuille Number in Square Microchannels," ASME International Mechanical Engineering Congress and Exposition, Lake Buena Vista, FL, USA, IMEC2009-11810.
- [14] Soman, J., Mathew, B., John, T. J., Hegab, H., 2009, "Flow Distribution in Multichanneled Microdevices with In-Line Manifolds," ASME International Mechanical Engineering Congress and Exposition, Lake Buena Vista, FL, USA, IMEC2009-11988.
- [15] Kunjumon, A., Mathew, B., John, T. J., Hegab, H., 2009, "Modeling a Non-Adiabatic Counter Flow Microchannel Heat Exchanger with Axial Heat Conduction," ASME International Mechanical Engineering Congress and Exposition, Lake Buena Vista, FL, USA, IMEC2009-11765.
- [16] John, T. J., Mathew, B., Hegab, H., 2009, "Thermal Performance of Microchannel Heat Exchangers Employing Nanofluids," Nanotech India, Cochin, Kerala, India
- [17] Bellamkonda, R., John, T. J., Mathew, B., Hegab, H., DeCoster, M., Davis, D., "Nanowire-GMR Integrated Microfluidic Biosensor," ASME Fluids Engineering Conference, Vail, CO, USA, FEDSM2009-78529.
- [18] John, T. J., Mathew, B., Hegab, H., 2009, "Analysis of the Diameter of Microbubbles Formed in a Cross flow Microchannel," ASME Fluids Engineering Conference, Vail, CO, USA, FEDSM2009-78495.
- [19] Mathew, B., John, T. J., Hegab, H., 2009, "Effect of Manifold Design on the Flow Distribution in Multichanneled Microfluidic Device," ASME Fluids Engineering Conference, CO, USA, FEDSM2009-78531.
- [20] John, T. J., Hegab, H., 2009, "Modeling Microfluidic Microbubble Generators," ASME Fluids Engineering Conference, Vail, CO, USA, FEDSM2009-78496.
- [21] John, T. J., Mathew, B., Hegab, H., 2009, "Analysis of Effectiveness of Parallel Flow Microchannel Heat Exchangers with Heat Transfer from Surroundings," ASME Heat Transfer Conference, San Francisco, CA, USA, HT2009-88230.
- [22] Mathew, B., John, T. J., Hegab, H., 2009, "Effectiveness of Counter Flow Microchannel Heat Exchangers Subjected to External Heat Transfer and Internal Heat Generation," ASME Heat Transfer Conference, San Francisco, CA, USA, HT2009-88167.

- [23] Bellamkonda, R., John, T. J., Mathew, B., DeCoster, M., Hegab, H., Palmer, J., Davis, D., 2009, "Microfabrication of Nanowires-Based GMR Biosensor," Proceedings of SPIE, Vol. 7318, 73181H-1.



## REFERENCES

- [1] Schubert, R.W., Conrad, S.A., Kim, S.S., 2003, "Using Microbubbles of Oxygenate Blood: Possible?," Proceedings of the 25th Annual International Conference of the IEEE EMBS Cancun, Mexico, pp. 431-434.
- [2] Prentice, P.A., McLean, D., Cuschieri, A., Dholakia, K, Campbell, P.A., 2005, "Spatially Controlled Sonoporation of Prostate Cancer Cells via Ultrasound Activated Microbubble Cavitations," Proceedings of the 3rd Annual International IEEE EMBS Special Topic Conference on Micro Technologies in Medicine and Biology, Kahuku, Oahu, Hawaii, pp.158-159.
- [3] Katherine, F., Rachel, P., Mark, B., 2007, "Ultrasound Microbubble Contrast Agents: Fundamentals and Application to Gene and Drug Delivery," *Annual Review of Biomedical Engineering*, 9, pp. 415-447.
- [4] Wackerbarth, H., Schön, P., Bindrich, U., 2009, "Preparation and Characterization of Multilayer Coated Microdroplets: Droplet Deformation Simultaneously Probed by Atomic Force Spectroscopy and Optical Detection," *Langmuir*, 25, pp. 2636-2640.
- [5] Leung Ki, Y. S., Kharouf, M., Van Lintel, H.T.G., Haller, M., Renaud Ph., 2000, "Bubble Engineering for Biomedical Valving Application," Annual International IEEE-EMBS Special Topic Conference on Microtechnologies in Medicine & Biology, Lyon, France, pp. 390-393.
- [6] Engla, W., Tachibana, M., Colina, A., Panizza, P., 2008 "A Droplet-Based High-Throughput Tubular Platform to Extract Rate Constants of Slow Chemical Reactions," *Chemical Engineering Science*, 63, pp. 1692-1695.
- [7] Okubo, Y., Maki, T., Nakanishi, F., Hayashi, T., Mae, K., 2010, "Precise Control of Polymer Particle Properties Using Droplets in the Microchannel," *Chemical Engineering Science*, 65, pp. 386-391.
- [8] Sarrazin, F., Prata, L., Di Micelia, N., Cristobal, G., Link, D.R., Weitz, D.A., 2007, "Mixing Characterization Inside Microdroplets Engineered on a Micro Coalesce," *Chemical Engineering Science*, 62, pp. 1042-1048.

- [9] Fang, M., Chandra, S., Park, C.B., 2008, "Building Three-Dimensional Objects by Deposition of Molten Metal Droplets," *Rapid Prototyping Journal*, 14(1), pp. 44–52.
- [10] Lee, T-M., Kang, T.G., Yang, J-S., Jo, J., Kim, K-Y., Choi, B-O, Kim D-S., 2008, "Drop-on-Demand Solder Droplet Jetting System for Fabricating Microstructure," *IEEE Transactions on Electronic Packaging Manufacturing*, 31(3), pp. 202-210.
- [11] Christopher, G. F., Anna, S. L., 2007, "Micro Fluidic Method for Generating Continuous Droplet Streams," *J. Phys. D: Appl. Phys.*, 40, pp. 319-336.
- [12] Haverkamp, V., Hessel, V., Löwe, H., Menges, G., Warnier, M. J.F., Rebrov, E. V., de Croon, Mart H.J.M., Schouten, J., Liauw, M. A., 2006, "Hydrodynamics and Mixer-Induced Bubble Formation in Microbubble Columns with Single and Multiple-Channels," *Chemical Engineering and Technology*, 29(9), pp. 1015-1026.
- [13] Cristini, V., Tan, Y-C., 2004, "Theory and Numerical Simulations of Droplet Dynamics in Complex Flows-a Review," *Miniaturization for Chemistry, Biology & Bioengineering*, 4, pp. 257-264.
- [14] Tan, S-H., Murshed, S.M.S., Nguyen, N.T., Wong, T. N., Yobas, L., 2008, "Thermally Controlled Droplet Formation in Flow Focusing Geometry: Formation Regimes and Effect of Nanoparticle Suspension," *J. Phys. D.: Appl. Phys.*, 41, pp. 165501-165506.
- [15] Xiao, P., Kit, C.W., Singh, P.H., Zhang, Y., Li, W.J., 2008, "The Carbon Nanotube Based Microbubble Generator in Micro Channel with Dynamic Fluid," NANO '08. 8th IEEE Conference on Nanotechnology, pp. 295-296.
- [16] Xu, J., Attinger, D., 2008, "Drop on Demand in a Microfluidic Chip," *Journal of Micromechanics and Microengineering*, 18, pp. 65020-65029.
- [17] Yang, C-G., Xu, Z-R., Wang, J-H., 2010, "Manipulation of Droplets in Microfluidic Systems," *Trends in Analytical Chemistry*, 29(2), pp. 141-157.
- [18] Umbanhowar, P.B., Prasad, V., Weitz, D.A., 2000, "Monodispersed Emulsion Generation via Drop Break Off in a Co flowing Stream," *Langmuir*, 16, pp. 347-351.
- [19] Byakoya, A. V., Gnyloskurenko, S. V., Nakamura, T., Raychenko, O. I., 2003, "Influence of Wetting Conditions on Bubble Formation at Orifice in an Inviscid Liquid Mechanism of Bubble Evolution," *Colloids and Surfaces A: Physicochem. Eng. Aspects*, 229, pp. 19-32.
- [20] Barrat J-L., Bocquet, L., 1999, "Large Slip Effect at a Non wetting Fluid-Solid Interface," *Physical Review Letters*, 82(23), pp. 4671-4674.

- [21] Rapoport, N.Y., Efors, A. L., Christensen, D.A., Kennedy, A.M., Nam, K.-H., 2009, "Microbubble Generation in Phase-Shift Nanoemulsions Used as Anticancer Drug Carriers," *Bubble Science, engineering and Technology*, 1(1/2), pp. 31-39.
- [22] Xu, J., Maxey, M.R., Karniadakis, G. E., 2002, "Numerical Simulation of Turbulent Drag Reduction Using Micro-Bubbles," *J. Fluid Mech.*, 468, pp.271-281.
- [23] Ramakrishnan, S., Kumar, R., Kuloor, N. R., 1969, "Studies in Bubble Formation Under Constant Flow Condition," *Chemical Engineering Science*, 24, pp. 731-747.
- [24] Tsuge H., Hibino, S., Nojima, U., 1981, "Volume of Bubble Formed at a Single Sub Merged Orifice in a Flowing Liquid," *American Institute of Chemical Engineers*, 24(4), pp. 630-636.
- [25] Marshall S.H., Chudacek M.W., Bagster D.F., 1993, "A Model for Bubble Formation from an Orifice with Liquid Cross Flow," *Chemical Engineering Science*, 48(11), pp. 2049-2059.
- [26] Bhunia, A., Pais, C.S., Kamotani, Y., Kim, I., 1998, "Bubble Formation in Coflow Configuration in Normal and Reduced Gravity," *AiChE Journal*, 44(7), pp. 1499-1509.
- [27] Nahra Henry, K., Kamotani, Y., 2000, "Bubble Formation form Wall Orifice in Liquid Cross Flow under Low Gravity," *Chemical Engineering Science*, 55, pp. 4653-4665.
- [28] Nahra Henry, K., Kamotani, Y., 2003, "Prediction of Bubble Diameter at Detachment from a Wall Orifice in Liquid Cross Flow under Reduced and Normal Gravity Conditions," *Chemical Engineering Science*, 58, pp. 55-69.
- [29] Sadatomi, M., Kawahara, A., Kano, K., Ohtomo, A., 2005, "Performance of a New Micro-Bubble Generator with a Spherical Body in a Flowing Water Tube," *Experimental Thermal and Fluid Science*, 29, pp. 615-623.
- [30] Van der Graaf, S., Nisisako, T., Schroen, C.G.P.H., van der Sman, R.G.M., Boom, R.M., 2005, "Lattice Boltzmann Simulations of Droplet Formation in a T-Shaped Microchannel," *Langmuir*, 22, pp. 4144-4152.
- [31] Husny, J., Cooper-White, J.J., 2006, "The Effect of Elasticity on Drop Creation in T-Shaped Microchannels," *J. Non-Newtonian Fluid Mech.*, 137, pp. 121-136.
- [32] Menech, M.DE, Garstecki, P., Jousse, F., Stone, H. A., 2007, "Transition from Squeezing to Dripping in a Microfluidic T-Shaped Junction," *J. Fluid Mech.*, 595, pp. 141-161.
- [33] Zhang, Y., Wang, L., 2009, "Experimental Investigation of the Bubble Formation in a Microfluidic T-Shaped Junction," *Nanoscale and Microscale Thermophysical Engineering*, 13, pp. 228-242.

- [34] Xiang, Y., LaVan, D. A., 2009, "Droplet Formation in Microfluidic T-junctions," *Materials Research Society Symposium Proceedings*, 1139, pp. 89-95.
- [35] Timgren, A., Tragarth, G., Tragarth, C., 2010, "A Model for Drop Size Prediction during Cross Flow Emulsification," *Chemical Engineering Research and Design*, 8, pp. 229-238.
- [36] Carmer, C., Fischer, P., Windhab, E.J., 2004, "Drop formation in a co-flowing ambient fluid," *Chemical Engineering Science*, 59, pp. 3045-3058.
- [37] Garstecki, P., Gitlin, I., DiLuzio, W., Whitesides, G.M., Kumacheva, E., Stone, H.A., 2004, "Formation of Monodispersed Bubbles in a Microfluidic Flow-Focusing Device," *Applied Physics Letters*, 85(13), pp. 2649-2651.
- [38] Xiong, R., Bai, M., Whan Na, Y., Chung, J. N., 2007, "Bubble Generation in a Microchannel with Barrier," 5<sup>th</sup> Joint ASME/JSME Fluids Engineering Conference, San Diego, California USA, pp. 437-443.
- [39] Xiong, R., Bai, M., Chung, J. N., 2007, "Formation of Bubble in a Simple Co-Flowing Micro-Channel," *Journal of Micromechanics and Microengineering*, 17, pp. 1002-1011.
- [40] Hashimoto, M., Shevkoplyas, S. S., Zasonska, B., Szymborski, T., Garstecki, P., Whitesides, G. M., 2008, "Formation of Bubbles and Droplets in Parallel, Coupled Flow-Focusing Geometries," *Small*, 4(10), pp. 1795-1805.
- [41] Saeki, D., Sugiura, S., Kanamori, T., Sato, S., Mukataka, S., Ichikawa, S., 2008, "Highly Productive Droplet Formation by Anisotropic Elongation of Thread Flow in a Microchannel," *Langmuir*, 24, pp. 13809-13813.
- [42] Dietrich, N., Poncin, S., Midoux, N., Huai Z. Li., 2008, "Bubble Formation Dynamics in Various Flow-Focusing Micro devices," *Langmuir*, 24, pp. 13904-13911.
- [43] Taotao, F., Youguang, M., Funfschilling, D., Huai, Z., 2009, "Bubble Formation and Breakup Mechanism in a Microfluidic Flow-Focusing Device," *Chemical Engineering Science*, 64, pp. 2392-2400.
- [44] John, T.J., Mathew, B., Hegab, H., 2009, "Analysis of the Diameter of Microbubbles formed in a Cross flow Microchannel," ASME Fluids Engineering Division Summer Meeting, Vail, Colorado, FEDSM2009-78495.
- [45] John, T.J., Hegab, H., 2009, "Modeling Microfluidic Microbubble Generators," ASME Fluids Engineering Division Summer Meeting, Vail, Colorado, FEDSM2009-78496.

- [46] John, T.J., Mathew, B., Hegab, H., 2009, "Experimental Analysis of Poiseuille Number in Square Microchannels," ASME International Mechanical Engineering Congress and Exposition, Lake Buena Vista, Florida, USA, IMEC2009-11810.
- [47] Sung Sam Kim, 2001, "Generation of Oxygen Microbubbles in a Micro Channel With Cross Current Liquid Flow," PhD dissertation, Louisiana Tech University, Ruston, Louisiana.
- [48] John, T.J., Hegab, H., 2010, "Experimental Study of Microbubble formation in Microchannels," 8th International Conference on Nanochannels, Microchannels, and Minichannels, Montreal, Canada, FEDSM2010-ICNMM-2010-31155.
- [49] Cubaud T., Ho Chin-M., 2004, "Transport of Bubbles in Square Microchannels," *American Institute of Physics*, 16(12), pp. 4575-4585.
- [50] Wang K., Lu Y. C., Xu J. H., Tan J., Luo G. S., 2010, "Generation of Micro Monodispersed Droplets and Bubbles in the Capillary Embedded T-Junction Microfluidic Devices," *American Institute of Chemical Engineers*, 57(2), pp. 209-306.
- [51] Taotao Fu , YouguangMa, DenisFunfschilling, ChunyingZhu, HuaiZ.Li, 2010, "Squeezing-to-Dripping Transition for Bubble Formation in a Microfluidic T-Junction," *Chemical Engineering Science*, 65 , pp. 3739–3748.
- [52] Davidson J. F., Schuler, B.O.G., 1960, "Bubble Formation at an Orifice in an Inviscid Liquid," *Transactions of Instrumentation of Chemical Engineers*, 38, pp. 335-342.
- [53] White, F.M., "Viscous Fluid Flow," 1991, Second Edition, McGraw-Hill, Columbus, Ohio.
- [54] Mathew, B., John. T. J., Hegab, H., 2010, "Dynamics of Fluid Flow in a Heated Zig-Zag Microchannel," 10th AIAA/ASME Joint Thermophysics and Heat Transfer Conference, Chicago, IL, USA, AIAA-5056.
- [55] Marc J. Madou, 2002, "Fundamentals of Micro Fabrication," Second Edition, CRC Press I Llc.
- [56] Droplet Breakup in a T-junction, 1994, Model Gallery, COMSOL®.
- [57] CoventorWare® user's manual, 2008.